Title

Precision Biomaterials for Modulating Regulatory T cells

Permalink

https://escholarship.org/uc/item/0s25c3jg

Author

Hadley, Pierce

Publication Date

2024

Peer reviewed|Thesis/dissertation

Precision Biomaterials for Modulating Regulatory T cells

by

Pierce Hadley

DISSERTATION
Submitted in partial satisfaction of the requirements for degree of
DOCTOR OF PHILOSOPHY
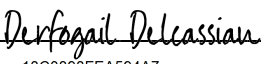
in

Bioengineering

in the

GRADUATE DIVISION

of the

UNIVERSITY OF CALIFORNIA, SAN FRANCISCO
AND
UNIVERSITY OF CALIFORNIA, BERKELEY

Approved:

DocuSigned by:

_Tejal Desai_____   Tejal Desai
0E5C999FDECA417...   Chair

DocuSigned by:

_Qizhi Tang_____   Qizhi Tang
DocuSigned by: ...04BA...

_Derfogail Delcassian_____   Derfogail Delcassian
18C0898FEA594A7...

_____

_____
                                                                        Committee Members

To my dad, Michael Hadley

Without his lead, I would never have walked this path,

And would not have learned to laugh along the way;

Your guidance is sorely missed.

ACKNOWLEDGEMENTS

I would first like to acknowledge my thesis advisors, Dr. Tejal Desai and Dr. Qizhi Tang, for having cultivated excellent labs filled with wonderful colleagues and collaborators. To Dr. Desai, thank you for allowing me a great deal of academic freedom to explore my interests, pairing me with Dr. Xiao Huang, and for sending me to Dr. Tang to further train in immunology. Your lab and support established the core from which the rest of my work grew and flourished. To Dr. Tang, thank you for giving me—a fool, ignorant in the ways of immunology—a chance in your lab. Your willingness to meet for hours on end, week after week, for the past few years was critical in making me the scientist I am today. Furthermore, your tolerance for my general shenanigans and banter helped make the lab a place I could call home.

To the members of the Desai lab who have contributed and supported my work—Dr. Xiao Huang, Lariana, Justin, Yuanzhou, and Eva—thank you. Dr. Huang was instrumental in my training, having found me lost during my rotation and taking me under his wing. Without your outreach, I would never have pursued immunology, and this entire work would never have been. My undergraduate mentee—and friend—Lariana, helped make tough lab days more bearable, provided important technical support, and was supportive of my terrible jokes; it was great to find another clown to join the circus.

To the members of the Tang lab—Emilie, Patrick, Wendy (and Wendy's mom), Roberto, Thibault, Vinh, Joey, Alex, Huiyun, and Peng—it has been a pleasure to work with you all. I consider myself lucky that I can call many of you as my friends. Emilie, thank you for taking the time to train me in immunological techniques and for being such a good sport when I went on hour-long (if not longer) story telling sessions during lunch and coffee breaks. I am thankful for your continued friendship outside of lab. To my younger brother from another mother— Thibault—I wish your time in lab could have been longer before you left for graduate school, but I will surely never forget the time we had in lab (how about that 2023 Diabetes Center Retreat!).

Roberto, I know that with you being present, I leave the lab in good hands; you have consistently given me scientific feedback, of which I am thankful, and have helped contribute to my departure as feeling bittersweet. Wendy, even though our lab building was wrapped up in light-blocking plastic, you still managed to bring the sunshine. You have cared for many of us in lab, both in our science (the mice thank you) and our emotional wellbeing, which goes above and beyond the typical lab manager. I hope you know how important you are to us all!

I am thankful for my friends, who have supported me through the exciting and too-often depressing times during PhD. Letitia and Kim: y'all funny. Thank you for making me get out of my normal geographical radius (i.e. the immediate vicinity of my Poang chair and fireplace) and for making life outside of lab so fun. To my MSTP cohort—especially Chris, Min Cheol, Albert, and Mitchel—this chapter is closing, but our story hasn't ended. It was fun going through COVID lockdown with you all; we may have been terrible at gaming but at least we tried.

I want to also thank my early mentors during my undergraduate years at UIUC, who helped build the foundation from which I've now been able to succeed. Dr. Rohit Bhargava and Dr. Marcia Pool—had you not recruited me to the Cancer Scholars program, I am doubtful I would have gotten here. Further, thank you Dr. Bhargava for letting me join your lab and allowing me to explore so many different research topics, many of which I wish to integrate with my newly attained immunology skillset. A very special thanks to my graduate mentor in Dr. Bhargava's lab—Dr. Mark Gryka—and his wife/my friend, Hailey Gryka. You welcomed me into your family while I was away from my own, and for that I am eternally grateful. Mark, you have been one of my best friends for so long now and I am thankful to have met you and to have been your undergraduate lab mentee. I know I am long overdue to help you both out with the house renovation and yard-work, so with the completion of this dissertation I better find the time.

Finally, I would like to thank my parents. You have always been supportive of my education and helped make this all possible. To my mom, thank you for accompanying me (on

the phone) during my walks to work. To my dad, I would not have made it here without you, literally. I did not intend to apply to be an engineer for undergrad, but your foresight led to me attending UIUC. This would lead me to finding lifelong friends and the needed skills/opportunities to get into UCSF, which I originally did not apply to until you added it to my list without telling me first. The chapters of my life have been prefaced by your influence. I wish you could be here to see what you helped build. Thank you.

SOURCE AND CONTRIBUTIONS

A.1. Chapter 2:

Chapter 2 represents an in-progress review paper not yet ready for publication. It primarily reviews the past 4 years of literature on the modulation of Tregs using biomaterials.

I identified and read relevant literature as well as wrote the initial manuscript draft. I worked with Dr. Qizhi Tang to receive feedback on the overall outline. Dr. Tang and Dr. Tejal Desai provided feedback.

A.2. Chapter 3:

Chapter 3 was originally published as: Precise surface functionalization of PLGA particles for human T cell modulation, Pierce Hadley, Yuanzhou Chen, Lariana Cline, Zhiyuan Han, Qizhi Tang, Xiao Huang, and Tejal Desai, *Nature Protocols*, **18**, 3289–3321 (2023) DOI: 10.1038/s41596-023-00887-8.

I worked closely with Dr. Xiao Huang—who originally published on the technology described in the protocol—to train in the relevant techniques, design new experiments/assays described in the manuscript, and draft the manuscript. Yuanzhou Chen, Lariana Cline, and Dr. Zhiyuan Han contributed to the data collection. All authors contributed to the editing.

A.3. Chapter 4:

This is an original, ongoing work which has not yet been completed for publication. For particle-related work, I closely with Dr. Xiao Huang and Lariana Cline. For T-cell related work, I worked with Dr. Emilie Ronin, Dr. Patrick Ho, and Alex Vu. I worked with the UCSF Genomics CoLab and sequenced by the UCSF Center for Advance Technology scRNA/TCRseq sample

"Life before death. Strength before weakness. Journey before destination."

-Brandon Sanderson, The Way of Kings

Precision Biomaterials for Modulating Regulatory T Cells

Pierce Hadley

ABSTRACT

Over the past few decades, regulatory T cell (Treg) therapy has gained traction for the treatment of autoimmunity, transplant rejection, and other inflammatory diseases. A necessary part of this process is cellular manufacturing, where Tregs are activated with immunomodulatory agents, expanded, and quality-assessed for CD4+ and Foxp3+ lineage purity before infusion. A challenge that has emerged in certain patient populations is the failure for Tregs to expand. This clinical manufacturing failure has been associated with the pre-expansion phenotype of the Tregs, with a higher proportion of terminally differentiated effector Tregs correlating with poorer expansion. While the heterogeneity of Treg phenotypes and their expansive capacities has been reported, it is unclear what signaling strengths are required to induce proliferation within each subset. To investigate this question, we used a biomaterial strategy for precisely attaching Treg stimulatory molecules onto polymeric particles via DNA hybridization to generate artificial antigen presenters. First, we optimized the fabrication technique, adapting numerous technologies commonly available to immunology labs, and exemplified its use in both human CD4+ and CD8+ T cell activation. Second, we then applied these materials towards activating human Tregs, identifying unique activation thresholds for inducing expansion and further subset-specific expansion behaviors. Third, unable to drive the expansion of effector Tregs using this approach, we turned to paired single cell RNA and TCR sequencing (scRNA/TCRseq) to identify distinguishing genes associated with high expansion. Using TCR tracking of highly expanding clones, we were able to subset pre-expanded cells by their post-expansion TCR clonotype enrichment, enabling the comparison between transcriptomes of high expanders and low expanders. This led to the finding that highly expanding clones were associated with numerous

markers associated with Treg stemness, proliferative capacity, and degradation of inhibitory

intracellular signals, whereas poorly expanding clones express numerous differentiation and

activation related genes. Further, we identified a group of proliferative Tregs which displayed an

inflammation-associated phenotype, which prompts further investigation into maintaining Treg

purity in strategies that improve expansion. This work sets a foundation in studying Treg subset

activation biology using precisely controlled signals and has uncovered numerous gene targets

for improving Treg expansion. We believe that investigating these targets and optimizing their

activation signals may provide a means of rescuing Treg proliferation in cases of manufacturing

failures, reenabling Treg therapy as a possible treatment option for affected patient populations.

TABLE OF CONTENTS

LIST OF FIGURES

LIST OF TABLES

Chapter 3.

Chapter 1

Preface

This dissertation work represents the investigation into the optimization and use of polymeric, DNA-scaffolded biomaterials in T cell and Treg subset activation as well as understanding the drivers of Treg proliferation via single cell genomic technologies, namely scRNAseq and scTCRseq. Chapter 2 first introduces the field of biomaterial immunomodulation of Tregs, which includes the generation of Tregs via biomaterial-modulated antigen presenting cells as well as direct Treg immunomodulation by biomaterials. We highlight the need for new material design and modulatory-cargo options, focusing on the need for more precise material loading strategies and the delivery of gene-targeting therapeutics. Additionally, we introduce and review the concept of artificial antigen presenting materials, which represent the main biomaterial technology used within this work.

To adapt DNA-scaffolded materials, a technology developed previously in our lab, we first needed to optimize the fabrication methodology and verify its applicability in T cell activation. Chapter 3 contains an optimized fabrication methodology as well as its exemplified use in human CD4+ and CD8+ T cell activation. We show that numerous material parameters, including the αCD3 to αCD28 ratio and particle number, must be optimized to maximize the expansion in each subset. We also document the new additions to the approach which integrate standard immunology tools, such as flow cytometry, into the biomaterial quality assessment workflow. This work was guided under the supervision of my postdoctoral mentor in the Desai lab, Dr. Xiao Huang.

Using the optimized fabrication approach, we demonstrate the utility of these particles in the activation of human Tregs and their subsets in isolation, as described in Chapter 4. We first showed that Tregs display αCD3 and αCD28 thresholds for allowing expansion. We then showed that Treg subsets display differential expansion capacities with unique post-expansion phenotypic maturation. We were unable to induce expansion in effector Tregs using αCD3/αCD28 optimization, thus we turned to scRNA/TCRseq to identify the transcriptomic

features of expanding cells. We describe an approach for attributing expansive capacity in un-expanded Tregs by evaluating the expansion of their matching clonotype in separate, activated samples. Using this proxy metric for expansion, we identified differentially expressed genes within high expanders and poor expanders. These targets provide the basis for future investigation into modulating expansion within Tregs, including effector subsets.

Chapter 2

Introduction: A Recent Update on Biomaterials to Enable

Regulatory T Cell Mediated Tolerance

A. ABSTRACT

In autoimmunity and transplant rejection, the balance between immunosuppressive regulatory T cells (Tregs) and proinflammatory cells—including CD4 or CD8+ T cells and stimulatory antigen presenting cells—is skewed towards tissue destructive processes. In these contexts, Tregs are unable to restore tolerance due to a variety of defects including insufficient expansion of antigen-specific cells, reduced survival, and limited suppressive capacity. There has been progress in the exogenous delivery of Treg enhancing compounds to support their induction, recruitment, activity, and survival, however, these strategies offer minimal control over localization and release-kinetics, which can result in off-target effects and suboptimal Treg response. Engineered biomaterials have been used to address similar challenges in other therapeutic applications, with a wide range of customization that enable the controlled presentation and release of immunomodulatory compounds to support the induction, recruitment, activity, and survival of Tregs. Here, we review the recent biomaterial approaches for supporting Treg-mediated tolerance in autoimmunity and transplantation, including materials that enable the indirect Treg modulation via generating tolerogenic antigen presenting cells (tolAPCs) or those that directly engage Tregs.

B. INTRODUCTION

Among various immune cells possessing tolerogenic properties, regulatory T cells (Tregs) are indispensable in maintaining tolerance to self and non-self-antigens. Inadequate suppression of auto-reactive T cells is the primary driver for autoimmune conditions and transplant rejection[1]. Although pharmacological interventions are the current clinical standard for immunosuppression, their long-term use is limited due to increased risks of infection, cancer, and organ toxicity. Consequently, enhancing Treg-mediated tolerance has garnered interest for its potential to provide localized and sustained tolerogenic responses in clinical applications[2].

Treg biology, including suppressive mechanisms, subtypes, and responsive cues, has been reviewed elsewhere[1,3–7]. Pertinent to this review, Tregs can be broadly into two main classes: thymically-generated, natural Tregs (nTregs) and peripherally-generated Tregs, which can be differentiated from Foxp3-negative T cells (pTregs-in vivo, iTregs-in vitro)[8]. nTregs, which stably express FoxP3 via epigenetic modifications, rely heavily on CD28 costimulation via CD80/CD86 and IL-2 for their development, expansion, survival, and lineage stability[9–12]. pTregs typically originate from Foxp3-negative T cells in tissues through interactions with tolerogenic APCs (tolAPCs) which provide high antigen-specific TCR-stimulation, low costimulation, and release tolerogenic paracrine factors such as TGF-β or IL-10[13]. Ex vivo, iTregs are similarly generated via delivery of TCR-stimulating cues, such as αCD3, and soluble TGF-β. These Tregs subtypes are capable of maintaining a suppressive niche through their recruitment to inflammatory sites and suppressive activity towards T cells and APCs, or by perpetuating further pTreg generation[8,13].

Persistent Treg activation—in the presence of inflammatory cues and absence of tolerogenic or survival signals—can lead to cell anergy, death, or even destabilization towards inflammatory phenotypes[14,15]. Thus, immune tolerance can be supported by strategies that deliver immunomodulatory signals for Treg recruitment, survival, and activation or for generating

tolAPCs to facilitate Treg induction. These signals are composed of highly diverse molecular classes—ranging from small molecules, proteins, and even other cells—which require tailored delivery methods for their optimal performance[16,17]. Biomaterial-based strategies provide numerous advantages compared to free supplementation or injection of immunomodulatory cues, including the co-delivery of multiple compounds, tunable surface-or-core loading, controlled release kinetics, and customizability for localized retention or systemic delivery[18–23]. While numerous reviews highlight unique biomaterial classes and engineering methods, this review focuses on recently published biomaterial strategies to achieve Treg-mediated tolerance in transplantation and autoimmunity, with a focus on indirect methods via tolAPCs generation to induce Treg formation or by directly interacting with T cells and Tregs. Due to the extensive range of tolerogenic mechanisms and biomaterials investigated beyond these recent works, readers are encouraged to refer to recent, more comprehensive reviews on tolerogenic and broad immune-targeting biomaterials[21,24–27].

C. INDIRECT T-CELL MODULATION VIA TOLEROGENIC APCs

C.1. General Considerations for Delivery and Targeting

Since the in vivo activation of both CD4+/Foxp3- conventional T cells (Tconvs) and Tregs canonically requires activation via APCs, the modulation of APCs into tolAPCs can target the T-cell inflammatory response upstream by anergizing Tconvs and enhancing pTreg induction or nTreg activity[28,29]. In vivo tolAPC targeting strategies face numerous engineering challenges involving trafficking to desired tissues, release and processing of immunomodulatory cargos, and avoiding unintended defects in nTreg function. The majority of recent approaches have included nanoscale (<1um) polymeric or liposomal particles, due to their ease for endocytosis and systemic tissue distribution [30–34]. Intravenous (I.V.) injection of particles >100nm diameter are typically processed in the liver or spleen while subcutaneous (S.C.) or intradermal injection may have increased propensity to lead to early lymph node trafficking, which has been proposed to lead to distinct immune activation and tolerance[21,30,35–39]. Depending on the application and desired administrative route, specific targeting to APCs can be enhanced by a variety surface-modifications, such as attaching mannan and apoB to enhance uptake by APCs via C-type lectin and stabilin scavenger receptors, respectively[21,40]. The material itself can also serve as an endocytosis-promoting signal, such as phosphatidylserine based liposomes[41]. In contrast, materials at the scale of microns or larger are locally retained until degradation and resist endocytosis if they are sufficiently large[42–46]. There have also been reports of direct intra-lymph-node injections of microparticles, which would not typically be able to drain into this site, allowing for larger lymph-node-contained drug depots[47]. These larger materials have been used to create local tolerogenic niches via delivery of suppressive signals, either via interactions with material-bound ligands, or release from within the material—including chemoattracts to further improve material-and-cell colocalization.

C.2. Immunomodulatory Agents for Generating tolAPCs

The diversity of tolAPC converting signals include small molecules, protein-based biologics, cell-derived vesicles, varied gene targeting technologies (CRISPR, miRNA), and even cells. Frequently used examples in the small molecule class includes calcitriol (vitamin D3), retinoic acid, dexamethasone, and rapamycin[30,31,33,48–50]. These drugs are normally formulated in endocytosable nanoparticles (polymeric or liposomal) co-delivered with antigen to release the majority of their payload within APCs. Combinations of particle sizes have also be used to maximally deliver tolAPC generating signals via small, endocytosable particles, and provide sustained release of tolerogenic niche signals via larger, non-endocytosable particles[42,44,51,52]. This strategy has been used in multiple disease contexts to deliver small, 1um diameter particles to direct the uptake of tolAPC-polarizing calcitriol and antigen as well as large, >30um diameter particles delivering TGF-β or APC-attracting GM-CSF (termed dual-sized microparticles). The evolution of this strategy in T1DM treatment has highlighted the importance of dose optimization and antigen-selection in improving the material effectiveness against increasingly more demanding immune challenges (e.g. diabetes prevention in prediabetic NOD mice versus rescue in recent disease onset in NOD mice)[42,53]. To improve the effectiveness of these dual-sized particles in established T1DM disease in NOD mice, T-cell depleting antibody αCD3—a strategy recently approved in human T1DM to bias towards depleting activated T-cells—was co-administered at the beginning of the particle regimen, which interestingly did not modify the disease status relative to particles alone[43]. While improvements are still needed for efficacy, we note an appreciated transparency during the material iteration process, which has clearly highlighted the importance of various design parameters and the underlying customizability of the biomaterial platform[52]. In the face of the large parameter space for material design, there is a need to improve the throughput of biomaterial engineering[54]. An interesting approach to generate tolAPCs involved screening combinations of inhibitory

immunomodulators alongside traditionally stimulatory Toll-Like Receptor (TLR) agonists (termed push/pull for simultaneous activation/inhibitory actions)[55]. After screening for synergistic inhibitor combinations for an optimal tolAPC phenotype, liposomes were formulated to include antigen (MOG or OVA), three inhibitors—dexamethasone, simvastatin, and small molecule SC-514 (NF-kB inhibitor)—and lipid-modified TLR-agonists flagellin (1st dose) or CpG (2nd dose). Compared to antigen+inhibitor-only liposomes, the inclusion of TLR agonists led to improved delay in EAE development, decreased formation of MOG-specific CD4+ effector memory T cells, and significantly increased numbers of MOG-specific CD4+ Foxp3+ Tregs.

Depending on the material and drug-payload, these materials can also be co-loaded in transplantation to generate a localized tolerogenic niche. A recent rat-to-mouse islet transplantation model used Matrigel to coencapsulate rat islets, microparticle encapsulated tacrolimus, and liposomal encapsulated clodronate which led to over 60% graft-survival after 500 days[56]. Compared to islet-only gel controls, the combination of immunosuppressants generated intra-graft, tolerogenic dendritic cells and significant enrichment for Foxp3+ Tregs which were shown to mediate graft-tolerance as rejection was accelerated by late-stage provision of anti-CD25 depleting antibody. The study identified that the combination of both tacrolimus and clodronate had synergistic graft-protective mechanisms compared to either drug alone. To note, while delivery of multiple agents can target multiple tolerogenic pathways, some studies have highlighted the important implications for coencapsulation, noting that phenotypically heterogenous APCs can form, especially if the drug-loading led to altered material properties such as size or charge which can lead to differential uptake efficiencies[31,48,55].

As opposed to the small molecule delivering materials, proteins have typically been delivered by large, non-endocytosable reservoirs, such as microparticles or hydrogels. While TGF-β or IL-10 can be used to direct Treg induction, these proteins have shown tolAPC

generating effects via reduction of dendritic cell costimulation and enhancing macrophage M2 differentiation, furthering the release IL-10 and TGF-B[43,53,57]. Biomaterials can also be tailored to improve the loading concentrations and release profiles of these biologics, as highlighted in the previous discussion on dual-sized microparticles[50,52]. One group developed large (>50um) poly-lactic-co-glycolic acid (PLGA) particles that display an ~70% burst-release over 24 hours with residual sustained release over 5 days; these particles were potent iTreg inducers in vitro, although in vivo their effect was less pronounced likely due to the still limited release duration[58]. A potential method for improving the efficacy of limited-release reagents is to promote the migration of APCs and other lymphocytes to the material during the earlier release phase. One strategy leveraged the biodegradability of PLGA/PLLA-HEMA microparticles with core-loaded autoantigens (GAD or MOG) and coated with mesoporous silica nanoparticles bearing 1) surface-bound Fas-L, capable of inducing apoptosis in Fas-expressing activated T cells and 2) core-loaded with the monocyte/T cell chemoattractant MCP-1[59]. These materials had potent disease-modifying effects in numerous models which were found to be mediated by antigen-specific Treg activity, including the reduction of EAE-severity in MOG immunized C57BL/6 mice and rescue of autoimmune diabetes in NOD mice—both treatments occurring after indication of disease onset. Mechanistically, the authors proposed macrophage uptake of material-induced T cell apoptotic bodies lead to a tolerogenic phenotype, and the concurrent presentation of autoantigen lead to increased proportions of antigen-specific Tregs[60]. While not explicitly shown whether these were nTreg or pTreg, the authors found that TGF-β blocking antibodies ablated the increase in antigen specific Tregs, suggesting a pTreg response. The autoantigens could be detected in the plasma after 15 days whereas MCP-1 is undetectable within a day due to its burst release from the MSNs. Thus, the continued therapeutic effect of antigen delivery may have been enabled by a stabilized tolerogenic niche. Further, at 72 hours these particles were enriched in the spleen and liver—a common site for I.V. administered microparticles—and were selectively uptaken by Marco+ macrophages, where the uptake via this receptor has been

previously shown to induce an M2 phenotype, which may have further promoted a tolerance[61]. Similarly, another study leveraging MOG-loaded MSNs for treating EAE found selective particle uptake in the spleen across numerous cell types including CD11c+ DCs, macrophages, and B220+ B cells, and noted a primary CD86+ costimulation defect in antigen-loaded MSNs, leading to an upregulation in both the percentage and number of CD4+ Foxp3+ Tregs in the spleen[62]. The therapeutic effect was observed when treating during disease induction as well as during the onset of disease—similar late-stage timing to the FasL/MCP-1/autoantigen study— which was further enhanced via the addition of ROS-scavenging, cerium-based nanoparticles onto the MSNs, acting to further tolerize splenic APCs.

At a larger scale, some materials have even attempted to deliver cell-derived materials and even encapsulating whole cells. Cell-derived vesicles, including exosomes or cell membrane covered particles, present and release numerous immunomodulatory proteins which can be used to produce tolAPCs, block DC costimulation, and even directly modulate with T cells. PLGA nanoparticles coated in Treg-derived cell membranes have been shown to reduce DC maturation and inhibit T cell proliferation[63]. Further, exosomes have been further engineered to present CTLA-4 and PD-L1, reducing the activation of T cells by blocking DC costimulation and direct T cell suppression[64]. In either case, nano-scale exosomes are short-lived in vivo, thus scaffolds and hydrogels have been developed to prolong their release in vivo[46,65,66].

Finally, with the rise of genetic engineering tools—including CRISPR, RNAi, etc.— tolAPC generation can be accomplished via targeted downregulation of costimulatory molecules or upregulation of inhibitory receptors[29,67,68]. Biomaterials can aid the delivery of these tools by protecting the materials from degradation, increased delivery efficiency, and reducing immunogenicity. Hydrophilic, negatively charged molecules such as RNA can have improved loading by incorporation of cationic polymers and lipids, which can additionally aid in APC uptake and endosome escape [69–71]. One approach to used PLGA nanoparticles embedded with

cationic cholesterol lipid to co-deliver plasmid encoding CRISPR-Cas9, gRNAs targeting CD80/86/40, and BDC2.5mi peptide[70]. Intravenous injection of this material into prediabetic, NOD mice downregulated the target costimulatory molecules expressed on DCs in lymph nodes, spleen, and blood, induced antigen-specific Tregs, and delayed onset of diabetes. On challenge in RNA delivery is the potential to form an inflammatory response via TLR signaling, leading to the generation of inflammatory T cells. Thus, one approach for the liposomal delivery of mRNA encoding EAE-specific autoantigen, mRNA were modified with uridine analogs and delivered in as ssRNA, which prevent mRNA induced upregulated of costimulatory molecules, induced high levels of antigen-specific Tregs, and reduced EAE progression[72]. It is likely that this approach is more feasible prior to disease onset when DCs have not already upregulated costimulatory molecules. Advancing the delivery of gene modifying tools may provide unique new opportunities for targeting specific pathways which may be difficult using the existing pool of small-molecules and proteins.

While immunomodulatory drugs can modulate tolerogenic pathways APCs it is worth mentioning cases where autoantigen-only delivery can induce tolAPCs. One proposed mechanism is particle uptake by the MARCO scavenger receptor—which has preference for negatively charged, protein coated materials—on phagocytic cells in the spleen or liver, such as macrophages, leading to the release of TGF-B and IL-10 release[25,36,73] although there are conflicting reports when antigen-only delivery is tolerogenic which should be elucidated based on inflammatory status prior to antigen-delivery[33,74]. Other scavenger receptors involved on naturally tolerogenic cells, such as LSECs, may be preferentially[40]. Further, in vitro uptake studies of antigen-only particles show variable effects on increasing MHC-II and costimulatory molecules, which may be due to varying particle sizes and ability for antigen processing/maturation[75,76] It is likely that the choice of delivery site, material size, and timing relative to disease onset are important factors to consider. There are also conflicting results as

to the required number of unique antigen species to achieve tolerance. Single-antigen delivery has been shown to induce antigen-specific Treg responses[77] with some instances observing bystander tolerance against other antigens[61,72]. Further, the protective-synergy of delivering multiple peptides has been reported[78,79]. One study in NOD mice found that PLGA-NP delivery of individual proteins (chgA, GAD65, insulin) implicated in generating CD4+ T cell responses found no delay in diabetes onset while co-delivery of all three proteins delayed onset[61]. In contrast, another study in NOD mice identified that individual liposomal delivery of IGRP$_{206\text{-}214}$ (CD8+ specific) peptide could delay diabetes onset. However, when co-delivered with BDC2.5mi (CD4+ specific)—which was shown to individually delay onset—disease protection is lost. Interpreting these results are confounded by differences in T-cell subset (CD4 vs CD8) specificity, administration routes, timing relative to disease onset, inclusion of immunomodulatory factors. Thus, increased attention on delivered antigen formulations are needed for improving therapeutic efficacy.

D. DIRECT T-CELL MODULATION

D.1. Artificial Antigen Presenting Cells

Biomaterials with surface-bound ligands for engaging the TCR and costimulatory receptors, such as agonist αCD3/CD28 antibodies, MHC-peptide complexes, and release of encapsulated factors—such as IL-2—can act as artificial antigen presenting cells (aAPCs) to promote T cell activation[80–83]. Nanoparticles bearing peptide-loaded MHCs have previously been shown to generate antigen-specific cell responses but has typically led to the expansion of FoxP3-negative T cells with potent regulatory properties, notably distinct from traditional pTregs[84,85]. Protocols for Foxp3 induction in T cells, however, typically employ TCR-stimulation without costimulation and deliver of TGF-β—mimicking the Treg induction signals provided by tolAPCs[86–88]. PLGA nanoparticles have induced Foxp3 expression within both CD4 and CD8 T cells via paracrine delivery of co-loaded TGF-β and IL-2, with cell-binding promoted by particle-bound αCD4/CD8[81]. This inductive effect was maintained when replacing the CD4/CD8 antibodies with agonistic αCD3/αCD28—however, the addition of costimulation should be viewed cautiously, as this may lead to T cell activation even outside of inflammatory disease contexts if TGF-β has insufficient dosing or release duration. Thus, in a xenogeneic GVHD model in NSG mice, the authors formulated particles to only deliver aCD3, IL2, and TGF-β, which were capable of sustaining significantly higher CD4+ and CD8+ human Treg proportions, leading to improved host survival. Removal of αCD28 was justified by minimal-costimulation provided in-trans by surrounding cells, thus allowing materials to act as tolerogenic aAPCs and not be overstimulating or inflammatory. In contrast, natural tolAPCs were still capable of pTreg formation despite CD80/CD86 expression, thus indicating that the relative signaling strengths of TCR, costimulation, and inductive cues presented by biomaterials requires careful tuning to optimally induce Tregs. This signal tuning is an ongoing challenge for surface-conjugated biomaterials, with difficulties in achieving high surface density, relative tunability, and variable

loading efficiencies[18,50,80]. One approach using a cationic polymer poly(beta-amino ester) (PBAE) blended with PLGA saw significantly higher surface loading capacity and stability of αCD3/αCD28 using covalent attachment approaches[80]. However, it was demonstrated that in vitro, increasing the density of αCD3/αCD28 can eventually lead to immunostimulatory aAPCs with a reduction in iTregs, indicating the importance for surface tunability for optimal induction. In vivo, composite PLGA/PBAE aAPCs loaded with TGF-β led to increased pTreg formation compared to PLGA-only aAPCs—this was attributed to higher cell-binding efficiency and increased densities of agonistic surface proteins. While the PBAE/PLGA material had significant reduction in TGF-β release compared to PLGA-particles, the PBAE/PLGA still generated more pTregs. This material had also been used in vivo to induce Tregs in a streptozotocin model of T1DM in C57BL/6 mice, although the Treg inductive effect was short-lived and still showed some stimulatory effect towards other T cells, indicating further material and dosing optimization is needed[82].

D.2. Supporting Treg Recruitment and Survival

Optimal therapeutic outcomes rely on effective Treg recruitment, maintaining stability under inflammatory conditions, and ensuring their prolonged survival. Treg recruitment has been attempted using CCL22, IL33, and CCL1 released from microparticles or hydrogels[68,89–91]. One study demonstrated that sustained particle release of CCL22 protected against murine hindlimb allograft rejection and increased donor-specific Treg enrichment[68]. However, there was increased rejection incidence in the highest CCL22 doses, which was proposed to be due to receptor internalization and subsequent reduced chemotactic function to inflammatory sites. Treg recruitment signals may also have differential effects on nTreg or induced Treg; one study co-encapsulating Tregs and murine islets within CCL-1 containing, alignate-GelMa microgels identified that while iTreg and nTreg express similar levels of CCR8—the receptor for CCL-1—

both cell types were retained within the microgels, although CCL-1 enhanced the suppressive activity of nTregs while blunting the activity of iTregs. The authors also investigated IL-2 inclusion within these gels to enhance their survival; as predicted, IL-2 codelivery with CCL-1 showed optimal Treg viability and phenotypic stability, although lack of IL2 more severely impaired iTregs compared to nTregs. While biomaterial delivery of IL-2 can aid in Treg survivability, this runs the risk of expanding non-Treg populations and must be carefully tuned if it is not co-released with tolerogenic cues[92–94].

While low-dose IL-2 strategies have been used to preferentially activate Tregs, other IL-2 delivery via biomaterials have demonstrated Treg biasing by using 1) administration of IL-2 muteins[93,95], 2) surface-presentation of IL-2 via Treg-biasing IL-2 binding antibodies[20], and 3) surface-tethering Tregs with IL-2 releasing materials[96,97]. Polymeric nanowires with surface conjugated anti-mouse-IL2 antibody (JES6-1) could locally sequester and present IL-2 with biased activity towards Tregs[20,98]. Anti-human-IL2 antibodies, including those pre-complexed with IL2, have been developed and could be applied towards IL-2 depots or aAPC applications[83,99,100]. Surface-tethering of IL-2 depots directly onto Tregs (termed "backpacking") may further reduce off-target effects, as one method used disulfide-crosslinked IL-2-Fc nanogels which would release IL-2 upon TCR-dependent Treg release of disulfide-reducing glutathione, leading to enhanced in vivo survivability and therapeutic action. However, these materials could still release IL-2 non-specifically into the environment, thus highlighting the potential need for using IL-2 muteins to further enhance Treg specificity.

D.3. Considerations for Delivery of T-cell Inhibitory Biologics

Activation of T-cell inhibitory pathways to induce anergy, tolerogenic apoptosis, or reduce activation of inflammatory pathways can contribute to Treg induction. Hydrogels displaying either FasL or PD-L1 have been used in islet transplantation, leading to increase iTregs within the grafts which prolong graft survival[93,101,102]. FasL-mediated induction is primarily driven by tolAPC generation after uptake of apoptotic bodies, as discussed previously, and PD-L1 is capable of directly inducing iTregs—particularly in the presence of additional inductive cues like TGF-β[103,104]. Additionally, while in certain contexts nTregs may appear resistant to the inhibitory action of other biologics, such as FasL and PD-L1, most biomaterials studies do not distinguish the effects between nTreg and iTreg, which should be further investigated due to their differential lineage stability and functional capacitiy[105,106]. Another inhibitory molecule, CTLA-4-Ig, has been delivered to selectively block CD80/CD86 costimulation from APCs, leading to Treg inducing, TCR-only anergic signaling. However, this approach must be carefully dosed to prevent adverse effects on nTregs due to their dependence on CD80/CD86 for expansion and survival[64,107–109]. Given that T cell inhibiting strategies may also inhibit nTreg, one study used PLGA nanoparticles to intracellularly deliver miRNA-125a, which has been shown to inhibit inflammatory T cell pathways while enhancing Treg activity[69]. Particles were not only preferentially uptaken by activated effector T cells, but they also led to the decreased expression of STAT3 and IFNγ, enhanced iTreg suppressive activity under inflammatory IL-6 conditions, and dramatically increased Treg proportions in vivo[69]. These genetic engineering tools offer a promising alternative to the broad inhibitory actions of protein biologics, enabling the development of tolerogenic therapies tailored to specific inflammatory pathways that do not impair Treg activity.

E. CONCLUSIONS AND FUTURE PERSPECTIVE

Recent biomaterials promote Treg-mediated tolerance via generating tolAPCs or directly delivering T-cell and Treg modulating factors. However, many of these methods do not result in sustained tolerance. While Treg induction is promising due to a large recruitment pool and the obligatory conversion of inflammatory T-cells, their phenotypic stability, persistence, and memory formation capacity require further study, especially relative to nTreg-centered approaches[110]. Also, some pTreg generation techniques may negatively impact nTreg function—for example, pTreg inducing materials typically present T cell anergic signals, such as lack of costimulation, which is detrimental to nTreg function. Present studies rarely decouple the respective activation responses and therapeutic contributions between pTreg and nTreg. To provide clarity, materials claiming Treg-enhancing functions should provide additional metrics like expansion (in vitro) or absolute number (in vivo), as percent enrichment may not accurately reflect an enhancement of Treg numbers or function and instead could be reporting a direct inhibition and reduction of effector T cells. Assessing the generation and persistence of antigen-specific Tregs may also be essential since antigen-specific Treg responses could contribute to potent, lasting tolerance.

Current approaches significantly overlap in their biomaterial and loading methods, yet there is a need to identify new materials and surface-attachment strategies to improve both surface/core-loading and release-profiles[18,80]. Despite these material advancements, the standard combination of antigen and immunosuppressant delivery might be insufficient for maintaining tolerance. Strategies such as aAPCs have not received much recent attention outside of ex vivo manufacturing, likely due to non-Treg off-target effects. However, incorporating IL-2 muteins, Treg-biasing αIL2 antibodies, or inhibitory biomolecules like PD-L1 may increase Treg specificity. Furthermore, there is potential for exploring aAPC formulations and their capacity to boost Treg expansion and function, as aAPCs have been specifically

designed in the T-cell and CAR-T cell manufacturing field to improve phenotypic enrichment and

expansion both in vitro and in vivo. Finally, emerging genetic engineering tools could enable

more precise targeting of inflammatory pathways or Treg enhancement and is worth further

investigation. Addressing the limitations of these biomaterial formulations can improve our

understanding of Treg tolerance and help generate more effective and persistence therapies for

autoimmune diseases and transplantation.

F. REFERENCES

1. Romano, M., Fanelli, G., Albany, C. J., Giganti, G. & Lombardi, G. Past, Present, and Future of Regulatory T Cell Therapy in Transplantation and Autoimmunity. *Frontiers in Immunology* **10**, (2019).

2. Bluestone, J. A., McKenzie, B. S., Beilke, J. & Ramsdell, F. Opportunities for Treg cell therapy for the treatment of human disease. *Front Immunol* **14**, 1166135 (2023).

3. Sakaguchi, S., Yamaguchi, T., Nomura, T. & Ono, M. Regulatory T Cells and Immune Tolerance. *Cell* **133**, 775–787 (2008).

4. Ferreira, L. M. R., Muller, Y. D., Bluestone, J. A. & Tang, Q. Next-generation regulatory T cell therapy. *Nat Rev Drug Discov* **18**, 749–769 (2019).

5. Shevyrev, D. & Tereshchenko, V. Treg Heterogeneity, Function, and Homeostasis. *Frontiers in Immunology* **10**, 3100 (2020).

6. Khantakova, J. N., Bulygin, A. S. & Sennikov, S. V. The Regulatory-T-Cell Memory Phenotype: What We Know. *Cells* **11**, (2022).

7. Sumida, T. S., Cheru, N. T. & Hafler, D. A. The regulation and differentiation of regulatory T cells and their dysfunction in autoimmune diseases. *Nat Rev Immunol* 1–15 (2024) doi:10.1038/s41577-024-00994-x.

8. Shevach, E. M. & Thornton, A. M. tTregs, pTregs, and iTregs: Similarities and Differences. *Immunol Rev* **259**, 88–102 (2014).

9. Tang, Q. *et al.* Cutting edge: CD28 controls peripheral homeostasis of CD4+CD25+ regulatory T cells. *J Immunol* **171**, 3348–3352 (2003).

10. Esensten, J. H., Helou, Y. A., Chopra, G., Weiss, A. & Bluestone, J. A. CD28 Costimulation: From Mechanism to Therapy. *Immunity* **44**, 973–988 (2016).

11. Golovina, T. N. *et al.* CD28 Costimulation is Essential for Human T Regulatory Expansion and Function. *J Immunol* **181**, 2855–2868 (2008).

12.   Hombach, A. A., Kofler, D., Hombach, A., Rappl, G. & Abken, H. Effective Proliferation of Human Regulatory T Cells Requires a Strong Costimulatory CD28 Signal That Cannot Be Substituted by IL-2. *J Immunol* **179**, 7924–7931 (2007).

13.   Wardell, C. M., MacDonald, K. N., Levings, M. K. & Cook, L. Cross talk between human regulatory T cells and antigen-presenting cells: Lessons for clinical applications. *European Journal of Immunology* **51**, 27–38 (2021).

14.   Bailey-Bucktrout, S. L. *et al.* Self-antigen driven activation induces instability of regulatory T cells during an inflammatory autoimmune response. *Immunity* **39**, 949–962 (2013).

15.   Zhou, X. *et al.* Instability of the transcription factor Foxp3 leads to the generation of pathogenic memory T cells in vivo. *Nat Immunol* **10**, 1000–1007 (2009).

16.   Zhong, J. X., Raghavan, P. & Desai, T. A. Harnessing Biomaterials for Immunomodulatory-Driven Tissue Engineering. *Regen. Eng. Transl. Med.* (2022) doi:10.1007/s40883-022-00279-6.

17.   Trucillo, P. Biomaterials for Drug Delivery and Human Applications. *Materials (Basel)* **17**, 456 (2024).

18.   Huang, X. *et al.* DNA scaffolds enable efficient and tunable functionalization of biomaterials for immune cell modulation. *Nat. Nanotechnol.* **16**, 214–223 (2021).

19.   Hadley, P. *et al.* Precise surface functionalization of PLGA particles for human T cell modulation. *Nat Protoc* **18**, 3289–3321 (2023).

20.   Zamecnik, C. R. *et al.* An Injectable Cytokine Trap for Local Treatment of Autoimmune Disease. *Biomaterials* **230**, 119626 (2020).

21.   Yousefpour, P., Ni, K. & Irvine, D. J. Targeted modulation of immune cells and tissues using engineered biomaterials. *Nat Rev Bioeng* **1**, 107–124 (2023).

22.   Cheung, A. S., Zhang, D. K. Y., Koshy, S. T. & Mooney, D. J. Scaffolds that mimic antigen-presenting cells enable ex vivo expansion of primary T cells. *Nat Biotechnol* **36**, 160–169 (2018).

23.   Dellacherie, M. O., Seo, B. R. & Mooney, D. J. Macroscale biomaterials strategies for local immunomodulation. *Nat Rev Mater* **4**, 379–397 (2019).

24.   E. Emerson, A., M. Slaby, E., C. Hiremath, S. & D. Weaver, J. Biomaterial-based approaches to engineering immune tolerance. *Biomaterials Science* **8**, 7014–7032 (2020).

25.   Gammon, J. M. & Jewell, C. M. Engineering immune tolerance with biomaterials. *Adv Healthc Mater* **8**, e1801419 (2019).

26.   Benne, N., ter Braake, D., Stoppelenburg, A. J. & Broere, F. Nanoparticles for Inducing Antigen-Specific T Cell Tolerance in Autoimmune Diseases. *Front Immunol* **13**, 864403 (2022).

27.   Wang, H. & Mooney, D. J. Biomaterial-assisted targeted modulation of immune cells in cancer treatment. *Nature Mater* **17**, 761–772 (2018).

28.   Raker, V. K., Domogalla, M. P. & Steinbrink, K. Tolerogenic Dendritic Cells for Regulatory T Cell Induction in Man. *Frontiers in Immunology* **6**, (2015).

29.   Morelli, A. E. & Thomson, A. W. Tolerogenic dendritic cells and the quest for transplant tolerance. *Nat Rev Immunol* **7**, 610–621 (2007).

30.   Buckle, I. *et al.* Tolerance induction by liposomes targeting a single CD8 epitope IGRP206-214 in a model of type 1 diabetes is impeded by co-targeting a CD4+ islet epitope. *Immunol Cell Biol* **100**, 33–48 (2022).

31.   ter Braake, D., Benne, N., Lau, C. Y. J., Mastrobattista, E. & Broere, F. Retinoic Acid-Containing Liposomes for the Induction of Antigen-Specific Regulatory T Cells as a Treatment for Autoimmune Diseases. *Pharmaceutics* **13**, 1949 (2021).

32.   Kwon, S. P. *et al.* Nanoparticle-Mediated Blocking of Excessive Inflammation for Prevention of Heart Failure Following Myocardial Infarction. *Small* **17**, 2101207 (2021).

33.   Bergot, A.-S. *et al.* Regulatory T Cells Induced by Single-Peptide Liposome Immunotherapy Suppress Islet-Specific T Cell Responses to Multiple Antigens and Protect from Autoimmune Diabetes. *The Journal of Immunology* **204**, 1787–1797 (2020).

34.   Kenison, J. E. *et al.* Tolerogenic nanoparticles suppress central nervous system inflammation. *Proc Natl Acad Sci U S A* **117**, 32017–32028 (2020).

35.   Burke, J. A. *et al.* Subcutaneous nanotherapy repurposes the immunosuppressive mechanism of rapamycin to enhance allogeneic islet graft viability. *Nat. Nanotechnol.* **17**, 319–330 (2022).

36.   Kelly, C. P. *et al.* TAK-101 Nanoparticles Induce Gluten-Specific Tolerance in Celiac Disease: A Randomized, Double-Blind, Placebo-Controlled Study. *Gastroenterology* **161**, 66-80.e8 (2021).

37.   Gholamzad, M., Baharlooi, H., Shafiee Ardestani, M., Seyedkhan, Z. & Azimi, M. Prophylactic and Therapeutic Effects of MOG-Conjugated PLGA Nanoparticles in C57Bl/6 Mouse Model of Multiple Sclerosis. *Adv Pharm Bull* **11**, 505–513 (2021).

38.   Brzezicka, K. A. *et al.* Suppression of Autoimmune Rheumatoid Arthritis with Hybrid Nanoparticles That Induce B and T Cell Tolerance to Self-Antigen. *ACS Nano* **16**, 20206–20221 (2022).

39.   Sohn, H. S. *et al.* Tolerogenic nanoparticles induce type II collagen–specific regulatory T cells and ameliorate osteoarthritis. *Science Advances* **8**, eabo5284 (2022).

40.   Liu, Q. *et al.* Use of Polymeric Nanoparticle Platform Targeting the Liver To Induce Treg-Mediated Antigen-Specific Immune Tolerance in a Pulmonary Allergen Sensitization Model. *ACS Nano* **13**, 4778–4794 (2019).

41.   Tredicine, M. *et al.* Liposome-based nanoparticles impact on regulatory and effector phenotypes of macrophages and T cells in multiple Sclerosis patients. *Biomaterials* **292**, 121930 (2023).

42.   Lewis, J. S. *et al.* Dual-Sized Microparticle System for Generating Suppressive Dendritic Cells Prevents and Reverses Type 1 Diabetes in the Nonobese Diabetic Mouse Model. *ACS Biomater. Sci. Eng.* **5**, 2631–2646 (2019).

43.   Stewart, J. M., Posgai, A. L., Leon, J. J., Haller, M. J. & Keselowsky, B. G. Combination Treatment with Antigen-Specific Dual-Sized Microparticle System Plus Anti-CD3 Immunotherapy Fails to Synergize to Improve Late-Stage Type 1 Diabetes Prevention in Nonobese Diabetic Mice. *ACS Biomater. Sci. Eng.* **6**, 5941–5958 (2020).

44.   Kwiatkowski, A. J. *et al.* Treatment with an antigen-specific dual microparticle system reverses advanced multiple sclerosis in mice. *Proc Natl Acad Sci U S A* **119**, e2205417119 (2022).

45.   Nguyen, T. T. *et al.* Engineering of hybrid spheroids of mesenchymal stem cells and drug depots for immunomodulating effect in islet xenotransplantation. *Sci Adv* **8**, eabn8614 (2022).

46.   Mohammadi, M. R. *et al.* Exosome loaded immunomodulatory biomaterials alleviate local immune response in immunocompetent diabetic mice post islet xenotransplantation. *Commun Biol* **4**, 1–17 (2021).

47.   Gammon, J. M. *et al.* Engineering the lymph node environment promotes antigen-specific efficacy in type 1 diabetes and islet transplantation. *Nat Commun* **14**, 681 (2023).

48.   Carey, S. T., Gammon, J. M. & Jewell, C. M. Biomaterial-enabled induction of pancreatic-specific regulatory T cells through distinct signal transduction pathways. *Drug Deliv. and Transl. Res.* **11**, 2468–2481 (2021).

49.   Kuppan, P. *et al.* Co-localized immune protection using dexamethasone-eluting micelles in a murine islet allograft model. *American Journal of Transplantation* **20**, 714–725 (2020).

50.   Bridgeman, C. J., Shah, S. A., Oakes, R. S. & Jewell, C. M. Dissecting regulatory T cell expansion using polymer microparticles presenting defined ratios of self-antigen and regulatory cues. *Frontiers in Bioengineering and Biotechnology* **11**, (2023).

51.   Brusko, M. A. *et al.* Immunomodulatory Dual-Sized Microparticle System Conditions Human Antigen Presenting Cells Into a Tolerogenic Phenotype In Vitro and Inhibits Type 1 Diabetes-Specific Autoreactive T Cell Responses. *Front Immunol* **11**, 574447 (2020).

52.   Kwiatkowski, A. J. *et al.* Design principles of microparticle size and immunomodulatory factor formulation dictate antigen-specific amelioration of multiple sclerosis in a mouse model. *Biomaterials* **294**, 122001 (2023).

53.   Lewis, J. S. *et al.* A combination dual-sized microparticle system modulates dendritic cells and prevents type 1 diabetes in prediabetic NOD mice. *Clinical Immunology* **160**, 90–102 (2015).

54.   McDonald, S. M. *et al.* Applied machine learning as a driver for polymeric biomaterials design. *Nat Commun* **14**, 4838 (2023).

55.   Deak, P., Knight, H. R. & Esser-Kahn, A. Robust tolerogenic dendritic cells via push/pull pairing of toll-like-receptor agonists and immunomodulators reduces EAE. *Biomaterials* **286**, 121571 (2022).

56.   Pathak, S. *et al.* Particulate-Based Single-Dose Local Immunosuppressive Regimen for Inducing Tolerogenic Dendritic Cells in Xenogeneic Islet Transplantation. *Advanced Healthcare Materials* **10**, 2001157 (2021).

57.   Beskid, N. M. *et al.* IL-10-Functionalized Hydrogels Support Immunosuppressive Dendritic Cell Phenotype and Function. *ACS Biomater. Sci. Eng.* **8**, 4341–4353 (2022).

58.   Li, Y. *et al.* Immunosuppressive PLGA TGF-β1 Microparticles Induce Polyclonal and Antigen-Specific Regulatory T Cells for Local Immunomodulation of Allogeneic Islet Transplants. *Frontiers in Immunology* **12**, (2021).

59.   Chen, X. *et al.* Modular immune-homeostatic microparticles promote immune tolerance in mouse autoimmune models. *Science Translational Medicine* **13**, eaaw9668 (2021).

60.   Gordon, S. & Plüddemann, A. Macrophage Clearance of Apoptotic Cells: A Critical Assessment. *Front Immunol* **9**, 127 (2018).

61.   Podojil, J. R. *et al.* Tolerogenic Immune-Modifying Nanoparticles Encapsulating Multiple Recombinant Pancreatic β Cell Proteins Prevent Onset and Progression of Type 1 Diabetes in Nonobese Diabetic Mice. *The Journal of Immunology* **209**, 465–475 (2022).

62. Nguyen, T. L. *et al.* Immunosuppressive biomaterial-based therapeutic vaccine to treat multiple sclerosis via re-establishing immune tolerance. *Nat Commun* **13**, 7449 (2022).

63. Li, S. *et al.* Biomimetic immunomodulation by crosstalk with nanoparticulate regulatory T cells. *Matter* **4**, 3621–3645 (2021).

64. Xu, Z. *et al.* Engineering Programmed Death Ligand-1/Cytotoxic T-Lymphocyte-Associated Antigen-4 Dual-Targeting Nanovesicles for Immunosuppressive Therapy in Transplantation. *ACS Nano* **14**, 7959–7969 (2020).

65. Su, N. *et al.* Mesenchymal stromal exosome–functionalized scaffolds induce innate and adaptive immunomodulatory responses toward tissue repair. *Science Advances* **7**, eabf7207 (2021).

66. Zhang, Y. *et al.* Hydrogel-load exosomes derived from dendritic cells improve cardiac function via Treg cells and the polarization of macrophages following myocardial infarction. *Journal of Nanobiotechnology* **19**, 271 (2021).

67. Passeri, L. *et al.* Tolerogenic IL-10-engineered dendritic cell-based therapy to restore antigen-specific tolerance in T cell mediated diseases. *Journal of Autoimmunity* **138**, 103051 (2023).

68. Fisher, J. D. *et al.* In situ recruitment of regulatory T cells promotes donor-specific tolerance in vascularized composite allotransplantation. *Science Advances* **6**, eaax8429 (2020).

69. Zhang, J. *et al.* MicroRNA-125a-Loaded Polymeric Nanoparticles Alleviate Systemic Lupus Erythematosus by Restoring Effector/Regulatory T Cells Balance. *ACS Nano* **14**, 4414–4429 (2020).

70. Luo, Y.-L. *et al.* An All-in-One Nanomedicine Consisting of CRISPR-Cas9 and an Autoantigen Peptide for Restoring Specific Immune Tolerance. *ACS Appl. Mater. Interfaces* **12**, 48259–48271 (2020).

71. Karlsson, J., Rhodes, K. R., Green, J. J. & Tzeng, S. Y. Poly(beta-amino ester)s as gene delivery vehicles: challenges and opportunities. *Expert Opin Drug Deliv* **17**, 1395–1410 (2020).

72.   Krienke, C. *et al.* A noninflammatory mRNA vaccine for treatment of experimental autoimmune encephalomyelitis. *Science* **371**, 145–153 (2021).

73.   Prasad, S. *et al.* Tolerogenic Ag-PLG Nanoparticles Induce Tregs to Suppress Activated Diabetogenic CD4 and CD8 T Cells. *J Autoimmun* **89**, 112–124 (2018).

74.   Zhang, X. *et al.* Polymeric nanoparticles containing rapamycin and autoantigen induce antigen-specific immunological tolerance for preventing vitiligo in mice. *Human Vaccines & Immunotherapeutics* **17**, 1923–1929 (2021).

75.   Baranov, M. V., Kumar, M., Sacanna, S., Thutupalli, S. & van den Bogaart, G. Modulation of Immune Responses by Particle Size and Shape. *Front Immunol* **11**, 607945 (2021).

76.   Liu, M. *et al.* Old Dog New Tricks: PLGA Microparticles as an Adjuvant for Insulin Peptide Fragment-Induced Immune Tolerance against Type 1 Diabetes. *Mol. Pharmaceutics* **17**, 3513–3525 (2020).

77.   Freitag, T. L. *et al.* Gliadin Nanoparticles Induce Immune Tolerance to Gliadin in Mouse Models of Celiac Disease. *Gastroenterology* **158**, 1667-1681.e12 (2020).

78.   Firdessa-Fite, R. *et al.* Soluble Antigen Arrays Efficiently Deliver Peptides and Arrest Spontaneous Autoimmune Diabetes. *Diabetes* **70**, 1334–1346 (2021).

79.   Postigo-Fernandez, J., Firdessa-Fite, R. & Creusot, R. J. Preclinical evaluation of a precision medicine approach to DNA vaccination in type 1 diabetes. *Proceedings of the National Academy of Sciences* **119**, e2110987119 (2022).

80.   Rhodes, K. R., Meyer, R. A., Wang, J., Tzeng, S. Y. & Green, J. J. Biomimetic tolerogenic artificial antigen presenting cells for regulatory T cell induction. *Acta Biomaterialia* **112**, 136–148 (2020).

81.   Giang, S., Horwitz, D. A., Bickerton, S. & La Cava, A. Nanoparticles Engineered as Artificial Antigen-Presenting Cells Induce Human CD4+ and CD8+ Tregs That Are Functional in Humanized Mice. *Frontiers in Immunology* **12**, (2021).

82. Neshat, S. Y. *et al.* Improvement of Islet Engrafts via Treg Induction Using Immunomodulating Polymeric Tolerogenic Microparticles. *ACS Biomater Sci Eng* **9**, 3522–3534 (2023).

83. Rhodes, K. R. *et al.* Bioengineered particles expand myelin-specific regulatory T cells and reverse autoreactivity in a mouse model of multiple sclerosis. *Science Advances* **9**, eadd8693 (2023).

84. Clemente-Casares, X. *et al.* Expanding antigen-specific regulatory networks to treat autoimmunity. *Nature* **530**, 434–440 (2016).

85. Tsai, S. *et al.* Reversal of Autoimmunity by Boosting Memory-like Autoregulatory T Cells. *Immunity* **32**, 568–580 (2010).

86. Mikami, N. *et al.* Epigenetic conversion of conventional T cells into regulatory T cells by CD28 signal deprivation. *Proceedings of the National Academy of Sciences* **117**, 12258–12268 (2020).

87. Hawse, W. F., Cattley, R. T. & Wendell, S. G. Cutting Edge: TCR Signal Strength Regulates Acetyl-CoA Metabolism via AKT. *J.I.* **203**, 2771–2775 (2019).

88. Xu, L., Kitani, A. & Strober, W. Molecular mechanisms regulating TGF-β-induced Foxp3 expression. *Mucosal Immunol* **3**, 230–238 (2010).

89. Microneedle-Based Local Delivery of CCL22 and IL-2 Enriches Treg Homing to the Skin Allograft and Enables Temporal Monitoring of Immunotherapy Efficacy - Puigmal - 2021 - Advanced Functional Materials - Wiley Online Library. https://onlinelibrary.wiley.com/doi/10.1002/adfm.202100128.

90. Wang, Z. *et al.* Biodegradable and Antioxidant DNA Hydrogel as a Cytokine Delivery System for Diabetic Wound Healing. *Advanced Healthcare Materials* **11**, 2200782 (2022).

91. Encapsulation of Human Natural and Induced Regulatory T-Cells in IL-2 and CCL1 Supplemented Alginate-GelMA Hydrogel for 3D Bioprinting - Kim - 2020 - Advanced Functional

Materials - Wiley Online Library.

https://onlinelibrary.wiley.com/doi/full/10.1002/adfm.202000544.

92. Nagy, N. *et al.* Weekly injection of IL-2 using an injectable hydrogel reduces autoimmune diabetes incidence in NOD mice. *Diabetologia* **64**, 152–158 (2021).

93. A hydrogel platform for co-delivery of immunomodulatory proteins for pancreatic islet allografts - Medina - 2022 - Journal of Biomedical Materials Research Part A - Wiley Online Library. https://onlinelibrary.wiley.com/doi/10.1002/jbm.a.37429.

94. Safina, I. *et al.* Gold nanorods enhance different immune cells and allow for efficient targeting of CD4+ Foxp3+ Tregulatory cells. *PLOS ONE* **16**, e0241882 (2021).

95. de Picciotto, S. *et al.* Selective activation and expansion of regulatory T cells using lipid encapsulated mRNA encoding a long-acting IL-2 mutein. *Nat Commun* **13**, 3866 (2022).

96. Eskandari, S. K. *et al.* Regulatory T cells engineered with TCR signaling–responsive IL-2 nanogels suppress alloimmunity in sites of antigen encounter. *Science Translational Medicine* **12**, eaaw4744 (2020).

97. Marshall, G. P. *et al.* Biomaterials-based nanoparticles conjugated to regulatory T cells provide a modular system for localized delivery of pharmacotherapeutic agents. *Journal of Biomedical Materials Research Part A* **111**, 185–197 (2023).

98. Spangler, J. B. *et al.* Antibodies to Interleukin-2 elicit selective T cell subset potentiation through distinct conformational mechanisms. *Immunity* **42**, 815–825 (2015).

99. VanDyke, D. *et al.* Engineered human cytokine/antibody fusion proteins expand regulatory T cells and confer autoimmune disease protection. *Cell Reports* **41**, 111478 (2022).

100. Trotta, E. *et al.* A human anti-IL-2 antibody that potentiates regulatory T cells by a structure-based mechanism. *Nat Med* **24**, 1005–1014 (2018).

101. Lei, J. *et al.* FasL microgels induce immune acceptance of islet allografts in nonhuman primates. *Science Advances* **8**, eabm9881 (2022).

102.   Coronel, M. M. *et al.* Immunotherapy via PD-L1–presenting biomaterials leads to long-term islet graft survival. *Science Advances* **6**, eaba5573 (2020).

103.   Francisco, L. M. *et al.* PD-L1 regulates the development, maintenance, and function of induced regulatory T cells. *Journal of Experimental Medicine* **206**, 3015–3029 (2009).

104.   Wang, L. *et al.* Programmed death 1 ligand signaling regulates the generation of adaptive Foxp3+CD4+ regulatory T cells. *Proceedings of the National Academy of Sciences* **105**, 9331–9336 (2008).

105.   Piao, W. *et al.* PD-L1 signaling selectively regulates T cell lymphatic transendothelial migration. *Nat Commun* **13**, 2176 (2022).

106.   Zhulai, G. & Oleinik, E. Targeting regulatory T cells in anti-PD-1/PD-L1 cancer immunotherapy. *Scandinavian Journal of Immunology* **95**, e13129 (2022).

107.   Riella, L. V. *et al.* Deleterious Effect of CTLA4-Ig on a Treg-Dependent Transplant Model. *American Journal of Transplantation* **12**, 846–855 (2012).

108.   Barra, J. M. *et al.* Localized cytotoxic T cell–associated antigen 4 and antioxidant islet encapsulation alters macrophage signaling and induces regulatory and anergic T cells to enhance allograft survival. *American Journal of Transplantation* (2023) doi:10.1016/j.ajt.2023.01.007.

109.   Paez-Mayorga, J. *et al.* Implantable niche with local immunosuppression for islet allotransplantation achieves type 1 diabetes reversal in rats. *Nat Commun* **13**, 7951 (2022).

110.   MacMillan, M. L. *et al.* First-in-human phase 1 trial of induced regulatory T cells for graft-versus-host disease prophylaxis in HLA-matched siblings. *Blood Advances* **5**, 1425–1436 (2021).

Chapter 3

Precise surface functionalization of PLGA particles for

human T cell modulation

A. ABSTRACT

The biofunctionalization of synthetic materials has extensive utility for biomedical applications but approaches to bioconjugation typically show insufficient efficiency and controllability. We recently developed an approach by building synthetic DNA scaffolds on biomaterial surfaces that enables the precise control of cargo density and ratio, thus improving the assembly and organization of functional cargos. We used this approach to show that the modulation and phenotypic adaptation of immune cells can be regulated using our precisely functionalized biomaterials. Here, we describe the three key procedures including the fabrication of polymeric particles engrafted with short DNA scaffolds, the attachment of functional cargos with complementary DNA strands, and the surface assembly control and quantification. We also explain the critical checkpoints needed to ensure the overall quality and expected characteristics of the biological product. We provide additional experimental design considerations for modifying the approach by varying the material composition, size, or cargo types. As an example, we cover the use of the protocol for human primary T cell activation and for the identification of parameters that affect ex vivo T cell manufacturing. The protocol requires users with diverse expertise ranging from synthetic materials to bioconjugation chemistry to immunology. The fabrication procedures and validation assays to design high-fidelity DNA-scaffolded biomaterials typically require 8 days.

B. INTRODUCTION

B.1. Introduction

Synthetic materials have been widely engineered to present biomolecules to engage cellular receptors and control cell behaviours for disease modulation[1–4]. In particular, immunotherapies show potential as treatment options for conditions including some types of cancers and autoimmune diseases[5–9]. In both clinical use and preclinical models, these treatments are mostly administered as in vivo immunomodulatory agents, such as antigens, antibodies, and cytokines, or as cellular therapies involving ex vivo stimulation and/or engineering to control disease[10–16]. Immune cells in fact respond to signals from cell-cell synapses and the extracellular space to determine their phenotype, fate, and behaviors[17–19]. Therefore, methods capable of precisely controlling the signals presented to immune cells may enable the engineering of cell therapeutic products with improved therapeutic efficacy or other benefits[3,20,21].

Although the immobilization of stimulatory ligands on biomaterial surfaces can mimic the natural signals for immune cell programming[22–24], the efficient and controllable conjugation of multiple ligands on synthetic surfaces is a major challenge of traditional chemical approaches[25–28]. Thus, we developed a synthetic short DNA-scaffold strategy for surface biofunctionalization[20]. This plug-and-play approach can precisely control the density and ratios of multiple functionalities with rapid surface assembly. This biofunctionalization approach can be used in various applications and requires the careful assembly of synthetic materials, oligonucleotides, and proteins. Here, we provide the step-by-step description to fabricating DNA-scaffolded particles, engineering complementary-DNA (compDNA) conjugated biomolecules, and applying these materials to activate human primary T cells ex vivo. This protocol further provides detailed methods and quality control assays to ensure a high fidelity of functional biomaterials and an optimal activation of human T cells.

B.2. Applications

We initially tested the approach to present agonistic αCD3 and αCD28 antibodies onto biodegradable polymeric microparticles composed of poly-lactic-co-glycolic acid (PLGA). These immune cell engaging particles (ICEp) activate T cell receptor and co-stimulatory receptors for human T cell ex vivo expansion, which is a key step for manufacturing T cell-based therapies[5,29]. Due to the biodegradable and biocompatible properties of ICEps, they did not need to be removed from ex vivo cultures compared to using commercially available magnetic particles (e.g. Dynabeads)[20]. The quantitative control of αCD3 and αCD28 antibodies showed an impact on both T cell expansion fold and phenotypic outcomes—in terms of differentiation fate and exhaustion—which are critical aspects for therapeutic uses[20,30–32]. In addition, these materials can be administered in vivo to control immune cell activities and can be tailored for both localized delivery—such as intratumor or subcutaneous injection—and systemic delivery through intravenous administration[20,33]. For example, logic-gated CAR-T cells have been engineered to recognize dual-antigens to minimize "off-tumor" toxicity, and we engineered microparticles presenting synthetic antigens to prime these T cells to target tumor specific antigens[34]. With the intratumoral injection of antigen-functionalized microparticles, we were able to restrict the activation of these logic-gated CAR-T cells locally to minimize systemic toxicity[20]. While this protocol will focus primarily on the quality control of ICEp fabrication and the uses in vitro, readers are encouraged to consult the original report on this technology for additional details on in vivo use[20].

The customizability of this approach facilitates a wide range of other applications where the precision control of multiple biomolecules is needed, for example, targeted drug delivery, gene engineering, and tissue remodeling[35–38]. An effective intracellular delivery of gene regulatory-or- editing molecules must overcome various barriers at the tissue, cell, and

intracellular (e.g., endosomes and lysosomes) levels, which can be facilitated using different biological functionalities[1,2,39]. Similarly, the precision density control of ligands for cellular receptors involved in tissue remodeling—for example, integrin and adhesion signaling—can provide avenues for tissue engineering[35]. The approach is also adaptable for drug loading within the particle core, and polymers with different degradation profiles can be leveraged for controlled release[33,40]. Particle size can be varied across multiple length-scales, enabling systemic delivery or localized retention[41,42]. Through the joint engineering of the DNA scaffold and underlying polymer, this approach can be reformulated to fit multiple biological challenges and thus displays unprecedented levels of control for cell modulation and therapeutic applications.

B.3. Development of the protocol

This protocol describes the fabrication of 1) DNA-scaffolded PLGA particles, 2) bioconjugation of biomolecules (e.g. antibodies) with compDNA, 3) compDNA-biomolecule conjugate assembly onto DNA scaffolds, and 4) primary human T cell activation and phenotyping using ICEp (**Fig. 3.1**). The high controllability of surface functionalization requires a dense layer of DNA scaffolds built on the particle surface which depends on the efficient conjugation of the PLGA-PEG-Maleimide (PLGA-PEG-Mal) with thiolated-DNA (thiol-DNA) and is susceptible to poor reagent quality and improper reaction conditions (**Fig 3.2**). Thus, we developed a framework for testing PLGA-PEG-DNA conjugation efficiency among different lots of precursor materials and correlated this with the DNA-scaffold density of the resultant particles. After validating successful polymer conjugation, PLGA-PEG-DNA batches bearing different DNA- sequences can be mixed at select ratios, which will reflect the final DNA-scaffold ratio on particles.

Generating compDNA-biomolecule conjugates requires careful design to preserve the activity of the biomolecule during conjugation and surface attachment (**Fig. 3.3**)[43–45]. For example, in antibody conjugation, tris(2-carboxyethyl)phosphine hydrochloride (TCEP) is used to selectively reduce hinge-region disulfide bonds to free thiol groups for thiol-DNA conjugation[46]. The TCEP molar excess and the reaction duration are important parameters for maintaining antibody function[47]. After DNA-conjugation, a critical concern is the removal of unreacted DNA which can compete for surface loading in later steps and thus requires affinity-based chromatography methods for purification due to electrostatic interactions between DNA and antibody. After the rapid surface assembly of purified antibody-DNA (Ab-DNA) conjugates, a flow cytometry- based method is provided to quantify the particle surface loading (**Fig. 3.4**).

When using ICEps for T cell activation, we found that culture seeding conditions, including the cell density, particle-to-cell ratio, and surface ratio of stimulatory biomolecules all influence T cell expansion and resultant phenotype (**Fig. 3.5**). For example, in our original report we enriched either memory or effector T cell fates through the control of particle compositions including the ratiometric control of agonistic αCD3 and αCD28 antibodies on the particle surfaces[20]. Here, we intend to highlight the influence of these parameters on T cell activation and manufacturing so that they can be taken into consideration for related research. While the focus is on using 2 μm (mean diameter) ICEPs for T cell activation, this fabrication protocol is compatible with multiple particle size-scales, thus we have provided protocol modifications throughout.

B.4. Comparison with other methods

An often-used approach for surface functionalization is through covalent conjugation between functional groups on the synthetic material and the biomolecule using a bifunctional

linker (e.g., PEG linker with NHS and Maleimide groups at the end-sites)[26,27,48]. However, the efficiency of this method is severely limited by surface steric hinderance and the instability of the functional groups[49–51]. While orthogonal chemistries provide an additional dimension of control for immobilizing multiple biomolecules species, they still suffer from the same limitations inherent to covalent surface attachment strategies[49,50]. Further, it becomes increasingly difficult to tune the surface stoichiometry of multiple biomolecule species, as characteristics of the biomolecule heavily influence their attachment—including molecular weight and charge[20,54]. In comparison, our DNA hybridization-based approach reaches the theoretical surface saturation limit while simultaneously maintaining independent control over the loading of each biomolecule species. Another surface functionalization approach to load multiple cargos is to use streptavidin- handles[21,22]. We previously found that the ratiometric control is largely affected by the molecular weight and charge of the cargo, where the species with highest surface affinity always outcompeted the others. Also, the maximal density of smaller molecules may be bottlenecked by the size of streptavidin.

B.5. Limitations

There are three areas of limitations in adapting DNA-scaffolded materials: 1) broad skillset and equipment required to combine synthetic materials, bioconjugation methods, and biological applications, 2) variations in precursor material quality, and 3) many steps involved throughout the whole protocol. We have adapted existing technologies commonly available in biological research labs for characterizing fabricated materials (e.g., gel electrophoresis, Nanodrop spectrophotometers, flow cytometers, etc.). Most polymers, linkers, and synthetic DNAs are commercially sourced to facilitate user adoption. For precursor quality, we have identified that PLGA-PEG-Mal was the main source of quality variation, possibly due to reactant

impurities remaining in the purchased polymer; we have included methods for evaluating this precursor quality.

B.6. Experimental Design

Particle size: This protocol can be adapted for fabricating spherical particles across varying size-scales while maintaining the functionality of the DNA-approach (**Fig. 3.2g-h**). Here, PLGA-PEG-DNA serves as the sole surfactant which correlates well with particle size control. Different quantification methods are needed for size quantification; micron-scale requires microscopy whereas nano- scale requires either Zetasizer or Nanosight. The protocol exhibits minimal batch-to-batch variation, although large particle sizes are associated with greater size distribution variance which has been reported with probe-sonication methods[55]. Thus, alternative methods for better size-control could be evaluated for compatibility with the DNA-scaffolding method, including post-fabrication size-filtration, differential centrifugation, or even alternatives to probe- sonication such as microfluidic droplet-generators or electrospray fabrication.

Surface density control: There are two methods for controlling the surface density of biomolecules: varying the DNA- scaffold density during particle fabrication or limiting the input quantity of compDNA- biomolecule conjugates during hybridization[20]. The first method was demonstrated previously by varying the molar excess of thiol-DNA to PLGA-PEG-Mal during polymer-DNA conjugation, while keeping the input amount of PLGA-PEG-Mal constant for particle fabrication[20]. The second method of density control involves titrating the compDNA-biomolecule below the surface saturation level (**Fig. 3.4a-c**), which is more convenient as it shares the same particle formulation and is used within this protocol.

Surface ratiometric control: Ratiometric control of biomolecules is achieved similarly as density control during either particle fabrication or surface hybridization. The surface ratios of scaffold DNA sequences are controlled by the input mixtures of PLGA-PEG-DNAs during particle fabrication. Thus, addition of excess compDNA-biomolecules will present the biomolecules in a ratio defined by the scaffold DNA ratio (**Fig. 3.4f-h**). In contrast, the hybridization method involves inputting a pre-defined ratio of compDNA-biomolecules below the saturation level of each respective scaffold DNA-sequence, allowing the input biomolecule stoichiometry to define the surface ratio outcome (**Fig. 3.4d,e**).

Particle core loading: While not described within the procedural section, an additional functionality of our material is the capacity for core-loading biomolecules and tracking dyes. Fluorescent dye can be pre- conjugated to PLGA (e.g AlexaFluors) and mixed during particle fabrication for in vitro or in vivo tracking. Biomolecules of interest can be loaded into the core for slow-release via a double- emulsion procedure[40,56].

Particle biodegradability: We have adopted PLGA due to its biocompatibility and tunable degradation, as degradation rates can be controlled by varying the chain lengths or lactic-to-glycolic acid ratios[40,56]. Different polymers with varying stabilities can alter the release-rates of core-loaded biomolecules[57,58]; we have shown that other polymers, such as poly-lactic acid (PLA), are also compatible with the DNA-approach technology but requires additional optimization.

Protein-DNA conjugation: There are many protein bioconjugation chemistries available which should be balanced with conjugation efficiency, cost, and maintenance of biomolecule activity[43,44,48,59,60]. Alternatively, a protein tag (e.g. SNAP-tag) can be incorporated at an optimal site of the protein to link with the functional group of the DNA[61,62]. To note, it is necessary to validate protein bioactivity post- conjugation through assays relevant to the biological function.

Protein-DNA storage: The purification procedure for removing unreacted DNA typically results in low Ab-DNA concentration reduce its stability. Further, long-term storage in solution is not advisable due to the risk of protein degradation[63–65]. Lyophilization has been used to improve long-term protein storage and is also used here to facilitate increased protein concentrations after resuspension— this can improve stability and minimize particle hybridization volumes as described later in "Particle surface loading of antibody". Biomolecules that are unstable or sensitive to freezing will require protein-specific bioactivity assays to verify minimal bioactivity loss and to decide whether lyophilization is appropriate. Previously, spin-concentrator columns were used to increase protein concentration, but this resulted in significant protein loss onto the concentrator membrane, and this was more apparent when using DNAs labelled with charged fluorescent dyes.

T cell sourcing and expansion using ICEp: Peripheral blood mononuclear cells (PBMCs) can be isolated from whole-blood or leukaphereses products and can be used without further purification or processed in a variety of ways to collect desired T cell fractions[29,66,67]. Cells can be separated on a variety of markers using commercially available positive or negative selection binding kits. To further enhance population purity and/or collect T cell subsets, such as regulatory T cells (Tregs) or naïve T cells, fluorescence-activated cell sorting (FACS) can be used. Isolated cells can be stimulated using a combination of TCR-and-costimulatory activating proteins and growth factors. The former is provided via ICEPs presenting agonistic αCD3 and αCD28 antibodies while mitogenic cytokines (e.g., IL-2) are provided as soluble supplementation in the medium. For the latter, while we are providing cytokine in the media, we and others have identified advantages for surface-delivery of growth factors which is compatible with ICEp technology[20,22,68]. Various cell-culture parameters using ICEp can influence overall expansion and should be optimized for each cell-type and experimental timeline, including: 1) choice of the culture plate, 2) cell seeding and maintenance densities, 3) cytokine

concentrations, and 4) particle-to-cell ratio[69]. Following expansion, T cells may be analyzed using flow cytometry.

Critical controls: There are numerous controls which are important in 1) determining PLGA and DNA quality, 2) surface loading of biomolecules onto the PLGA-DNA scaffold, and 3) biomolecule activity after DNA-conjugation. Determining the quality of the precursors for PLGA-PEG-DNA fabrication requires gel-electrophoresis, thus we suggest using commercially synthesized oligos to serve as an unreacted-DNA band control. This serves to identify the unreacted DNA fraction within the PLGA-PEG-DNA lanes, enabling the calculation DNA consumption during conjugation which is used as a proxy for PLGA conjugation efficiency.

For quantifying particle biomolecule loading, it is necessary to have a fluorescent standard ladder when using a plate spectrophotometer or, when using flow cytometry, have both un-hybridized and saturated single-color particle controls. The fluorescent biomolecule used in either case should match the biomolecule hybridized onto particles. For flow cytometry, batch-to-batch variation in particle size could result in dissimilar fluorescence intensities, thus control and experimental particles should come from the same common stock. For the biological activity of Ab-DNA conjugates, cell-staining titrations should be compared with unmodified antibody controls and measured via flow cytometry to detect changes over time or between conjugation batches. To minimize variation, a large batch of Ab-DNA should be aliquoted and either frozen or lyophilized immediately after conjugation. Smaller aliquots from this stock could serve as standards when comparing to new conjugations. Similarly, when loading particle with biomolecule-DNA conjugates, it may be beneficial to hybridize a large batch of particles and lyophilize them in aliquots for each future experiment.

C. MATERIALS

C.1. Biological materials

PBMCs are isolated from leukapheresis products collected from healthy donors (StemCell Technologies). *Caution: for working with primary human blood products, the appropriate approvals, trainings, and safety procedures should be followed according to institutional guidelines.*

C.2. Reagents:

See **Supplemental Table S3.1.** for full list of reagents, equipment, and software.

D. REAGENT SETUP

DNA reagents (thiol-DNA and compDNA): Calculate volume needed to resuspend DNA to 500 µM. Resuspend using 10 mM HEPES, pH 7.0 Allow for 30 minutes to resuspend, vertexing occasionally. Store at -20°C.

5x Particle fabrication buffer, 50 mM sodium citrate, 1.5 M sodium chloride, 10 mM magnesium chloride, pH 3.0: Weigh out 735 mg of sodium citrate, 4.38 g of sodium chloride, and 47.61 mg of magnesium chloride. Add into a container with 50 mL of deionized water and mix. Measure pH using a pH meter and adjust to pH 3.0 using concentrated hydrochloric acid. Transfer to conical tubes and store at room temperature (20-25℃).

2x DNA hybridization buffer, 600 mM sodium chloride, 2 mM magnesium chloride, 0.02% Tween 20, pH 7.0: Weigh out 1.75 g of sodium chloride and 9.52 mg of magnesium chloride. Add into a container with 50 mL deionized water. Add 10 µL of Tween 20, using a dilution in water if the stock is too viscous to accurately measure. Thoroughly mix and measure pH using a pH meter and adjust to pH 7.0. Store at room temperature.

5x Protein G binding buffer, 100 mM sodium phosphate, 0.75 M sodium chloride, pH 7.0: Weigh out 3.0 g of sodium phosphate monobasic and 10.88 g sodium chloride. Add into a container with 250 mL of deionized water. Thoroughly mix and measure the pH using a pH meter and adjust to pH 7.0. Store at room temperature.

Protein G acidic elution buffer, 0.1 M glycine, pH 2.7: Weigh out 375.35 mg of glycine and add to a container with 50 mL deionized water. Thoroughly mix and measure the pH using a pH meter and adjust to pH 7.0 using concentrated hydrochloric acid. Store at room temperature.

Protein G basic elution buffer, 0.1 M glycine, pH 10.0: Weigh out 375.35 mg of glycine and add to a container with 50 mL deionized water. Thoroughly mix and measure the pH using a pH meter and adjust to pH 7.0 using concentrated sodium hydroxide. Store at room temperature.

10x Protein G acidic neutralization buffer, 1 M Tris-HCl, pH 8.5: Measure out 50 mL of 1 M Tris-HCl in a secondary container. Measure the pH using a pH meter and adjust to pH 8.5 using concentrated sodium hydroxide. Store at room temperature.

10x Protein G basic neutralization buffer, 1 M Tris-HCl, pH 6.5: Measure out 50 mL of 1 M Tris-HCl in a secondary container. Measure the pH using a pH meter and adjust to pH 6.5 using concentrated hydrochloric acid. Store at room temperature.

PBS-FBS wash buffer, 1x Ca^{2+}/Mg^{2+} free PBS, 3% (vol/vol) FBS, 1 mM EDTA: In a sterile BSC, combine 15 mL of heat-inactivated FBS, 484 mL of 1x PBS, and 1 mL of 0.5 M EDTA in a container and mix. Mix and sterile-filter the solution using a 0.22 μM filter. Store at 4°C.

T cell medium: In a sterile BSC, combine 435 mL of RPMI 1640 + Glutamax, 50 mL of heat-inactivate FBS, 5 mL of 1 M HEPES, 5 mL of 100 mM sodium pyruvate, and 5 mL of combined

Penicillin (1 x 10^4 U/mL) + Streptomycin (10 mg/mL). Mix and sterile-filter the solution using a 0.22 μM filter and store at 4°C. Prior to experimental use, aliquot 50mL of media into a separate container and add 25 μL of hIL2 (2 x 10^5 U/mL stock) to a final concentration of 100 U/mL. Media containing hIL2 (complete T cell media) can be used for T cell culturing and should be used within 1 week and stored at 4°C.

Freezing medium, 10% (vol/vol) DMSO in FBS: In a sterile BSC, combine 22.5 mL of heat-inactivated FBS and 2.5 mL of DMSO. Sterile-filter using a 0.22 μM filter and store at 4°C.

E. PROCEDURE

E.1. PLGA-PEG-DNA conjugate synthesis (Timing 2d):

Critical: The following describes the synthesis of 500 nmol PLGA-PEG-DNA using commercially synthesized PLGA-PEG-Mal and thiol-DNA precursors. See **Table 3.1** for validated DNA-sequence options. Repeat the procedure for each desired oligo sequence.

1. Use a micropipette to transfer 500 nmol of thiol-DNA into a 1.5 mL microcentrifuge tube (DNA-tube).
2. Add 100 µL of 500 mM TCEP (100x molar excess to thiol-DNA) to reduce any inter- strand disulfide bonds and incubate for 1.5 hours at 37°C.
3. Prepare a Glen size-exclusion desalting column that is appropriately sized for DNA-tube volume using 10 mM EDTA in 10 mM Tris-HCl (1x TE, pH 7.5) for buffer exchange washes, per the manufacturer's instructions.
4. Buffer exchange the TCEP-reduced thiol-DNA into 1x TE (pH 7.5) using the prepared Glen column to collect the DNA-containing flow-through.

Critical Step: The exchange buffer should not contain any chemical groups which react with the selected conjugation chemistry. EDTA prevents disulfide reformation following reduction.

5. For DNA precipitation, aliquot the thiol-DNA into 1.5 mL tubes (precipitation tubes) with ~400 µL per tube. To each 400 µL tube, add 50 µL of 3 M sodium acetate (pH 5.0) and 1.3 mL of ethanol (200 proof); thoroughly mix and vortex after each addition. Cool tubes at -20°C for 30 minutes.
6. Centrifuge the precipitation tubes at 18000 *g* for 10 minutes at 4°C. Remove the supernatant and either air-dry or use a pressurized air-line to further dry the DNA-pellet.
7. Resuspend the DNA-pellet in one precipitation tube with 200 µL of TE. Combine this volume into another precipitation tube and repeat until all tubes are resuspended in a total of 200 µL

(targeting ~2.5 mM DNA if DNA loss was minimal during preceding steps).

Critical Step: DNA should be resuspended in less than 200 µL to be compatible with the optimized reaction conditions later. Adjust this volume appropriately and reoptimize if needed.

8. Measure the absorbance at 260 nm (A260) of a diluted sample of DNA using Nanodrop. Reference **Table 3.1** for the relevant extinction coefficients and calculate the stock concentration using Beer's law:

Stock Concentration= [(Dilution Factor) x (Absorbance)] / [(extinction coefficient) x (path length)] where Nanodrop path length is 1 cm and the extinction coefficients used here are in the units of $M^{-1} * cm^{-1}$.

9. Create a reaction-template in Excel to facilitate reagent calculations for synthesizing the PLGA-PEG-DNA. Refer to **Table 3.2** for the necessary equations and constants for constructing the template. An example template is provided in **Supplementary File 1** (found online using DOI listed herein).

Critical Step: The PLGA-PEG-Mal:DNA ratio should be optimized for each new polymer lot.

Critical Step: Use PLGA-PEG-Mal molecular number average instead of weight average due to the distribution of different polymer chain lengths. The number average here is specific to our PLGA-PEG-Mal lot.

10. Allow the PLGA-PEG-Mal container to warm to room temperature before opening.

Critical Step: Allowing the container to warm to room temperature before opening to avoid water condensation, which can hydrolyze the functional group.

11. Weigh the calculated amount of PLGA-PEG-Mal and add DMF to achieve a 30 mg/mL solution.

12. Add the solutions to a 15 mL tube in the following order, referring to the volumes in the

reaction template: 1) extra TE buffer, 2) DNA solution, 3) triethylamine, 4) Extra DMF, 5) PLGA-PEG-Mal DMF solution. Vortex to mix.

13. Wrap the top of the tube with parafilm and shake overnight using an orbital shaker at room temperature.

14. Use nitrogen or other inert gas line to back-fill the stock container of PLGA-PEG-Mal.

15. Wrap the container with parafilm before putting back into -20°C storage.

16. The next day, briefly vortex the PLGA-PEG-DNA reaction tube and aliquot into 1.5 mL tubes with ~500 μL into each tube. As ratiometric particles may be desired, it is recommended to premix PLGA-PEG-DNA bearing different sequences at a specified ratio before drying, ensuring that 100 nmol of total PLGA-PEG-DNA is aliquoted per tube.

Critical Step: The downstream fabrication protocol uses 100 nmol of PLGA-PEG-DNA, thus aliquoting 500 μL equates to a theoretical 100 nmol of PLGA-PEG-DNA (assuming 200 μM was the target PLGA-PEG-Mal reaction concentration). Premixing the different PLGA-PEG- DNA sequences prior to drying ensures more precise control over the mixture ratio, whereas later the volumes may be difficult to control due to solvent evaporation.

17. Dry the PLGA-PEG-DNA aliquots in a vacuum centrifuge at 70°C for 2-3 hours.

18. Once dried, store at -20°C.

Pause Point: Dried PLGA-PEG-DNAs are stable for over a year. PLGA-PEG-DNA can be stable if dissolved in organic solvent, although any aqueous solutions should be avoided as this will lead to hydrolysis of either the PLGA ester linkages or the thiol-maleimide bond.

19. Urea-PAGE is used to verify PLGA-PEG-DNA conjugation (**Fig. 3.2b-c**).

20. Prepare ~20 μL of a 0.2 μM solution of PLGA-PEG-DNA (diluted in 1x TE) and dilute to 0.1 μM using 20 μL of 2x Urea-PAGE loading buffer.

21. Similarly, make a 0.1 μM dilution of pure-DNA (in loading buffer) used for the reactions.

22. Heat the sample for 3 minutes at 70°C.

23. During heating, prepare a Urea-PAGE gel by loading a vertical gel-chamber with 1x TBE buffer and pre-running the gel for 10 minutes at 120 V. Use a syringe or pipette to clean the melted gels in each lane using TBE buffer within the chamber.

24. Load 1 pmol (~10 μL) of 0.1 μM sample in triplicate alongside 1 pmol of control pure- DNA lanes. Run the gel for 1.5 hours at 120 V.

25. Prepare a 25 mL of 1x Sybr Gold (10000x dilution) in 1x TBE.

26. Dispense into a wide disposable glass dish, cover the dish with the lid, and protect from light.

27. After the gel has finished running, release the gel from the cast and transfer to the 1x Sybr Gold solution.

28. Place onto an orbital shaker at room temperature for 5-10 minutes protected from light.

29. Rinse the stained gel with 1x TBE and transfer into a new glass dish containing buffer to prevent gel dehydration.

30. Image the gel using a gel-doc reader or laser scanner.

31. Import the gel image into ImageJ. After adjusting brightness and contrast, perform gel densitometry analysis as described by the ImageJ operational manual (see "Software")[70].

32. Use the intensity of the top PLGA-PEG-DNA band and the lower, unreacted DNA to calculate the efficiency of the reaction using the equation below and record to track batch variation:

(Intensity PLGA-PEG-DNA) / (Intensity PLGA-PEG-DNA + Intensity DNA)

Critical Step: Disulfide bonds can form between the thiol-DNA and can appear in the gel above the unreacted (**Fig. 3.2b**). We typically do not include the disulfide band intensity since it is negligible relative to the main unreacted thiol-DNA band.

E.2. PLGA particle fabrication (Timing 6h):

Critical: This procedure describes the fabrication of 2 μm particles bearing a maximally dense surface DNA scaffold at 1:1, R:G DNA-sequence ratios (see **Table 3.1** for sequence information), where R and G are different DNA sequences. This procedure assumes that 100 nmol of PLGA- PEG-DNA was dried in Step 18 with a 1:1 mixture of DNA -G and -R sequences (PLGA-PEG-G and PLGA-PEG-R, respectively). 100 nmol of PLGA-PEG-DNA generates ~100 OD_{550} in 400 μL volume (40 OD_{550} in 1 mL) or approximately 2 x 10^9 particles. For fabricating particles of other target diameters, refer to **Table 3.3** for modifying reagent amounts within this section and to the "Anticipated Results" for representative morphologies and size distributions (**Fig. 3.2g-h**).

33. Weigh 50 mg of unmodified PLGA 50:50 (38-54 kDa, PLGA) into a 15 mL tube (fabrication tube).

34. Use a glass pipette to add 400 μL of ethyl acetate (EtOAc) into the tube.

Critical Step: Keep EtOAc containing tubes open for as little time as possible to minimize evaporation—this will reduce the size variability between batches. Do not hold tubes near the liquid as this may contribute to heating.

35. Wrap the tube with parafilm and place vertically on a shaker table overnight to dissolve.

36. The next day, place stock tubes of EtOAc, water, and fabrication tube on ice to reduce evaporation when opened.

37. Resuspend the 1:1 R:G PLGA-PEG-DNA tube from Step 18 with 100 μL of water and 100 μL of EtOAc. Reuse this pipette tip whenever transferring PLGA-PEG-DNA for a given sequence ratio (switch if using a different sequence ratio).

38. Place the PLGA-PEG-DNA tube into the bath sonicator for 10 minutes or until fully resuspended.

39. Transfer the PLGA-PEG-DNA into the 15 mL fabrication tube in 100 µL increments to reduce material loss inside the pipette tip.

40. To wash the PLGA-PEG-DNA tube, add 300 µL of water and 100 µL of 5x particle fabrication buffer (see "Reagent Setup").

41. Using the saved PLGA-PEG-DNA pipette tip, transfer this solution into the fabrication tube. If the pipette tip gets clogged, briefly pipette the EtOAc fraction within the fabrication tube to dissolve the clog.

42. Sonicate the fabrication tube and vortex until mixed. Place the fabrication tube on ice.

43. Place a magnetic stir plate with a 250 mL beaker and a stir magnet into a fume hood. This will be needed after probe sonication after Step 50.

44. Prepare a 50 mL conical tube partially filled with ice to act as a secondary container for the fabrication tube during probe sonication. Set up a vortexer, 0.2% (wt/vol in water) PVA, and separate ice container near the probe sonicator.

45. For the sonication setup, clean the sonication microtip probe using 70% (vol/vol in water) ethanol and allow to dry.

Critical Step: Ensure that the sonication program is set to the recommended settings (**Box 3.1**). Sonication will need to pause halfway through, so if your sonicator does not allow for this function then adjust the number of cycles accordingly.

46. Vortex the reaction tube and place into the 50 mL secondary ice container.

47. Position the sonication probe into the fabrication tube solution, avoiding the tube walls.

48. Initiate the sonication program, moving the microtip throughout the solution to ensure a more homogenous sonication. After two cycles, pause sonication and vortex the reaction tube before finishing the remaining cycles.

49. Immediately after sonication add 9 mL of 0.2% (wt/vol) PVA into the fabrication tube, invert to mix, then vortex.

50. Dispense the contents of fabrication tube into the 250 mL beaker from Step 43 and turn on the magnetic stirrer for ~2.5 hours without any heating.

Critical Step: This step will evaporate the EtOAc residue. For larger volumes, use a rotary evaporator.

*See Troubleshooting (**Table 3.5**)*

51. After 2.5 hours, place a 40 µm filter onto a 50 mL conical tube and pour the particle solution through the filter. Use a micropipette to transfer any remaining solution.

52. Centrifuge the particle tubes at 225 g for 10 minutes.

Critical Step: If nanoparticles were fabricated, then after Step 52 the supernatant will contain the nanoparticles while any large particle contaminants will be contained within the pellet. If larger microparticles (>2 µm) were fabricated, then proceed as written without protocol modification.

53. Discard the supernatant and resuspend in 2 mL of TE containing 0.1% (vol/vol) Tween 20 (TE-Tween) using a micropipette.

Critical Step: If nanoparticles were fabricated, then collect the supernatant and discard any visible pellet after Step 52. For all subsequent nanoparticle centrifugation steps in this protocol, spin at 16000 g for 10 minutes.

54. Distribute the 2 mL into smaller microcentrifuge tubes and centrifuge at 6000 g for 5 minutes.

55. Resuspend each tube in 200 µL of TE-Tween.

56. Spin again at 6000 g for 5 minutes, resuspending again in 200 µL TE-Tween. During the final resuspension, combine all tubes into a single tube with a total volume of ~400 µL TE-Tween.

57. Prepare a small sample for Nanodrop quantification. Since the stock concentration is large, use a larger dilution volume to allow for sufficiently large pipetting volumes from the stock

solution (~0.5-1 µL). Assuming a successful fabrication yield of ~100 OD550 in 400 µL, use the dilution example below to generate a dilution of ~0.5 OD550:

A.   Generalized dilution equation used: C1 * V1 = C2 * V2

B.   (100 OD550 stock) * (X µL stock sampled) = (0.5 OD550 target concentration) * (100 µL total dilution volume) ; X µL stock sampled = 0.5 µL

C.   (Total dilution volume) – (X µL stock sampled) = (Volume of TE-Tween to dilute stock sample) ; Volume of TE-Tween to dilute stock sample = 99.5 µL

D.   Dilution Factor = (Total dilution volume) / (Volume of stock sampled) ; Dilution Factor = 200

Critical Step: Nanodrop particle absorbance is linear between 0.2 and 1.0 at OD550, so the estimated dilution fold would need to be adjusted accordingly. The estimate of 0.5 used above is an appropriate initial target as some amount of error will likely maintain the measured range between 0.2 and 1.0.

Critical Step: Microparticles settle quickly, creating a concentration gradient and a particle pellet over time. Whenever handling microparticles, ensure the tubes are sufficiently resuspended.

58. After using an appropriate buffer (TE-Tween) to blank the Nanodrop, measure the OD550 of the diluted sample and solve for the stock concentration via the equation below and using the Dilution Factor calculated in Step 57. If the measured OD550 is below 0.2 then remake the dilution using a lower dilution factor.

A. (Stock OD550) = (Dilution Factor) * (Measured OD550 of diluted sample)

59. Using the equation from Step 57, set aside a small sample of diluted particles to generate ~20 µL at 5-10 OD550. Save this sample for imaging and size-quantification later.

Critical Step: For nanoparticles, refer to Step 99 for the necessary sample amount and the dilution concentration for Zetasizer measurements.

60. To each ~400 µL tube of particles, add 100 µL of 5% (wt/vol) PVA and mix.

61. In a secondary container, prepare a small volume of liquid nitrogen.

62. Flash-freeze the tubes by submerging in liquid nitrogen below the cap-level using a tube holder (e.g. long-forceps).

63. Place the frozen tubes into a lyophilization chamber for 24 hours with the tube caps open.

Pause point: Lyophilized particles can be stored for up to two years at -20°C. Particles stored after two years should be reassessed for DNA-scaffold density (see "Particle surface DNA loading analysis")

E.3. Particle surface DNA loading analysis (Timing 4h):

Critical: This protocol describes the quantification of particle scaffold DNA density and relative ratio of DNA sequences via the detection of hybridized, fluorescently labeled compDNA (5' end label) using a plate spectrophotometer. The procedure assumes particles are taken from lyophilized stock. The total particle amount required for fluorescent detection varies depending on the particle size since each formulation has a different nM / OD550 loading capacity. Thus, the fluorescence detection limit of the spectrophotometer should be used to predict the amount of particles needed to adapt this method for other particle sizes.

64. Remove the lyophilized particles from Step 63 onto a disposable weigh-boat.

65. Use a razor blade to cut a small fraction of the particle for OD550 measurement. Target a concentration of 20 OD550 in 100 µL and readjust later after OD550 quantification is made.

Critical Step: 20 OD550 in 100 µL was chosen to ensure that the particle signal will be above the signal detection limit for our spectrophotometer. Additionally, if users are not careful during pipetting steps there could be substantial particle loss, which is mitigated by increasing the initial particle quantity.

66. Resuspend particle sample in 500 µL of water for 5 minutes.

67. Centrifuge the particles at 6000 *g* for 5 minutes.

Critical Step: Since the particles were lyophilized in a non-volatile buffer, the buffer salts are still contained in the pellet. Water should be used to resuspend to prevent high concentrations of buffer salts.

68. Remove the supernatant and wash with 500 µL of TE-Tween.

69. Repeat spinning and washing one more time with the final resuspension in 100 µL of TE-Tween.

70. Make a sample dilution in a separate tube.

71. Measure the diluted sample OD550. Use the OD550 to calculate the stock tube concentration.

Critical Step: If there is less than 20 OD550 in 100 µL, repeat Steps 64-67 to resuspend a newly cut portion of the particle as describe previously and add to the existing particle volume after sufficient wash steps described in this step. Repeat Steps 70-71.

72. Calculate the hybridization component volumes according to **Table 3.4**, assuming a particle concentration target of 20 OD550 in 100 µL total hybridization volume.

Critical Step: The total loading capacity of compDNA of high scaffold density 2 µm particles approaches 75-150 nM of compDNA per OD550 depending on batch-to-batch variation[20]. For the 1:1 R:G particle here, both compR and compG DNAs will maximally load between 37.5-75 nM/OD550, respectively. CompDNA should be loaded at 3x maximal theoretical loading capacity (~225 nM/OD550 for each compDNA on the 1:1 particle) to ensure surface saturation regardless of particle batch variability.

Critical Step: 200 nm particle loading approaches 1000-2000 nM of compDNA per OD550

whereas the 8 µm particle loading approaches 10-20 nM of compDNA per OD550, depending

on the batch variation. The loading capacity should be determined for different particle sizes

prior to experimental use. This should be adjusted in **Table 3.4** for calculating hybridization

reaction conditions depending on the particle size used.

Critical Step: The hybridization buffer will constitute half of the total volume. The remaining half

will be used for particle volume and compDNA. If 100 µL has not been reached, calculate the

volume for TE-Tween to fill the remainder. The total hybridization volume may exceed the target

volume depending on the concentration of reagents, so extra TE-Tween may not be required

(seen as a negative or zero value for the extra TE-Tween calculation).

73. Transfer a quantity of particles into a microcentrifuge tube such that, once diluted, it will
    result in 20 OD550 in 100 µL (hybridization tube). If the volume of particles needed in Step
    72 exceeds 50 µL then centrifuge particles and remove supernatant until 50 µL of volume
    remains.

74. To the hybridization tube, add 50 µL 2x hybridization buffer, compDNAs, and extra TE-
    Tween (if needed).

75. Mix the solution using a micropipette followed by bath sonication for 15 seconds to ensure
    particle dispersion.

76. Incubate particles on a shaker for 30 minutes at 37°C.

Critical Step: Particle hybridization is achieved in less than 2 minutes, although to ensure

surface saturation we hybridize for 30 minutes. During this time, settling occurs at high particle

concentrations which is more apparent when using larger diameter microparticles. If this is

substantial, vortex the particles halfway through their incubation period.

77. During particle incubation, generate fluorescent-compDNA standard curves in a black-
    walled microwell plate.

A. For each fluorescent compDNA:

    i. Start with a 200 µL of a 2 µM DNA concentration in 9% (vol/vol) DMSO in PBS (PBS-DMSO).

    ii. Remove 100 µL to perform twofold serial dilutions until reaching the limit of detection for the plate spectrophotometer, leaving 100 µL per well.

    iii. Separately, make blank-wells containing 100 µL PBS-DMSO for background subtraction.

    iv. Cover the well-plate top and set-aside to protect from light.

Critical Step: Particles will be loaded onto the plate in PBS-DMSO, so the ladder should be made in the same buffer.

78. After hybridization, add 400 µL of TE-Tween and centrifuge at 6000 *g* for 5 minutes at 4°C.

79. Remove supernatant and wash twice more.

80. Use 120 µL TE-Tween for the final resuspension.

Critical Step: After particles have been hybridized, all centrifugation steps should occur at 4°C to minimize dehybridization of loaded cargos.

Critical Step: It is important to remove a majority of the supernatant to prevent background signal. It is additionally important to not disturb the pellet during any steps, as this will reduce the total signal detected during later steps.

81. Add 50 µL of hybridized particles (particle replicate tubes) into two separate centrifuge tubes—these will be used for repeated measures.

82. With the remaining 20 µL volume, dilute a small volume for OD550 calculation to determine the concentration in the particle replicate tubes. This value will be needed to calculate the final DNA nM/OD550.

83. Centrifuge replicate particle tubes at 6000 *g* for 5 minutes and remove 45 µL of supernatant from each.

84. Add 45 µL of DMSO to each particle tube to dissolve particles.

Critical Step: 5 µL of wash buffer should be remaining after supernatant removal to reduce particle loss. If previous wash steps were not thorough, the 5 µL of remaining supernatant could include background DNA signal. The 45 µL of removed supernatant can be saved and measured to determine the background fluorescence contribution.

85. For replicate measurements, add 90 µL of PBS into the microwell plate from Step 77 and 10 µL of dissolved particles.

86. Resuspend all wells thoroughly and do not generate bubbles.

87. Read fluorescence of the microplate on a microplate spectrophotometer in top-down mode with settings in accordance with the respective fluorophores used.

Critical Step: Filters should be carefully selected to minimize signal crossover between fluorophores. Other settings, such as channel voltage, should be optimized for each machine.

88. For fluorescence analysis, average the blank PBS-DMSO wells and subtract from all wells. Create a linear best-fit curve for the fluorescent ladder lanes.

Critical Step: Since the ladder fluorescent signal could be widely different than the measured particle signal, ensure that the ladder range used for generating the best-fit curve are within one-to-two dilution steps away from the measured particle signal to increase accuracy.

89. Calculate the fluorophore concentration of each well using the best-fit curve above. Correct for sample dilution by dividing each well fluorescence concentration by 1/10 of the OD550 value determined in Step 82 to determine stock nM/OD550.

Critical Step: Particles were diluted tenfold in Step 85. This factor needs to be corrected for the

OD550 in the plate.

90. Average the nM/OD550 values from each well and report as the mean ± s.e.m. Calculate

the surface-ratio between R:G signals using the equation below. The ratio of compDNAs is

reflective of the ratio of the scaffold DNAs:

- Ratio of R-nM/OD550 (R) to G-nM/OD550 (G)

    ○ If R > G then the ratio of R to G is (R / G):1

    ○ If R < G, then the ratio of R to G is 1:(G / R)

*See Troubleshooting (**Table 3.5**)*

E.4. Particle size quantification (Timing 2h):

Critical: Microparticle size distributions are assessed using confocal microscopy imaging (Option

A). While brightfield requires less material preparation, confocal imaging of fluorescent particles

produces defined silhouettes and reduces off-target quantification of debris, thus confocal

imaging is recommended for accurate size quantification. The selected magnification should be

used to provide a sufficient field-of-view to capture a large number of particles while still

maintaining visualization of small diameter particles. Since nanoparticle fabrication may be of

interest, we suggest the use of dynamic light scattering (DLS) instruments such as Zetasizer

(Option B). Since Zetasizer does not rely on fluorescence measurements, unlike the confocal

microscopy method, nanoparticles do not need to be hybridized with fluorescent compDNA and

can be analyzed immediately after Step 56.

Option A (microparticle size quantification using confocal microscopy):

91. Particles must first be hybridized using saturating levels of fluorescent compDNA as

described in Steps 72-76 and 78-80. A small amount of particles are needed for imaging (~5-

10 OD550 in 30 μL) so adjust starting particle amount to minimize particle waste.

92. Pipette 10 µL of diluted, fluorescent particle (target ~5-10 OD550) onto a clear microscope slide and overlay a coverslip.

93. Seal the coverslip corners with clear nail-polish.

94. After the corners have partially dried and flattened, seal the sides of the slips by connecting each corner with nail-polish. This will prevent sample drying and allow for slide-inversion on the microscope if needed.

95. Visualize particles under confocal microscopy (**Fig. 3.2g**).

96. Adjust laser power and exposure settings for the relevant laser-line, careful to avoid photobleaching. Height-focus should be set using the fluorescence channel.

97. Acquire at least five representative images.

98. Analyze images using ImageJ to determine particle diameters. Size distribution curves can be generated in software such as Graphpad (**Fig. 3.2h**).

Option B (nanoparticle size quantification using Zetasizer):

99. Prepare a 1 mL dilution of nanoparticles using 0.1 µm filtered deionized water, targeting 0.01 OD550.

100. Dispense an appropriate volume into a disposable cuvette and perform size-analysis using the Zetasizer and the manufacturer's instructions. Intensity-weighted size distributions and other variation metrics, such as the average diameter or polydispersity index (PDI), can be exported and visualized within software such as Graphpad (**Fig. 3.2h**).

*See Troubleshooting (**Table 3.5**)*

E.5. Antibody conjugation with complementary DNA (Timing 1d):

Critical: This procedure describes the conjugation of antibodies with amine-labeled compDNA using an NHS-PEG-Mal linker at a 2 mg antibody scale. This protocol does not change whether

the DNA is labeled, but for most applications we recommend a dyeless-DNA. If a dye-labeled

DNA is used, special attention should be placed to the charge of the dye; we have found that

positively charged dyes may have increased association with the antibody and thus leads to

purification difficulties. Ab-DNA can be labeled for quantification purposes after purification if

required (see "Preparation of antibodies for surface loading quantification").

101. Calculate the volume needed for 2 mg of antibody and prepare a Glen size-exclusion
column that is appropriately sized for the antibody volume per the manufacturer's
instructions. Buffer exchange washes should be 10 mM EDTA in 1x PBS, Ca^{2+}/Mg^{2+} free
(PBS-EDTA).

Critical Step: Ensure that the buffer does not contain any amine-groups (e.g., Tris) as this will

compete to react with NHS reagent used later.

102. Buffer exchange the antibody into PBS-EDTA per Glen column manufacturer's instructions;
collect into a new tube (reaction tube).

103. Measure the antibody A280 using Nanodrop with an appropriate dilution. Place the
antibody at 4°C. Protein concentration can be calculated using the following equations:

- (A280 * Dilution) / 1.33 = (mg/mL antibody)

- ((mg/mL antibody) * 1000) / 155 = nmol antibody, where 155 is the antibody molecular
weight (kDa).

104. Calculate volume of amine-compDNA needed for 4x molar excess relative to antibody in
Step 103. Move this volume into a new tube (DNA reaction tube). The following equation can
be used:

- nmol DNA needed = 4 * (nmol antibody)

- mL of DNA needed = (nmol DNA needed) / (µM DNA stock)

Critical Step: Here, a sub-saturating amount of DNA—as determined using SDS-PAGE

immediately after DNA conjugation without purification—was used to prioritize Ab-DNA purity over conjugation efficiency (**Fig. 3.3b,c**). Higher amounts of DNA could be used to improve Ab-DNA yield as long as the removal of unreacted DNA is confirmed. Importantly, the ratio of DNA-to-biomolecule should be optimized for every new biomolecule and linker.

105. Calculate the mg of NHS-PEG-Mal for 20x molar excess relative to DNA from Step 104. Dissolve linker in a small volume of DMSO, with at least 30 µL per 0.8 mg of linker.

106. Add 20x molar-excess dissolved-linker to the DNA tube and incubate for 1 hour at 37°C. If the reaction DMSO volume exceeds 5% (vol/vol), add HEPES (100mM, pH 7.2) until 5% DMSO is reached.

107. When the DNA-PEG-Mal reaction from the previous step is nearly complete, dilute TCEP to 5 mM in PBS-EDTA.

108. Calculate the volume of 5 mM TCEP needed for 4.5x molar excess relative to antibody amount determined in Step 103.

109. Add this TCEP volume into the antibody tube and incubate for 1 hour at 37°C.

110. Afterwards place the antibody at 4°C.

Critical Step: A lower molar excess can be used but may require longer incubation; longer timing or increased molar excess can result in different reduction cleavage products.

111. Precipitate the DNA as described in Step 5. During the precipitation, a second Glen column should be equilibrated to PBS-EDTA. The final volume after DNA precipitation will be 200 µL, so prepare an appropriately sized Glen column.

112. After 30 minutes at -20°C, centrifuge the DNA reaction tube at 18000 *g* for 10 minutes at 4°C.

113. Remove the supernatant and resuspend in 200 µL PBS-EDTA.

114. Use the Glen column to buffer exchange to PBS-EDTA to remove any excess unreacted

linker from the DNA-PEG-Mal.

115. Determine the DNA-PEG-Mal concentration from the Nanodrop A_{260} and Beer's Law. Reference **Table 3.1** for the relevant extinction coefficients.

116. Add 4x molar excess of DNA-PEG-Mal into the antibody tube and incubate for 1 hour at 37°C. Afterwards, place the antibody reaction tube at 4°C overnight.

E.6. Antibody-DNA purification (Timing 1 to 2d):

Critical: The following steps are required for removal of free, unreacted DNA-PEG-Mal from the Ab-DNA conjugate which can compete for surface hybridization.

117. Use a ring-stand clamp to suspend a resin gravity column over a liquid waste container Assemble the column by placing the column filter at the bottom end nearest the exit port and capping the bottom. Vortex a bottle of Protein G resin beads and add 1.5 mL of the bead suspension followed by a sufficient volume of 1x Protein G binding buffer (binding buffer, diluted in water) to fill the column.

Critical Step: 1.5 mL of suspension results in ~0.75 mL column volume (CV) of resin after liquid drainage. Varied resin amounts can be used depending on the amount of protein being purified.

118. Remove the column cap and allow for the buffer to drain. When ~3/4 of the column height remains, cap the bottom, and wait 20 minutes for the resin to settle.

119. Place a second column filter into the column and push until above the binding resin. Critical Step: Do not trap bubbles beneath the filters as this can slow the elution of the column.

120. Add 5 CVs (~3.75 mL) of binding buffer and allow to drain.

121. Remove the waste container under the column and replace with a 15 mL capture conical tube.

122. Remove the capture tube and replace with another 15 mL conical tube.

123. Add the Ab-DNA from the first capture tube.

124. Repeat twice more by loading the flow-through to ensure maximum column binding.

125. Discard the last flow-through.

126. Place a waste container underneath the filter column and wash with 10 CVs of binding buffer.

127. While the column is washing, label ~thirteen 1.5 mL tubes—five for the acidic elutions, three for the neutral, and five for the basic.

128. Add 55 µL of 10x acidic elution neutralization buffer into each acidic elution tube and 55 µL 10x of basic elution neutralization buffer into each basic elution tube.

Critical Step: If different elution volumes are captured per tube, the volume of neutralization buffer should be adjusted to achieve a final 1x concentration.

129. Add 3 CV (2.5 mL) of acidic elution buffer into the column and begin capturing 500 µL of flow-through into each acidic capture tube.

130. Mix each tube afterwards to ensure the neutralization buffer has mixed into the flow-through.

131. After all acidic buffer has passed, add 3 CV of binding buffer and capture a third of the volume into each of the neutral tubes.

132. After all binding buffer has eluted, add 3 CV of basic elution buffer and capture 500 µL of flow-through into each basic capture tube.

133. Mix each tube afterwards to ensure the neutralization buffer has mixed into the flow-through.

134. Place a waste container underneath the column and add 5-10 CV of binding buffer.

135. After draining, cap the bottom and add binding buffer to cover just above the top resin.

136. Label and store at 4°C if subsequent purifications are needed.

137. Quantify the A260 and A280 of each elution tube using Nanodrop (**Fig. 3.3d**).

138. Dispose all tubes where the A280 indicates minimal protein recovery (<5-10% of the

original theoretical protein amount) and also dispose when the A280 / A260 ratio is less than

0.9.

Critical Step: This step is the most critical for improving the purity of the final Ab-DNA. The A280 / A260 ratio can slightly vary although the tubes which primarily contain the unbound DNAs should have a ratio much less than 1.0.

139. Dialyze the Ab-DNA with 1x PBS using a 50 mL dialysis column (10K MWCO) and place

onto an orbital shaker at 4°C as per the manufacturer's instructions.

140. Swap the 1x PBS after 2 hours and 4 hours cumulative time.

141. After the final swap, dialyze overnight.

142. The next day, collect the Ab-DNA from the dialysis column and store at 4°C.

Critical Step: This step removes the glycine and other buffer components which may inhibit downstream quantifications and purifications. The glycine must be removed if additional Fc-affinity column purifications are needed, otherwise the antibody cannot bind to the resin.

143. Use a microBCA kit to determine the protein concentration (in mg/mL) within the Ab-DNA

conjugate according to the manufacturer's recommendations.

144. The DNA concentration within the Ab-DNA is required for hybridization calculations, but this

requires additional steps to calculate since both the antibody and the DNA independently

contribute to both A260 and A280. Refer to **Box 3.2** to solve for the DNA concentration

within the Ab-DNA.

Critical Step: If a dye-labeled Ab-DNA was used, then the A260 (DNA component of Ab-DNA) can be estimated on a plate spectrophotometer using a standard fluorescent curve of known compDNA-dye concentrations and comparing the fluorescence of a known dilution of Ab- DNA.

145. Use Urea-PAGE to confirm that free DNA has been removed from the Ab-DNA conjugate (**Fig. 3.3e**).

146. Prepare dilutions of Ab-DNA and pure-DNA, run the gel, and analyze according to Steps 19-32.

Critical Step: If a dye-less DNA was used for conjugation, Urea-PAGE must be performed to later stain the DNA with Sybr Gold which is not compatible with SDS-PAGE gels. If a dye-labeled DNA was used, then SDS-PAGE gel is recommended as the antibody bands are more clearly defined.

*See Troubleshooting (**Table 3.5**)*

147. Calculate the Ab-DNA purity with the equation below. If the sample is not pure (e.g., purity <0.95), then the purification Steps 120-145—using the column saved from Step 136—must be repeated before proceeding:

   • Ab-DNA Purity = (Intensity of Ab-DNA band) / ((Intensity of Ab-DNA band) + (Intensity of DNA band))

148. Prepare a sufficiently sized Glen column using 0.1 M triethylammonium acetate buffer (TEAA, pH 7.0) as the exchange buffer.

149. Buffer exchange the Ab-DNA into the TEAA and aliquot into separate tubes for lyophilization.

150. Label the estimated protein and DNA amount in each tube to calculate the new concentrations when later resuspending.

Critical Step: TEAA is a volatile buffer and thus does not leave salts after lyophilization, which could damage the proteins at high concentrations.

151. Freeze the Ab-DNA using liquid nitrogen as described in Steps 61-63 and lyophilize overnight.

152. The next day, resuspend an Ab-DNA aliquot in 0.1 µm-filtered PBS so that the

    concentration of the antibody is at least 6.5 µM, using the concentrations determined in

    Steps 143-144 to determine the new concentrations after resuspension. Store remaining

    aliquots at -20°C.

Critical Step: Higher resuspension concentrations (>1 mg/mL) are important for the stability of

proteins and to have more reasonable volumes to work with during particle hybridization. To

note, resuspending the Ab-DNA at too high concentrations could result in protein

aggregation[71,72]. Thus, concentrations between 1-10 mg/mL are recommended which is

comparable to the concentrations of the purchased antibody stocks used within this protocol.

Pause Point: Lyophilized proteins are stable at -20°C for over 2 years. Antibody can remain

stable at 4°C for over a year. The shelf-life of other proteins should be assessed and monitored.

153. (Optional): Sodium azide (0.05%) can be added to a desired concentration to limit

    microbial growth once resuspended and stored at 4°C.

        E.7. Preparation of antibodies for surface loading quantification (Timing 2h):

Critical: Flow cytometry can be immediately used to verify the ratio between protein species on

particle surfaces if the conjugated compDNA was labeled with a fluorescent dye. If unlabeled

compDNA was used for conjugation, NHS-dye labeling of the antibody is first required. Below

we describe the labeling of αCD28-compR. The procedure is identical for labeling αCD3-compG

but with a different fluorophore. To reduce non-specific interactions between the Ab-DNA and

the particle, we recommend using negatively charged dyes for Ab-DNA labeling.

154. For later quantification, record the A260 and A280 of the Ab-DNA. Calculate the ratios R1

    = A280 / (µM antibody) and R2 = A260 / (µM DNA), where the respective antibody and DNA

    concentrations are known from Step 152 after resuspension from lyophilized stock.

155. Resuspend NHS-Alexafluor-488 (AF488) to 2 mM in DMSO.

156. Aliquot ~50 ug (0.32 nmol) of purified αCD28-compR (~100 μL at 0.5 mg/mL).

157. Add 8x molar excess of 2 mM AF488 into the antibody aliquot and react for 1 hour at 37°C.

158. Record the final reaction volume.

Critical Step: Do not exceed 5% (vol/vol) DMSO to reduce protein denaturing. To prevent this, either make a more concentrated stock of NHS-dye or dilute with HEPES (100 mM, pH 7.2).

159. Prepare an appropriately sized Zeba spin desalting column according to the manufacturer's instructions, replacing the buffer with 1x TE. Load the αCD28-compR- AF488 onto the column and spin as recommended.

160. Measure the A260, A280, and A488 to solve for the antibody, DNA, and AF488 concentrations using the below equations:

- μM antibody = A280 / R1, where R1 is from Step 154. Similarly, μM DNA = A260 / R2, where R2 is from Step 154.

- AF488 μM = A488 / (Extinction coefficient AF488).

- Number of AF488-dye per antibody = (μM AF488) / (μM antibody)

Critical Step: Depending fluorophore intensity and dilution, the absorbance may be greater than 1.0. If so, redo this step using a higher dilution. The number of AF488-dyes per antibody should be above 1.0 and can be used to indicate successful conjugation.

E.8. Particle surface loading of antibody (Timing 2h):

Critical: The following describes the loading and quantification of αCD28-compR-AF488 and αCD3-compG-AF647 DNA-conjugates onto microparticles presenting a 1:1 R:G DNA scaffold. These steps assume NHS-dye labeled antibodies were prepared previously, although the procedure is identical for any fluorescently tagged antibody (e.g., using dye-labeled DNA during

Ab-DNA synthesis). If this procedure is performed under sterile conditions and using sterile materials, these particles are applicable for use in vitro and in vivo settings (see Critical Step following Step 169).

161. Assuming particles are lyophilized in -20°C storage, prepare a small quantity of particles to allow for 1 OD550 in a final volume of 100 μL TE-Tween by following Steps 64-69 (adjusting for the desired OD550).

162. Assuming that antibodies have been prepared and labeled using NHS-dye, calculate the necessary volume of αCD28-compR-AF488 and αCD3-compG-AF647 to reach a final concentration of 30 nM each in 100 μL (total hybridization volume).

Critical Step: The antibody loading capacity on 1.5 μm particles is approximately 20 nM/OD550 which was previously determined using plate spectrophotometry as described in "Particle surface DNA loading analysis"[20]. The maximum loading capacity of other biomolecules should be determined for every new biomolecule type and particle size to ensure an appropriate excess is given during surface hybridization. Given that the scaffold ratio is 1:1, each antibody will maximally load ~10 nM/OD550. Since loading is at 3x excess of the theoretical limit, each antibody is hybridized at 30 nM/OD550 for a combined antibody concentration of 60 nM/OD550.

Critical Step: Particle loading should occur between 1-10 OD550. The total reaction volume is flexible, although the total reagent use should be considered. If done under sterile conditions, particles can be used for biological applications using a small sample for flow analysis.

163. Refer to **Table 3.4** for calculating the hybridization volumes, adjusting for the target OD550, antibody loading capacities, and antibody concentrations.

164. Spin the 100 μL of 1 OD550 particles for 5 minutes at 6000 *g* and remove supernatant until the calculated particle volume needed from Step 163 is reached.

165. To a 1.5 mL tube, add 50 μL of 2x hybridization buffer, the Ab-DNAs, and extra TE- Tween

using the values in Step 163.

166. Resuspend the particles and add into this reaction tube.

167. Use the micropipette to mix and sonicate briefly (~5-10 seconds). Incubate for 30 minutes at 37°C.

168. Wash particles twice according to Step 78-79 at 4°C.

169. After the last wash, resuspend in 500 μL TE-Tween.

Critical Step: For adapting to sterile use, particles should be resuspended using sterile PBS rather than TE-Tween. Additional PBS washes could be used to ensure the removal of Tween-20 detergent or other hybridization components. However, particle loss may increase without the use of a detergent, thus OD550 should be verified prior to particle dosing. While in vitro use is described later, particles for in vivo use should be concentrated using centrifugation to a desired volume suitable for localized or systemic injections as previously demonstrated[20].

E.9. Quantification of antibody loading onto particles using flow cytometry (Timing 4 to 6h):

Critical: This procedure quantifies the microparticle surface loading of αCD28-compR-AF488 and αCD3-compG-AF647 using flow cytometry. Blank and single-antibody loaded particles are made using the method described in Steps 163-169 and are used for compensation controls and downstream calculations. Use single DNA-sequence scaffolded particles (R or G only) for single-color controls to saturate the surface with their respective antibody species. The plate spectrophotometer used in the previous section "Particle surface DNA loading analysis" can be used as an alternative quantification tool, although this uses prohibitively more material due compared to flow cytometry.

170. Perform flow cytometric analysis on particles from Step 169. Reference **Box 3.3** for performing surface-loading analysis using software such as FlowJo. We have included

representative flow cytometry fluorescence histograms and calculated surface loadings for

particles hybridized using a variety of loading methods as described in the section

"Experimental Design" (**Fig. 3.4**). Example data from Steps 161-169 that used the 1:1 R:G

surface-scaffold and particle surface-saturating amount of Ab-DNA is provided (**Fig. 3.4h**)

*See Troubleshooting (**Table 3.5**)*

E.10. T cell enrichment from leukapheresis products (Timing 2hr):

Critical: This procedure describes the isolation of either CD4$^+$ or CD8$^+$ T cells from leukapheresis

blood product using commercial negative selection beads.

171. In a sterilized BSC, isolate CD4$^+$ or CD8$^+$ T cells from leukapheresis blood using the

EasySep Enrichment Kit per the manufacturer's instructions. Wash steps should be

performed using sterile-filtered PBS-FBS wash buffer (see "Reagent Setup"). When

required, cells should be centrifuged at 300 *g* for 5 minutes at 4°C.

172. After cells have been enriched, spin down the cells at 300 *g* for 5 minutes at 4°C. Calculate

the volume to resuspend cells between 10-50 x 10^6 cells/mL. Remove the supernatant and

resuspend in sterile freezing medium to the desired concentration. Aliquot 1 mL of cells into

each liquid nitrogen compatible freezing vial and place into a polyethylene CoolCell.

Immediately transfer the CoolCell into the -80°C freezer overnight. Transfer freezing vials to

liquid nitrogen storage the following day.

Pause point: T cells can be stored in liquid nitrogen for over a year and thawed when needed.

E.11. T cell expansion using ICEp (Timing ~11d):

Critical: This procedure describes CD4$^+$ T cell culturing using ICEps which is identical for CD8$^+$ T

cells. Cells will be expanded in a 96-well (flat-bottom) culture plate throughout, although they

can be transferred to larger well-plate volumes as long as the appropriate cell concentrations are maintained. ICEps should be prepared sterilely with αCD3 and αCD28 one day before T cell activation as described in the previous section, "Particle surface loading of antibody". The quantity of particles required should be determined before T cell activation to reduce material waste. Complete T cell media (media) should contain 100 U/mL hIL2.

173. Centrifuge αCD3 and αCD28 loaded ICEps at 6000 g for 5 minutes at 4°C.

174. In a BSC, carefully remove supernatant and resuspend to 1 OD550 (~20E6 particles/mL) in media. OD550 can be measured to verify desired particle concentration.

Critical Step: We will seed 25,000 T cells per 96-well, so 1.25 µL of particles (at 1 OD550) will eventually be added to each well for 1x particle to cell excess. Additional particle amounts can be added, although the total well volume should stay consistent between conditions.

175. Warm media in a 37°C water bath.

176. Aliquot 9 mL of warmed media into a 15 mL tube.

177. Remove a CD4$^+$ enriched T cell vial from liquid nitrogen storage and thaw in the water bath. Just prior to fully thawing, move the vial into the BSC.

178. Gently pipette to resuspend the cell pellet and transfer the volume into the 9 mL of warmed media to dilute the DMSO.

179. Spin cells at 300 g for 5minutes at 4°C.

180. Remove the supernatant and resuspend cells in 10 mL of media and count the cells. Depending on the number of T cell conditions, dilute an appropriate volume of cells in media to ~0.278E6 cells/mL.

181. After mixing, pipette 90 µL of cells per well in a 96-well plate.

182. Thoroughly mix the ICEps without generating bubbles and add an appropriate volume to each well (1.25 µL of 1 OD550 for 1x particle-to-cell). Occasionally resuspend stock ICEps

to prevent particle settling.

183. Add additional media for a total well volume of ~100 µL. The cells are now approximately at 0.25E6 cells/mL.

184. Using a multichannel pipette, gently mix all wells to thoroughly distribute ICEps and cells. Transfer the seeded culture-plate into a sterile incubator set to 37°C and 5% CO_2.

185. After 24 hours (Day 1) visualize the plate under a bright-field microscope to observe cell clustering and look for any signs of contamination.

186. After 48 hours (Day 2), double the well volume using prewarmed media (~100 µL) by dispensing around the well perimeter, attempting not to disturb the cell clusters. Cells are typically not ready to be split at this day due to a freezing-related growth delay.

187. On day 4, resuspend the T cell wells and take a small sample for counting.

188. Calculate the volume containing 25000 cells and reseed this volume into an unused well. Add media for a total well volume of 100 µL.

189. Track the cell expansion fold between well-splitting and repeat every two days until growth slows or a pre-determined end-point has been reached (**Fig. 3.5a,b**).

Critical Step: At this concentration, a two-day splitting procedure lets cells expand upwards of 10-15 fold without filling the entire well. Other plating conditions requires different schedules.

190. At the experiment endpoint, stain, and fix cells for flow cytometry analysis (**Fig. 3.5c-e**).

*See Troubleshooting (**Table 3.5**)*

F. ANTICIPATED RESULTS

F.1. Fabrication of PLGA particles with dense DNA scaffolds

A critical step in determining the particle DNA-scaffold density is the synthesis of polymer- DNA amphiphiles; as the sole surfactant for the emulsion-based fabrication protocol, the surface presentation of the DNA domain is driven by hydrophobic-hydrophilic interactions (**Fig. 3.1-i**)[56,73]. Polymer-DNA amphiphiles are generated from the conjugation of PLGA(10k)-PEG(5k)-Mal (PLGA-PEG-Mal, Akina #AI053) with thiol-DNA-17mer via the Michael addition reaction in DMF/TE (vol/vol, 90:10) solvent, which can then directly used for the emulsion protocol without prior purification (**Fig. 3.1-i and Fig. 3.2a**). We found that the input amount of the PLGA-PEG-Mal determines the particle size in the downstream emulsion protocol, so we maintained a constant 100 nmol of polymer reactant for each fabrication procedure targeting a particle diameter of 2 µm. Thus, the input molar excess of thiol-DNA relative to polymer—which directly correlates with the conjugation efficiency of PLGA-PEG-DNA—determines the DNA-scaffold density on the yielded particle product (**Fig. 3.2b-f**). Notably, we found that there was a conjugation efficiency variation associated with different lots of PLGA-PEG-Mal made by Akina, Inc. (**Fig. 3.2c,e**) and the quality of thiol-DNA (**Fig. 3.2d**), of which the latter became less of an issue when we sourced the thiol-DNA from IDT, Inc. instead of in-house synthesis as previously reported[20]. The 1:1 PLGA-PEG-Mal to thiol-DNA reaction ratio was chosen since the conjugation efficiency for the high-quality PLGA-PEG-Mal lot approached saturation as identified by Urea-PAGE (see PLGA Lot-1 in **Fig. 3.2b,e**). Poor quality PLGA-PEG-Mal may require high amounts of thiol- DNA to reach saturation, which is not economically viable and contributes to a lower DNA- scaffold density (see PLGA Lot-2 in **Fig. 3.2b,e,f**). Here, Urea-PAGE provided an effective and essential tool for the quality control of PLGA-PEG-DNA which should be routinely performed. As mentioned, the input amount of PLGA-PEG-Mal relative to unmodified PLGA during emulsion determines the size profile, therefore, it can be adjusted to

obtain particles with varied intended size (**Table 3.3** and **Fig. 3.2g,h**). This protocol produces approximately 200 nm diameter nanoparticles with a polydispersity index (PDI) range of less than 0.200, as determined by the built-in Zetasizer software, which indicates highly uniform particles (**Fig. 3.2h**, Size A)[74]. Further, these particles maintain similar mean diameters across batches, indicating low batch variance. For micron-scale particles, large size-distributions have been reported using bulk probe- sonication protocols, which was also observed here (**Fig. 3.2h**, Size B and C)[55]. While a given batch may be polydisperse, batch-to-batch variation was minimal, as indicated by the similar diameter and s.d. ranges compared to their averaged value across batches. Therefore, across size- scales this protocol generates DNA-scaffolded particles with minimal batch-to-batch variation.

F.2. Antibody-DNA conjugation and purification

To chemically modify antibodies with minimal activity loss, a selective reduction protocol using a precise molar excess of TCEP (4.5x) is used to generate free thiols for compDNA attachment (**Fig. 3.3a,b**). Therefore, it is important to accurately measure the antibody concentration to determine the TCEP dose. During antibody handling, Ca2+/Mg2+-free PBS buffer supplemented with 10 mM EDTA is used to keep the thiol groups from oxidizing and reforming disulfide linkages75. SDS-PAGE serves as a handy tool to check the extent of antibody reduction and fractionation after Ab-DNA conjugation (**Fig. 3.3b**). Linker-attached compDNA with maleimide functionalization (DNA-PEG-Mal) is given in excess to ensure a high yield of DNA-antibody conjugates. However, the excess amount of unreacted DNA needs to be removed to avoid competition in the downstream surface hybridization step. Hence, we titrated the DNA molar excess to the antibody and found that a range of 4x to 6x is the minimal excess for the highest conjugation efficiency as determined by the saturating trend for the conjugation reaction (**Fig. 3.3c**). Fc affinity-based chromatography was found to be the only method that

effectively removed unreacted DNA. To ensure a high recovery of the costly antibodies and a complete removal of excess DNA, we provide guidelines to determine the appropriate elution fractions to collect from the purification (**Fig. 3.3d**) and to check for residual free-DNA after purification (**Fig. 3.3e**) (see "Antibody-DNA purification").

F.3. Particle surface functionalization and quantification

The ratiometric and density control of one or more functionalities on particle surfaces are achieved through cargo-directed (**Fig. 3.4a-c and d-e**) and scaffold-directed (**Fig. 3.4f-g**) strategies. For the former method, one or multiple functionalities (compDNA-protein cargos) are hybridized onto the surfaces with a total input amount below the predetermined loading capacity of the cargo (**Fig. 3.4a-c and g-h**). The density and relative ratio of different cargos are adjusted by the input mixture ratio prior to surface-hybridization (**Fig. 3.4g-h**). For the latter method, one or multiple functionalities are hybridized onto particles with different densities of DNA scaffolds (with one or more sequences), and the loading input of the cargos are controlled at 3x molar excess to the predetermined loading capacity of each cargo (**Fig. 3.4d-f**). Flow cytometry enables the precise ratiometric quantification of surface-decorated cargos resulting from either method. While the cargo-directed method does not require unique particle scaffold formulations, it can have limitations in precision when cargos with different chemical properties (e.g., size and charge) are co-loaded[20]. Currently, we focus on using this method to characterize the relative densities and ratios of biomolecules, although the absolute numbers could be further quantified by establishing standard titrations in the future.

F.4. Exemplified human T cell activation ex vivo

DNA-scaffolded PLGA microparticles (2 μm) were coated with compDNA-conjugated agonistic antibodies αCD3 and αCD28 at various ratios to provide stimulatory and co-stimulatory signals for human T cell activation and ex vivo expansion, which is a key step for T cell manufacturing[29]. As reported previously, the ratiometric control of αCD3 to αCD28 had an impact on T cell expansion fold (**Fig. 3.5a**), and here we found that the particle to cell excess also affected cell expansion (**Fig. 3.5b**)[20]. Additionally, we expect that the size of the particles and the stability of the polymer may also matter for cell activation, so these chemiophysical parameters—in addition to details of material-cell interactions—would need to be systematically investigated among multiple T cell donors when adopting this type of material for T cell manufacturing[24,76,77]. Other than cell quantity, cell quality that is directly associated with the therapeutic efficacy after infusion into patients should also be evaluated. Here, we exemplified a flow cytometry-based immune profiling to evaluate cell differentiation (memory and effector fates, **Fig. 3.5c,d**) and exhaustion (co-expression of inhibitory receptors, **Fig. 3.5c,e**). While cell phenotyping provides important metrics relating to cell quality, the functionality of manufactured cells should also be evaluated in vivo in related animal models[78].

F.5. Acknowledgements

F.6. Author contributions

P.H. and X.H. designed the experiments and drafted the manuscript. P.H. and L.C. contributed to experiments in **Figures 3.2-5**, Y.C. and Z.H. contributed to experiments in **Figure 3.2**. P.H. analyzed the data. All authors contributed to the editing of the manuscript.

F.7. Key reference using this protocol

*Huang, X. et al. Nat. Nanotechnol. **16**, 214–223 (2021): DOI: 10.1038/s41565-020-00813-z*

G. FIGURES
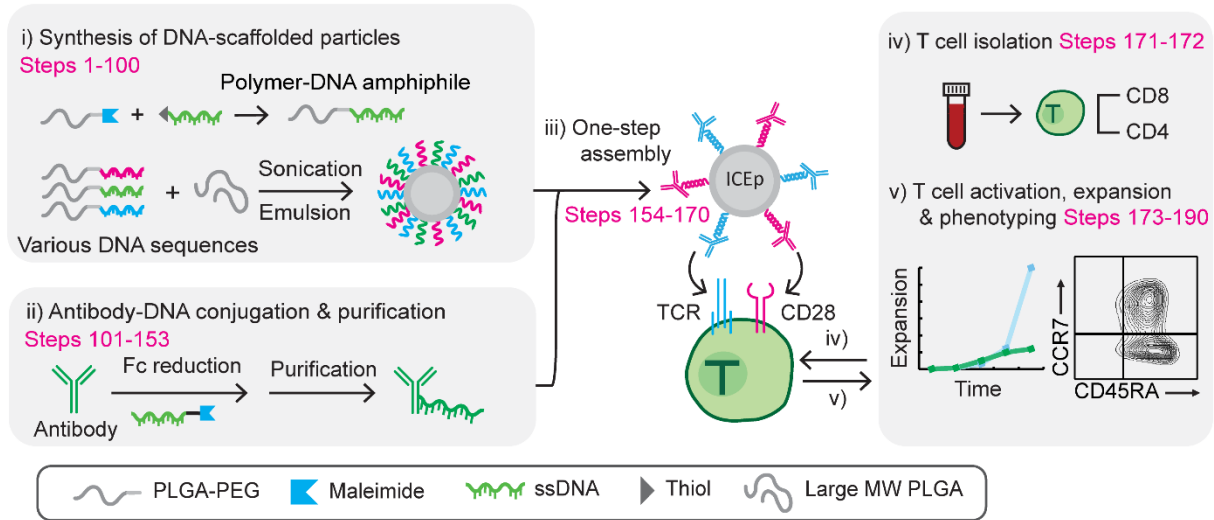
Figure 3.1. Schematic of the fabrication protocol for precision immune cell-engaging particles (ICEp).

The precise functionalization of immunomodulatory signals on synthetic material surfaces is enabled by attaching DNA-handles on both components and associating them via DNA-hybridization. This protocol involves i) synthesizing particles with dense surface DNA scaffolds (with one or multiple sequences) through emulsion-based fabrication using polymer-DNA amphiphiles as surfactants, ii) conjugating the complementary-DNA (compDNA) to the immunomodulatory biomolecules with minimal bioactivity loss and complete removal of free DNA, and iii) loading compDNA-biomolecule conjugates on particle surfaces through one-step hybridization. Here, ICEp are exemplified for their use in human T cell ex vivo expansion, which is highlighted with essential details in iv) T cell isolation and v) cell culture & activation that can impact phenotypic outcome of cell products.
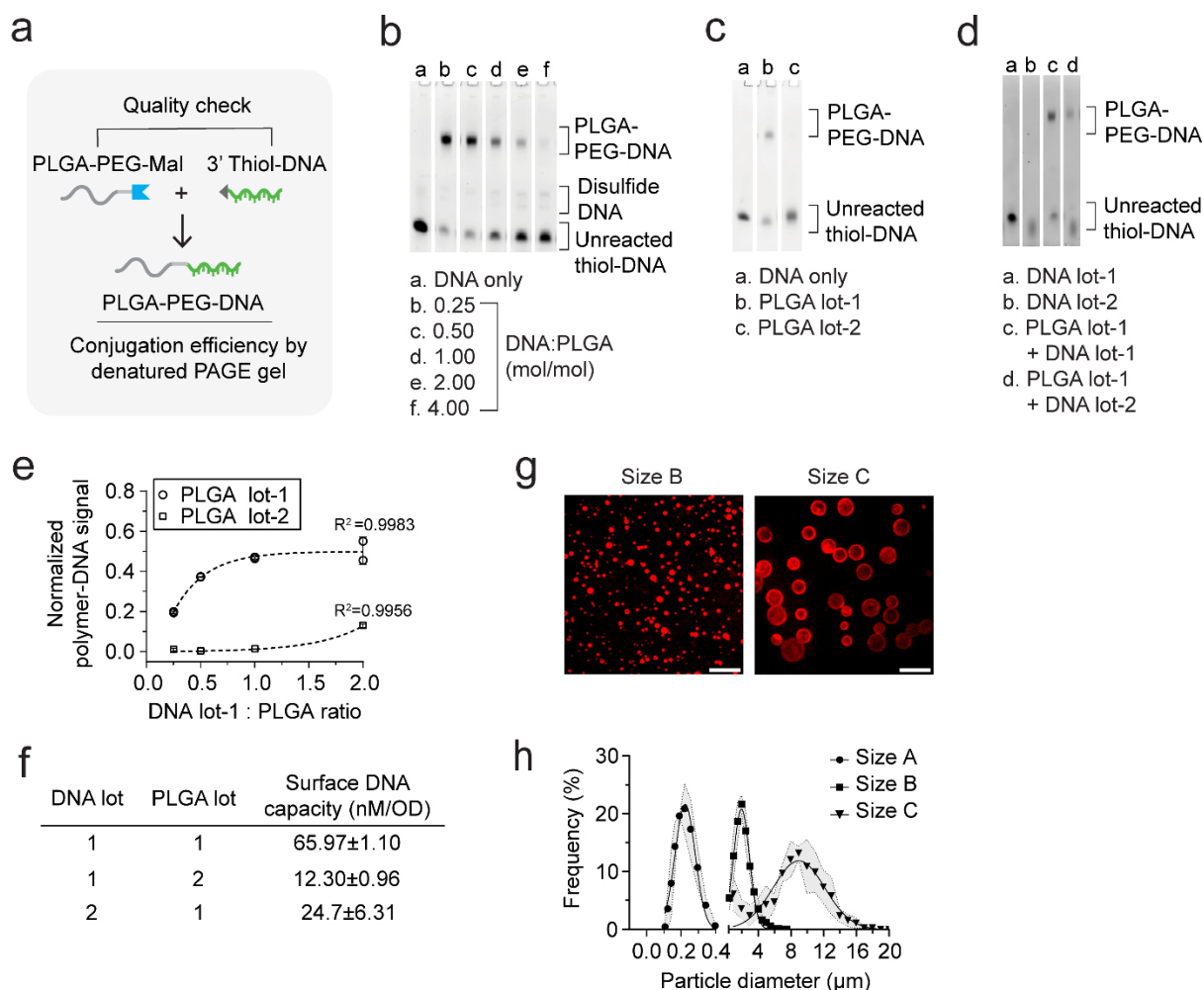
Figure 3.2. Quality control of PLGA particles with dense DNA scaffolds.

(a), Schematic of the synthesis of polymer-DNA amphiphiles and their quality check via gel electrophoresis—an essential step in achieving a high DNA-scaffold density upon particle fabrication. (b-d), Urea-PAGE of PLGA-PEG-DNA conjugates from the synthesis reactions using b varying molar ratios of thiol-DNA to PLGA-PEG-Mal, c different lots of PLGA-PEG-Mal, and d different lots of thiol-DNA. The total DNA input into each lane was controlled at 1 pmol. (e), Normalized PLGA-PEG-DNA amount to the total DNA amount in each lane of gel images in b and c using densitometry analysis in ImageJ. PLGA Lot-1 and Lot-2 were fit using exponential plateau (R^2 = 0.9983, RMSE = 0.0057) and exponential growth (R^2 = 0.9956, RMSE = 0.0041) models, respectively. (f), Surface loading capacity of fluorescently labeled compDNA on microparticles (2 µm diameter) fabricated using PLGA-PEG-Mal from different lots of PLGA-PEG-Mal and thiol-DNA in c and d. Data are mean ± s.e.m of n = 3 technical replicates. (g), Representative confocal microscope images (40x magnification) of particles fabricated using different protocols that yield different sizes and hybridized with Cy3-labeled compDNA.

(Figure caption continued on the next page.)

(Figure caption continued from the previous page.)

Scale bar: 20 µm. (h), Size distribution of particles measured using Zetasizer (Size A: mean diameter = 220.42 nm, mean diameter range = 201.54 – 234.35 nm, PDI range = 0.120 – 0.176, n = 3 independent samples) or shown in g using ImageJ analysis (Size B: mean diameter = 1.90 µm, mean diameter range = 1.74 – 2.10 µm, s.d. average = 1.01 µm, s.d. range = 0.99-1.01, n = 3 independent samples; Size C: mean diameter = 7.78 µm, mean diameter range = 6.57 – 8.61 µm, s.d. average = 3.75 µm, s.d. range = 3.40 – 3.89 µm, n = 4 independent samples). Size frequencies were fit with gaussian distribution curves ([Adjusted R^2, RMSE]: Size A = [0.8323, 3.343], Size B = [0.9462, 1.720], Size C = [0.6897, 2.543]) and the shaded regions represent error envelopes of ±1 s.d. for each discrete frequency bin.
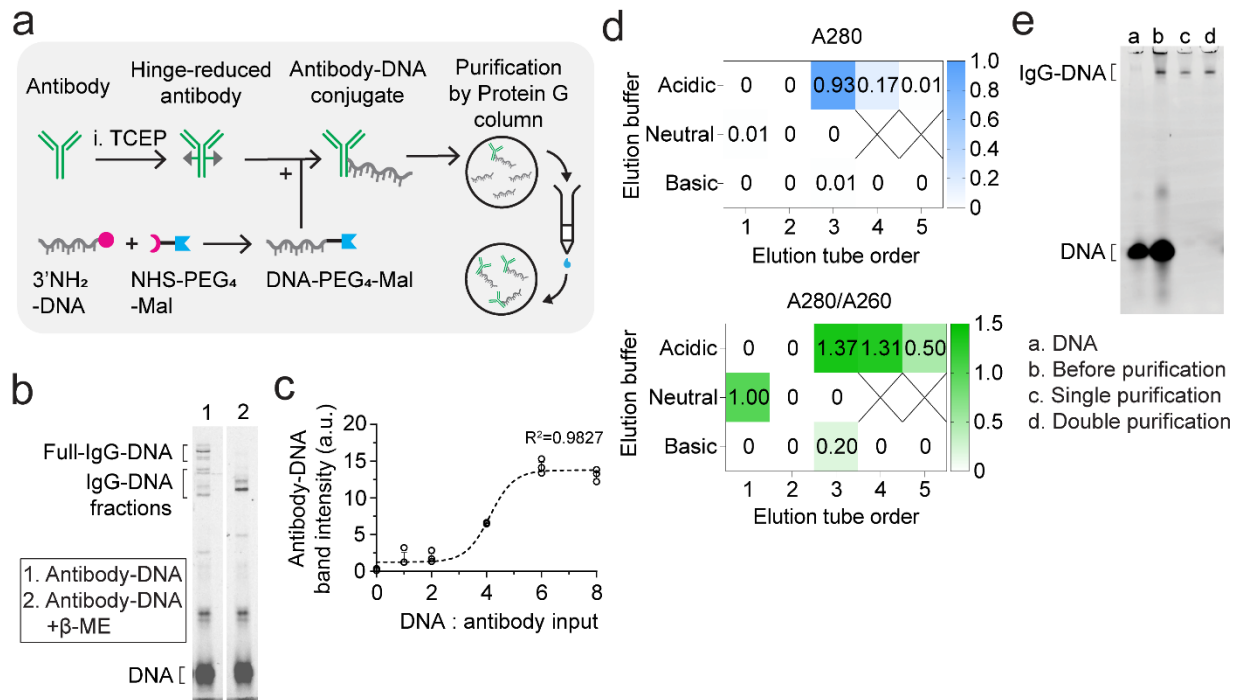
Figure 3.3. Protocol and quality checkpoints of antibody-DNA conjugation and purification.

(a), Schematic of antibody-DNA (Ab-DNA) conjugation through selective reduction of antibody hinge-region disulfides and Fc affinity-based chromatography for purification to remove excess, unreacted DNA. (b), SDS-PAGE of Ab-DNA conjugates from selective reduction by TCEP treatment at 4.5x molar excess (lane 1) versus full-reduction by β-mercaptoethanol (β-ME) treatment (lane 2). (c), Densitometric analysis of Ab-DNA bands from Urea-PAGE of reactions with varying ratios of DNA to antibody input. Data was fit using a sigmoidal dose-response curve (R^2 = 0.9827, RSME = 0.8078). Data represent mean ± s.e.m of n = 3 technical replicates. (d), Example heatmaps depicting the A280 or A280 / A260 ratios of Ab-DNA conjugates eluted from Fc affinity-based chromatography columns. (e), Urea-PAGE of Ab-DNA conjugates with and without purification.
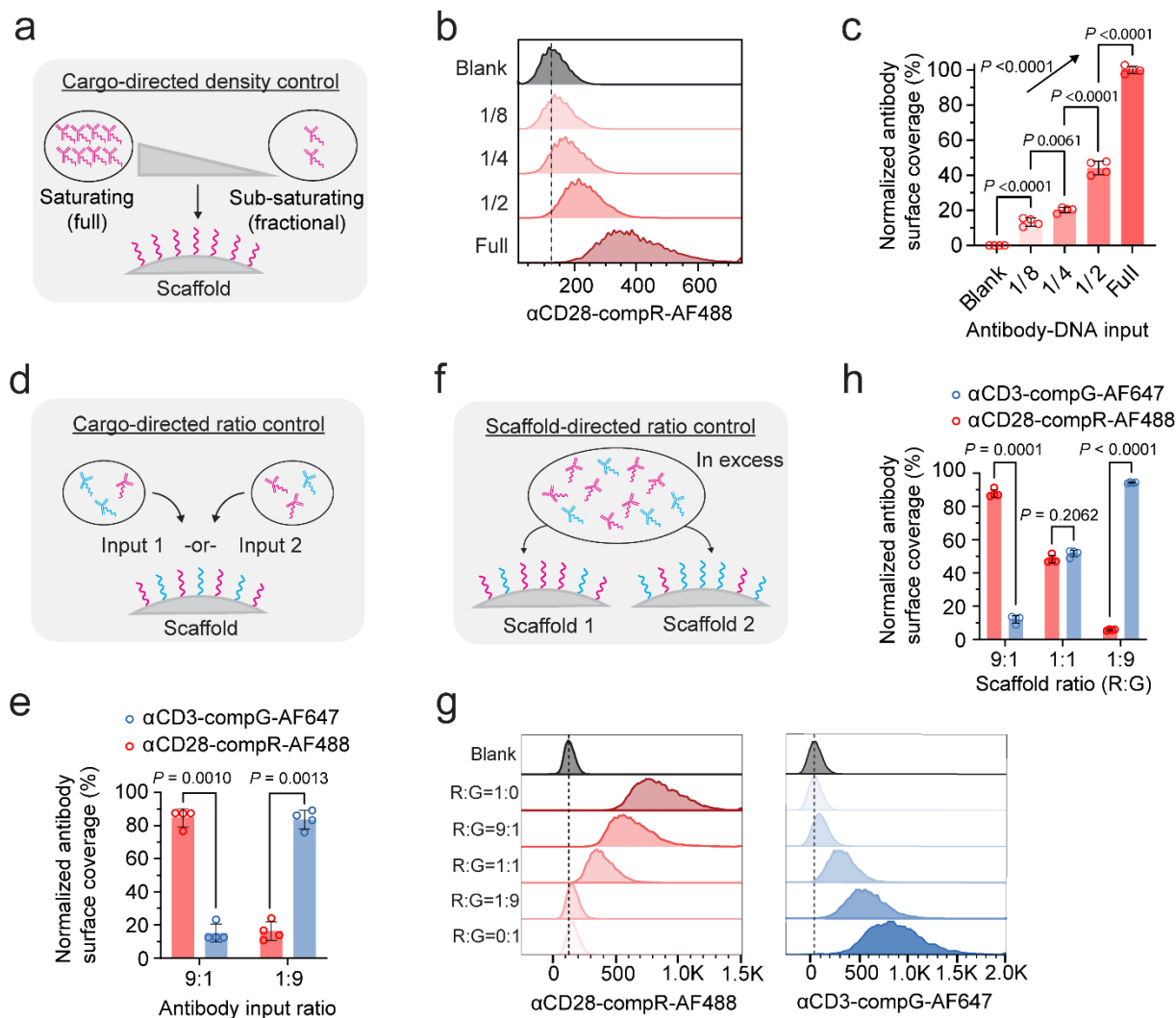
Figure 3.4. Density and ratiometric control of cargos co-loaded onto particle surfaces.

(a), Schematic of titrating the input amount of compDNA-cargo to control the surface density on particles. (b-c), Flow cytometry histograms b and normalized mean fluorescence intensities (MFI) c of particles hybridized with varying input amounts of antibody-DNA (Ab-DNA; αCD28-compR-AF488, Full: 20 nM/OD550, 1/2: 10 nM/OD550, 1/4: 5 nM/OD550, 1/8: 2.5 nM/OD550). Linear trend was determined using one-way ANOVA test ($F_{1,15}$ = 3944, P <0.0001) and inter-Ab-DNA input P values were determined by one-way ANOVA ($F_{4,15}$ = 1151, P < 0.0001) followed by Tukey's *post hoc* test. (d), Schematic of the ratiometric control of surface cargos by the input ratio of Ab-DNA cargos at the hybridization-based assembly step. (e), Flow cytometry-based quantification of particles (R:G = 1:1) that are hybridized with different ratios of Ab-DNA (αCD28-compR-AF488 and αCD3-compG-AF647) with a constant total amount of 20 nM/OD. Data are normalized MFI to the maximal loading capacity from particles with only one sequence of scaffold (R:G = 1:0 or R:G = 0:1). P values were determined by multiple two-tailed paired *t*-tests. (f), Schematic of the ratiometric control of surface cargos by the DNA-scaffold ratio of different sequences.

(Figure caption continued on the next page.)

(Figure caption continued from the previous page.)

(g), Flow cytometry histograms of particles fabricated with varying ratios of DNA scaffolds (R:G = 9:1, R:G = 1:1, R:G = 1:9) and hybridized with equal input amount of cargos (αCD28-compR-AF488 and αCD3-compG-AF647) in excess. (h), Normalized MFI of histograms in e to the maximal loading capacity from particles with only one sequence of scaffold (R:G = 1:0 or R:G = 0:1). *P* values were determined by multiple two-tailed paired *t*- tests. Data c, e, h represent mean ± s.d. of *n* = 4 experimental replicates from two independent experiments.
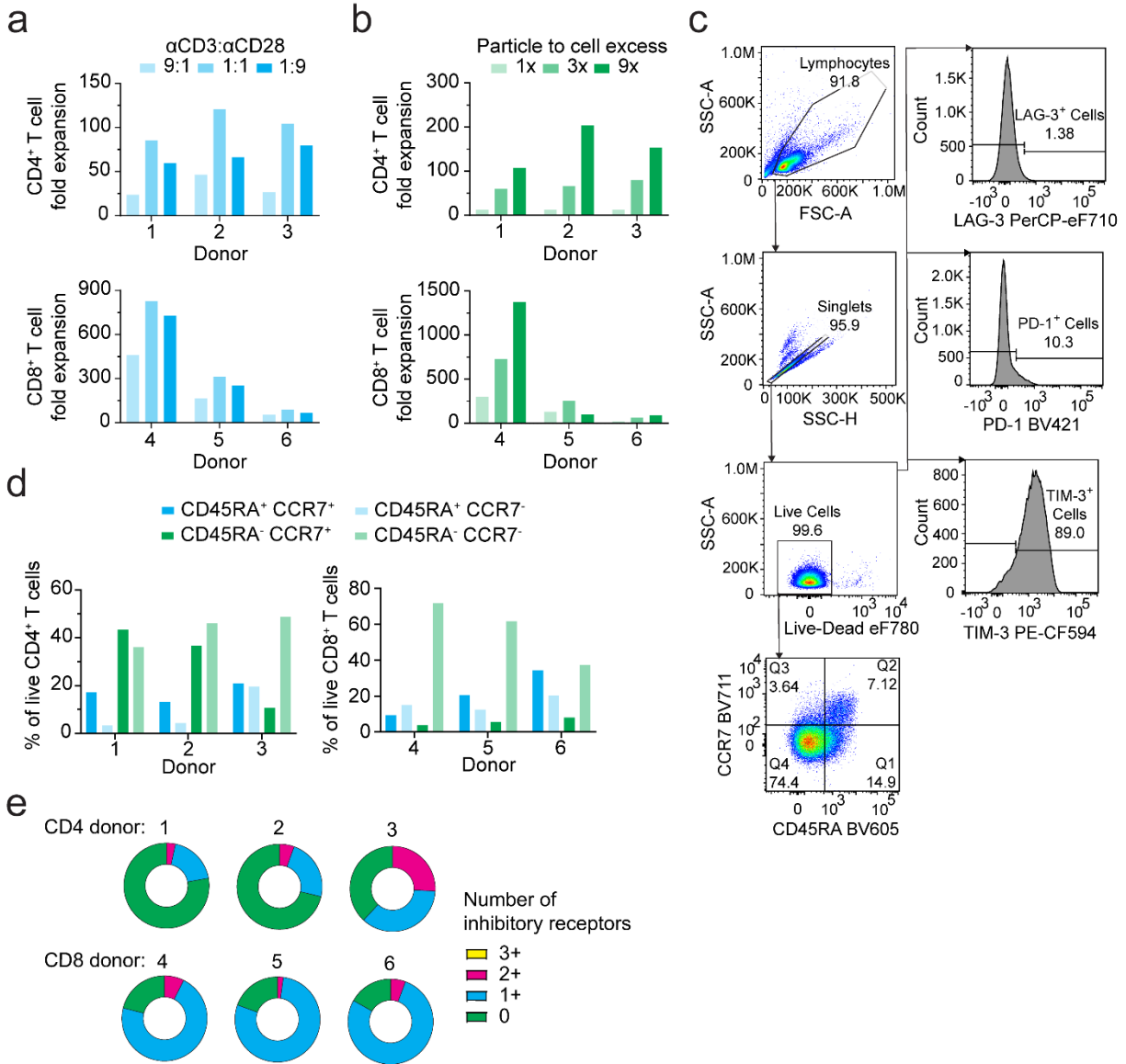
Figure 3.5. ICEp activation of human T cells and their phenotypic characterization

(a), Expansion fold of T cells (CD4+ and CD8+) at day 11 from the activation by ICEp with varying ratios of αCD3 to αCD28 on particle surfaces and 3x excess of particles to cells. (b), Expansion fold of T cells (CD4+ and CD8+) at day 11 from the activation by ICEp (αCD3-compR:αCD28-compG, 1:9) with varying particle to cell excess. (c), Representative flow cytometry gating strategy for T cell phenotyping. (d), Populations of naïve and stem cell-like memory (CD45RA+CCR7+), central memory (CD45RA-CCR7+), and effector memory cells (CD45RA-CCR7- and CD45RA+CCR7-) in expanded cells (CD4+ and CD8+) at day 11. Cells were activated using ICEp (αCD3-compR:αCD28-compG, 1:9) with 3x excess of particles to cells. €, Populations of cells with co-expression of inhibitory receptors (LAG-3, PD-1, and TIM-3) at day 11. Cells were activated using ICEp (αCD3-compR:αCD28-compG, 1:9) with 3x excess of particles to cells. Data a, b, d, e represent *n* = 6 independent donors (*n* = 3 for CD4+ and *n* = 3 for CD8+ T cell experiments).

H. TABLES

Table 3.1. DNA sequences used for polymer and protein bioconjugation

Name	Sequence (5' to 3')	3' Modification	Extinction coefficient ($M^{-1}*cm^{-1}$)
R	AGTGGGAGCGCGTGATG	Thiol (C3 S-S)	173700
G	GTTCATCTGCACCACCG	Thiol (C3 S-S)	148100
B	GCCTTTACGATGTCCTT	Thiol (C3 S-S)	144400
compR[a]	C[*]A[*]T[*]C[*]ACGCGCTCCCACT[*]A[*]A[*]T[*]T[*]	NH2 (Amino C7)	188400
compG[a]	C[*]G[*]G[*]TGGTGCAGATGAACTT[*]C[*]A[*]G[*]	NH2 (Amino C7)	215000
compB[a]	A[*]A[*]G[*]GACATCGTAAAGGCA[*]T[*]T[*]T[*]	NH2 (Amino C7)	216300

[*] = internal phosphorothioate bond.
[a]compDNAs can be optionally labeled with fluorophore at the 5'-end for quantification purposes.

Table 3.2. PLGA-PEG-DNA conjugation reaction template

Predetermined	
a. PLGA-PEG-Mal : DNA Ratio	1
b. Target PLGA-PEG-Mal concentration (µM)	200
c. PLGA-PEG-Mal molecular number (Da):	22941
d. Total DNA (µM)	See Step 8
e. Volume of DNA (µL)	See Step 8
Calculated	
f. Total reaction volume (µL)	(e * d * a) / b
g. Triethylamine volume (µL)	f / 100
h. Extra TE buffer volume (µL)	(f / 10) - e
i. PLGA-PEG-Mal needed (mg)	(a * d * e * c) / (1E9)
j. 30 mg/mL PLGA-PEG-Mal DMF volume (µL)	(1000 * i) / 30
k. Extra DMF volume (µL)	0.9 * f - j - g

Table 3.3. Fabrication conditions for achieving varied particle diameters

Particle diameter (µm)	PLGA- PEG-DNA (nmol)	Unmodified PLGA (Mw 38,000-54,000) (mg)	Vorganic (µL)	Vaqueous (µL)
0.2 (Size A)	200	5	500	1000 (50µL 5% PVA)
2 (Size B)	100	50	500	500 (no PVA)
8 (Size C)	20	50	500	500 (no PVA)

Table 3.4. Particle surface hybridization of complementary-DNA

Predetermined	
a. Target hybridization volume (µL)	100
b. Target particle OD_{550} (in target hybridization volume)	10 to 20
c. Stock particle OD_{550}	See Step 37
d. Concentration of compDNA (µM)	500
e. 2x DNA hybridization buffer volume (µL)	50
f. Loading capacity of compDNA (nM / OD_{550}) [a]	150
Calculated	
g. Particle volume needed (µL) [b]	(a * b) / c
h. Total hybridization capacity of compDNA (µM)[c]	(b * f) / 1000
i. compDNA volume (3x capacity excess; µL)	(3 * h * a) / d
j. Extra TE-Tween volume (µL)	a - e - g - i, or 0

[a]When loading antibody onto 2 µm particles, the loading capacity is 20 nM/OD_{550}[20]. These values must be determined for each biomolecule species and particle size. 200 nm diameter nanoparticle compDNA loading capacity is between 1000-2000 nM / OD_{550} and the 8 µm particles load between 12-20 nM / OD_{550}, depending on batch-to-batch variation. Antibody loading capacity has not determined for the nanoparticles or 8 µm particles.

[b]If this volume exceeds 50 µL, centrifuge this particle volume as previously described and remove supernatant until 50 µL remains. Adjust the calculation for Extra TE-Tween volume accordingly.

[c]This value represents the total loading capacity of all represented compDNAs. If ratiometric particles are used, this value should be distributed between each sequence based on the particle scaffold DNA surface ratio.

Table 3.5. Troubleshooting table

Step	Problem	Possible Reason	Solution
32	Poor PLGA-PEG-DNA conjugation or conjugate band intensity weak compared to unreacted DNA band	Improperly purified PLGA-PEG-Mal contains maleimide-bearing precursors used during vendor polymer fabrication	Purify PLGA-PEG-Mal via phase precipitation. If not solved, contact vendor
		Large amount of disulfide-DNA formed, evident from the band between the free DNA and PLGA-PEG-DNA bands.	Verify accurate EDTA concentration and reduce DNA concentration used after precipitation and resuspension.
		Improper moisture control can lead to maleimide hydrolysis in PLGA-PEG-Mal	Allow polymer container from freezer to warm to room temperature before opening to reduce condensation. Backfill with desiccated, inert gas before closing. Store in freezer desiccation chamber.
50	Large aggregates seen after sonication	Improper mixture of conjugation reaction components	Ensure that the unmodified PLGA is thoroughly dissolved before adding addition reaction components. Vortex the reaction tube before sonication and after two sonication cycles.
90	Low amount of DNA loading or off-target surface DNA ratios	PLGA-PEG-DNA sequence batches with varying conjugation efficiencies	PLGA-PEG-DNA conjugation efficiency should be tracked. If one batch failed or had low conjugation efficiency, the reaction should have been redone and the poor conjugate should not have been used to fabricate particles.
		Polymer concentration too high after diluting DMSO-degraded particles, leading to reaggregation	After diluting the DMSO-degraded particles, do not exceed 1-2 OD_{550} per 100 µL. Minimize wait-time before plate-reader analysis.
		Improper particle handling during spin-down steps or dilutions	During supernatant removal steps, ensure that particles are not accidently removed. Ensure thorough mixing before any dilutions or aliquoting.
		Particle scaffold fidelity is impaired due to particle age or mishandling	During lyophilized particle resuspension, select proper solution to not increase salt concentration. Monitor particle DNA loading over time, as the maleimide-thiol bond can hydrolyze, leading to a less dense scaffold.
		Improper ratio-mixture of PLGA-PEG-DNAs prior to particle fabrication	When drying polymers at a fixed ratio, ensure that the volumes mixed are accurate and no liquid is stuck inside the pipette tip.
100	Particle sizes are highly variable between batches	Incorrect amount of unmodified PLGA	Ensure the unmodified PLGA amount is within ±1% weight target between batches
		Improper mixture of particle fabrication components	Ensure that all components are thoroughly mixed prior to emulsification steps. Pay extra attention to the pipetting volumes for viscous or volatile components.
		Evaporation of EtOAc during mixing	Cool all liquid reagents on ice before mixing and avoid heat transfer from hands by holding tubes away from bottom. Reduce time that volatile tubes are opened.

Table 3.5. Continued

Step	Problem	Possible Reason	Solution
146	Low Ab-DNA gel band intensity	Poor conjugation efficiency	Titrate DNA amount to find optimal concentration; if no conjugation is observed, verify quality of the compDNA and/or use fresh TCEP. Ensure quality of the NHS-PEG-Mal linker and keep in proper storage conditions.
		Incorrect staining or gel imaging procedure	Verify staining reagent is compatible with selected gel-type. Ensure the correct pmol of biomolecule was loaded in the lanes. Make sure that the gel-doc voltage and filter-channel is appropriate for the dye used.
170	Low antibody signal on particle surface	Poor or incorrect dye-labeling	Increase the dye-to-antibody ratio and verify the reaction calculations are correct. If still low signal, verify NHS-dye concentration or repeat labeling reaction
		DNA impurities leading to competition for hybridization	Ensure that the Ab-DNA purity is above 95% for removing unreacted DNA in Step 147; perform additional column purifications and increase stringency on A_{280} / A_{260} cutoffs for elution collection.
190	Poor T cell expansion	Donor variation	Evaluate multiple donors as some may just have poor expansion at baseline. Compare with a gold-standard expansion reagent, like Dynabeads, to ensure the biomaterial is not at fault.
		Low antibody activity due to improper handling	Verify antibody structural integrity using SDS-PAGE. Perform cell-staining studies using stock Ab-DNA and comparing binding with unmodified controls (flow cytometry). Perform new conjugation with newly purchased antibody if the stock unmodified antibody quality is suspected.
		Incorrect number of particles given	It is critical to not lose particles during wash steps. Prior to adding to culture, remeasure the stock particle OD_{550} to ensure the correct volume of particles are added.

Table S3.1. Reagent and equipment table

-Reagents listed by procedural section-
PLGA-PEG-DNA synthesis
PLGA10k-PEG5k-Malemide (Akina, cat. no. AI053)
3' Thiol-DNA (Integrated DNA Technologies, large-scale custom synthesis)
500 mM Tris(2-carboxyethyl)phosphine (TCEP; Sigma, cat. no. 646547)
Glen Gel-Pak 0.2 desalting column (Glen, cat. no. 61-5002-05)
Glen Gel-Pak 1.0 desalting column (Glen, cat. no. 61-5010-05)
1 M Tris-HCl pH 8.0 (Fisher, cat. no. AAJ22638AP)
500 mM EDTA pH 8.0 (Fisher, cat. no. 50-841-658)
3 M Sodium acetate (EMD, cat. no. 127-09-3)
Ethanol, 200 proof (EtOH; VWR, cat. no. TX89125-172SFU)
N,N-dimethylformamide (DMF; Sigma-Aldrich, cat. no. D158550)
Triethylamine (Et3N; Sigma Aldrich, 471283) Caution: triethylamine is volatile. Handle in a fumehood with proper PPE.
2x TBE-Urea sample buffer (Thermo, cat. no. LC6876)
10x TBE buffer (Biorad, cat. no. 1610733)
15% TBE-Urea gel (Thermo, cat. no. EC68855BOX)
10000x Sybr Gold (Life Technologies Corporation, cat. no. S11494)
Hydrochloric acid (Sigma, cat. no. 320331)
Sodium hydroxide (Sigma, cat. no. 71690)
Nitrogen gas
PLGA particle fabrication
Purified, deionized water (Purification system; Sartorius, Arium Mini)
PLGA 50:50 38K-54K (Unmodified PLGA; Sigma, cat. no. 719900)
Ethyl acetate (EtOAc; Sigma, cat. no. 319902)
Sodium citrate (Sigma, cat. no. S1804)
Sodium chloride (Sigma, cat. no. S9625)
Magnesium chloride (Sigma, cat. no. M8266)
Poly(vinyl alcohol) 31K (PVA; Sigma, cat. no. 81381)
40 µm filter (Fisher, cat. no. 22-363-547)
Tween 20 (Sigma, cat. no. P9416)
Liquid nitrogen
Particle DNA loading and size quantification
Razor blade (Fisher, cat. no. 12-640)
3' Amine-modified fluorescent DNA (Biosearch, custom synthesis)
Dimethyl sulfoxide (DMSO; Sigma, cat. no. D2438)
10x phosphate-buffered saline (PBS; Calbiochem, cat. no. 6506)
Microscope slides, frosted (Corning, cat. no. 2948)
Coverslip 22x22 (Fisher, cat. no. 50-365-603)
Clear nail-polish (Fisher, cat. no. 50949071)
Disposable cuvette (VWR cat. no. 47743-834)
Antibody conjugation with DNA
Anti-human CD3, Clone: OKT-3 (BioXCell, cat. no. BE0001-2, RRID: AB_1107632)
Anti-human CD28, Clone: 9.3 (BioXCell, cat. no. BE0248, RRID: AB_2687729)
MAL-dPEG4-NHS linker (Quanta Biodesign, cat. no. 10214)
HEPES (Fisher, cat. no. BP310-500)
3' amine-modified dyeless DNA (Integrated DNA Technologies, custom synthesis)
Antibody-DNA purification
Disposable 2mL resin gravity column kit (Thermo, cat. no. 29920)
Protein-G resin beads (Genscript, cat. no. L00209)
Glycine (Sigma, cat. no. G8898)
10K MWCO dialysis column, 50 mL (Thermo, cat. no. 88404)
microBCA kit (Thermo, cat. no. 90358)
1 M Triethylammonium acetate buffer (TEAA; Sigma, cat. no. 90358)
Sodium phosphate monobasic (sodium phosphate; Sigma, cat. no. S8282)
Sodium azide (Thermo, cat. no. 190380050)
Tris-glycine 4-20% Gel (Thermo, cat. no. XP04205BOX)
Tris-MOPS-SDS running buffer powder (GenScript, cat. no. M00138)

Table S3.1. *Continued*

-Reagents listed by procedural section-
Preparation of antibodies for surface loading quantification
AlexaFluor488 carboxylic acid, succinimidyl ester (NHS-AF488; Thermo, cat. no. A20000)
AlexaFluor647 carboxylic acid, succinimidyl ester (NHS-AF647; Thermo cat. no. A20006)
Zeba-spin desalting column (Thermo, cat. no. 87766)
T cell isolation and culture
RPMI + GlutaMAX (Thermo, cat. no. 61870036)
Fetal Bovine Serum (OmegaScientific, cat. no. HS-20)
Penicillin (1E4 U/mL) + Streptomycin (10 mg/mL) (Thermo, cat. no. 15140-122)
1 M HEPES (Thermo, cat. no. 15630130)
100 mM Sodium pyruvate (Thermo, cat. no. 11360070)
Human CD3/CD28 Dynabeads (Thermo, cat. no. 111.31D)
EasySep CD4+ T cell enrichment kit (StemCell, cat. no. 17952)
EasySep CD8+ T cell enrichment kit (StemCell, cat. no. 17953)
Fixation/permeabilization kit (Thermo, cat. no. 00-5523-00)
Fixable viability dye eF780 (Thermo, cat. no. 65-0865-14)
Anti-human CD45RA-BV605 (Biolegend, cat. no. 304134)
Anti-human CCR7-BV711 (BD, cat. no. 566602)
Anti-human LAG-3 PerCP-eF710 (Invitrogen, cat. no. 46-2239-42)
Anti-human PD-1 BV421 (BD, cat. no. 562516)
Anti-human TIM-3-PE-CF594 (BD, cat. no. 565560)
Anti-human CD27-PE (BD, cat. no. 557330)
Human IL-2 (Teceleukin; Roche Ro 23-6019)
0.5 M EDTA, sterile (Thermo, cat. no. 15575-038)
1x PBS, pH 7.4, calcium/magnesium free (Thermo, cat. no. 10010-023)
Plasticware
2.0 mL eppendorf tube (Eppendorf, cat. no. 022363352)
15 mL conical tube (Fisher, cat. no. 1495949B)
50 mL conical tube (Fisher, cat. no. 14-959-49A)
Disposable spatula (VWR, cat. no. 80081-188)
Disposable weight-boat (Ted Pella, cat. no. 20158)
10 mL Luer-lock syringe (VWR, cat. no. 76124-664)
10 mL serological pipette (Fisher, cat. no. 1367827F)
96-flat-well plate; cell-culture treated (Thermo, cat. no. 167008)
Cryovials (Sigma, cat. no. CLS430659)
0.22 µM PES stericup media filter (Sigma, cat. no. S2GPU02RE)
96-well flat-bottom plate; black (Fisher, cat. no. 14245177)
Equipment related to particle fabrication
Vortex (VWR, cat. no. 97043-562)
Benchtop centrifuge (Beckman, Allegra-6R)
Benchtop microcentrifuge (Fisher, accuSpin Micro 17)
Benchtop pH-meter (Fisher, Accumet AB150)
Nanodrop One UV-vis spectrophotometer (Thermo, cat. no. 13-400-518)
Analytical balance scale (Fisher, cat. no. 01-913-921)
SpeedVac concentrator (Thermo, SPD121P)
Refrigerated vapor trap (Thermo, RVT400)
Dry-vacuum pump (SigmaAldrich, cat. no. Z411906)
Orbital shaker (VWR, cat. no. 490000-128)
Parafilm (Genesee, cat. no. 16-100)
Pyrex glassware 250mL beaker (Fisher, cat. no. 02-555-25B)
Ultrasonic waterbath (VWR 75T)
Magnetic stir plate (Cimarec Model #SP131325)
Micro stir-bar (Fischer, cat. no. 1451364SIX
Probe sonicator (Sonicator, Qsonica S-4000)
Lyophilization chamber (SP Scientific Advantage Plus ES-53)
Spinning disk confocal (CSU-22 and Nikon Ti)
Microplate spectrophotometer (Molecular Devices SpectraMax M5)

Table S3.1. *Continued*

-Reagents listed by procedural section-
Equipment related to protein bioconjugation
Gel laser scanner (GE Typhoon FLA 9000)
Gel image doc (Azure c150 Gel Doc)
Heating block (Fisher, cat. no. 11-718-8)
Gel electrophoresis power supply (Thermo, cat. no. PS0300)
Gel electrophoresis cell (Thermo, cat. no. EI0001)
Serological pipette controller (Fisher, cat. no. NC0165100)
Tube racks (Thermo, cat. no. 8850)
Equipment for T cell isolation and culture
Incubator (37°C, 5% CO2)
Heated waterbath (Fisher Isotemp 205)
Flow cytometer (BD LSR-Fortessa, Thermo Attune)
Inverted bright-light microscope (Leica DM4000M)
Hemacytometer (Sigma, cat. no. Z359629)
50 mL EasySep magnet (StemCell, cat. no. 18002)
Coolcell (Corning, cat. no. CLS432002)
Liquid nitrogen cryo-tank
Software
FlowJo version 10 (https://www.flowjo.com/solutions/flowjo)
Graphpad Prism version 9 (https://www.graphpad.com/)
Excel (https://www.microsoft.com/en-us/microsoft-365/excel)
ImageJ (https://imagej.nih.gov/ij/ and https://imagej.nih.gov/nih-image/manual/tech.html)

I. BOXES

Box 3.1. Sonication settings for particle fabrication

The following sonication settings were chosen for the S-4000 probe sonicator (Qsonica). The settings should be adjusted for other sonication systems and yielded particles should be quality- checked to match the characteristics described within this protocol.
1. Total energy: 230-250 J
2. Amplitude: 30
3. Pulse sequence timing: 5 seconds on, 10 seconds off
4. Total sonication time: 25 seconds (5 total pulse sequences)

Box 3.2. Equations for determining the DNA concentration within antibody-DNA solution

Perform the following steps for determining the specific concentration contributions from antibody and DNA within the antibody-DNA conjugate solution:

1. Measure the A260 and A280 for dilutions of 1) purified Ab-DNA and 2) pure antibody (Pure-Ab).
2. Record the dilution factor, D, used to measure the Ab-DNA A260 and A280.
3. (Equation 1) A280 (Ab Component of Ab-DNA) * D / 1.33 = antibody mg/mL
4. Solve for A280 (Ab Component of Ab-DNA) where the antibody mg/mL was calculated from MicroBCA in Step 143.
5. (Equation 2) A280 (Pure-Ab) / A260 (Pure-Ab) = G. Solve for G.
6. (Equation 3) A280 (Ab Component of Ab-DNA) / A260 (Ab Component of Ab-DNA) = G.
7. Solve Equation 3 for A260 (Ab Component of Ab-DNA), where A280 (Ab Component of Ab-DNA) is solved in Line iv and G is solved in Line v.
8. (Equation 4) A260(Ab-DNA) = A260(DNA component of Ab-DNA) + A260(Ab component of Ab-DNA)
9. Solve Equation 4 for A260 (DNA component of Ab-DNA) using the A260 (Ab-DNA) measured on Nanodrop and the A260 (Ab component of Ab-DNA) solved in line vii.
10. Solve for DNA concentration in the stock solution with A260 (DNA component of Ab- DNA) * D / (Extinction coefficient of DNA used for conjugation) = DNA µM.

Box 3.3. Quantification of particle surface loading using flow cytometry

Flow cytometry should be performed including single-color and blank controls. The median fluorescent intensities (MFIs) can be used to calculate the antibody surface occupancy from the below equations. Optional normalization to the particle DNA loading can be performed for more convenient comparisons of surface ratios between particles batches when comparing particles with varied total surface protein density. This method is useful for comparing surface DNA ratios but cannot be used to compare DNA densities between batches.

1. Surface occupancy of antibody (%αCD3)

    - %αCD3 = (MFIαCD3 - MFIBlank-Particle) / (MFISingle-Color-Control-αCD3 - MFIBlank-Particle), where the MFI is the signal coming from the respective channel as the αCD3 antibody dye. Repeat for %αCD28 using relevant values.

2. Ratio of αCD3:αCD28

    - If %αCD3 > %αCD28, then the ratio of αCD3:αCD28 is (%αCD3 / %αCD28) : 1

    - If %αCD3 < %αCD28, then the ratio of αCD3:αCD28 is 1 : (% αCD28 / %αCD3)

3. Optional: Normalization of surface occupancy

    - %αCD3norm = (%αCD3) / (%αCD3 + %αCD28), repeat similar calculation for normalizing %αCD28 using relevant values.

J. REFERENCES

1. Mitchell, M. J. et al. Engineering precision nanoparticles for drug delivery. *Nat Rev Drug Discov* **20**, 101–124 (2021).

2. Blanco, E., Shen, H. & Ferrari, M. Principles of nanoparticle design for overcoming biological barriers to drug delivery. *Nat Biotechnol* **33**, 941–951 (2015).

3. Dellacherie, M. O., Seo, B. R. & Mooney, D. J. Macroscale biomaterials strategies for local immunomodulation. *Nat Rev Mater* **4**, 379–397 (2019).

4. Wang, H. & Mooney, D. J. Biomaterial-assisted targeted modulation of immune cells in cancer treatment. *Nature Mater* **17**, 761–772 (2018).

5. Waldman, A. D., Fritz, J. M. & Lenardo, M. J. A guide to cancer immunotherapy: from T cell basic science to clinical practice. *Nat Rev Immunol* **20**, 651–668 (2020).

6. Tan, S., Li, D. & Zhu, X. Cancer immunotherapy: Pros, cons and beyond. *Biomedicine & Pharmacotherapy* **124**, 109821 (2020).

7. Sterner, R. C. & Sterner, R. M. CAR-T cell therapy: current limitations and potential strategies. *Blood Cancer J.* **11**, 1–11 (2021).

8. Romano, M., Fanelli, G., Albany, C. J., Giganti, G. & Lombardi, G. Past, Present, and Future of Regulatory T Cell Therapy in Transplantation and Autoimmunity. *Frontiers in Immunology* **10**, (2019).

9. Ferreira, L. M. R., Muller, Y. D., Bluestone, J. A. & Tang, Q. Next-generation regulatory T cell therapy. *Nat Rev Drug Discov* **18**, 749–769 (2019).

10. Herold, K. C. et al. An Anti-CD3 Antibody, Teplizumab, in Relatives at Risk for Type 1 Diabetes. *New England Journal of Medicine* **381**, 603–613 (2019).

11. Balcerek, J. et al. Polyclonal Regulatory T Cell Manufacturing Under cGMP: A Decade of Experience. *Frontiers in Immunology* **12**, (2021).

12. Dong, S. et al. The effect of low-dose IL-2 and Treg adoptive cell therapy in patients with type 1 diabetes. *JCI Insight* **6**, e147474 (2021).

13. Lin, M. J. et al. Cancer vaccines: the next immunotherapy frontier. *Nat Cancer* **3**, 911–926 (2022).

14. Larson, R. C. & Maus, M. V. Recent advances and discoveries in the mechanisms and functions of CAR T cells. *Nat Rev Cancer* **21**, 145–161 (2021).

15. Tang, L. et al. Enhancing T cell therapy through TCR-signaling-responsive nanoparticle drug delivery. *Nat Biotechnol* **36**, 707–716 (2018).

16. Bonati, L. & Tang, L. Cytokine engineering for targeted cancer immunotherapy. *Current Opinion in Chemical Biology* **62**, 43–52 (2021).

17. Hwang, J.-R., Byeon, Y., Kim, D. & Park, S.-G. Recent insights of T cell receptor-mediated signaling pathways for T cell activation and development. *Exp Mol Med* **52**, 750–761 (2020).

18. Veerman, R. E., Güçlüler Akpinar, G., Eldh, M. & Gabrielsson, S. Immune Cell-Derived Extracellular Vesicles – Functions and Therapeutic Applications. *Trends in Molecular Medicine* **25**, 382–394 (2019).

19. Chang, J. T., Wherry, E. J. & Goldrath, A. W. Molecular regulation of effector and memory T cell differentiation. *Nat Immunol* **15**, 1104–1115 (2014).

20. Huang, X. et al. DNA scaffolds enable efficient and tunable functionalization of biomaterials for immune cell modulation. *Nat. Nanotechnol.* **16**, 214–223 (2021).

21. Majedi, F. S. et al. Augmentation of T-Cell Activation by Oscillatory Forces and Engineered Antigen-Presenting Cells. *Nano Lett.* **19**, 6945–6954 (2019).

22. Cheung, A. S., Zhang, D. K. Y., Koshy, S. T. & Mooney, D. J. Scaffolds that mimic antigen presenting cells enable ex vivo expansion of primary T cells. *Nat Biotechnol* **36**, 160–169 (2018).

23. Rhodes, K. R., Meyer, R. A., Wang, J., Tzeng, S. Y. & Green, J. J. Biomimetic tolerogenic artificial antigen presenting cells for regulatory T cell induction. *Acta Biomaterialia* **112**, 136–148 (2020).

24. Kim, J. V., Latouche, J.-B., Rivière, I. & Sadelain, M. The ABCs of artificial antigen presentation. *Nat Biotechnol* **22**, 403–410 (2004).

25. Boozer, C., Ladd, J., Chen, S. & Jiang, S. DNA-Directed Protein Immobilization for Simultaneous Detection of Multiple Analytes by Surface Plasmon Resonance Biosensor. *Anal. Chem.* **78**, 1515–1519 (2006).

26. Liu, Y. & Yu, J. Oriented immobilization of proteins on solid supports for use in biosensors and biochips: a review. *Microchim Acta* **183**, 1–19 (2016).

27. Bilal, M., Asgher, M., Cheng, H., Yan, Y. & Iqbal, H. M. N. Multi-point enzyme immobilization, surface chemistry, and novel platforms: a paradigm shift in biocatalyst design. *Critical Reviews in Biotechnology* **39**, 202–219 (2019).

28. Smith, M. R., Tolbert, S. V. & Wen, F. Protein-Scaffold Directed Nanoscale Assembly of T Cell Ligands: Artificial Antigen Presentation with Defined Valency, Density, and Ratio. *ACS Synth. Biol.* **7**, 1629–1639 (2018).

29. Wang, X. & Rivière, I. Clinical manufacturing of CAR T cells: foundation of a promising therapy. *Molecular Therapy - Oncolytics* **3**, 16015 (2016).

30. Arcangeli, S. et al. CAR T cell manufacturing from naive/stem memory T lymphocytes enhances antitumor responses while curtailing cytokine release syndrome. *J Clin Invest* **132**, (2022).

31. López-Cantillo, G., Urueña, C., Camacho, B. A. & Ramírez-Segura, C. CAR-T Cell Performance: How to Improve Their Persistence? *Frontiers in Immunology* **13**, (2022).

32. Arcangeli, S. et al. Next-Generation Manufacturing Protocols Enriching TSCM CAR T Cells Can Overcome Disease-Specific T Cell Defects in Cancer Patients. *Frontiers in Immunology* **11**, (2020).

33. Elmowafy, E. M., Tiboni, M. & Soliman, M. E. Biocompatibility, biodegradation and biomedical applications of poly(lactic acid)/poly(lactic-co-glycolic acid) micro and nanoparticles. *J. Pharm. Investig.* **49**, 347–380 (2019).

34. Roybal, K. T. et al. Precision Tumor Recognition by T Cells With Combinatorial Antigen-Sensing Circuits. *Cell* **164**, 770–779 (2016).

35. Maynard, S. A., Winter, C. W., Cunnane, E. M. & Stevens, M. M. Advancing Cell-Instructive Biomaterials Through Increased Understanding of Cell Receptor Spacing and Material Surface Functionalization. *Regen. Eng. Transl. Med.* **7**, 533–547 (2021).

36. Zhong, J. X., Raghavan, P. & Desai, T. A. Harnessing Biomaterials for Immunomodulatory-Driven Tissue Engineering. *Regen. Eng. Transl. Med.* (2022) doi:10.1007/s40883-022-00279-6.

37. Mertgen, A.-S. et al. Multifunctional Biomaterials: Combining Material Modification Strategies for Engineering of Cell-Contacting Surfaces. *ACS Appl. Mater. Interfaces* **12**, 21342–21367 (2020).

38. Bao, G., Mitragotri, S. & Tong, S. Multifunctional Nanoparticles for Drug Delivery and Molecular Imaging. *Annu Rev Biomed Eng* **15**, 253–282 (2013).

39. Saminathan, A., Zajac, M., Anees, P. & Krishnan, Y. Organelle-level precision with next generation targeting technologies. *Nat Rev Mater* **7**, 355–371 (2022).

40. Lagreca, E. et al. Recent advances in the formulation of PLGA microparticles for controlled drug delivery. *Prog Biomater* **9**, 153–174 (2020).

41. Yu, W., Liu, R., Zhou, Y. & Gao, H. Size-Tunable Strategies for a Tumor Targeted Drug Delivery System. *ACS Cent Sci* **6**, 100–116 (2020).

42. Pradal, J. et al. Effect of particle size on the biodistribution of nano- and microparticles following intra-articular injection in mice. *International Journal of Pharmaceutics* **498**, 119–129 (2016).

43. Adakkattil, R., Thakur, K. & Rai, V. Reactivity and Selectivity Principles in Native Protein Bioconjugation. *The Chemical Record* **21**, 1941–1956 (2021).

44. Trads, J. B., Tørring, T. & Gothelf, K. V. Site-Selective Conjugation of Native Proteins with DNA. *Acc. Chem. Res.* **50**, 1367–1374 (2017).

45. Saha, B., Songe, P., H. Evers, T. & J. Prins, M. W. The influence of covalent immobilization conditions on antibody accessibility on nanoparticles. *Analyst* **142**, 4247–4256 (2017).

46. Zamecnik, C. R., Lowe, M. M., Patterson, D. M., Rosenblum, M. D. & Desai, T. A. Injectable Polymeric Cytokine-Binding Nanowires Are Effective Tissue-Specific Immunomodulators. *ACS Nano* **11**, 11433–11440 (2017).

47. Makaraviciute, A., Jackson, C. D., Millner, P. A. & Ramanaviciene, A. Considerations in producing preferentially reduced half-antibody fragments. *Journal of Immunological Methods* **429**, 50–56 (2016).

48. Sapsford, K. E. et al. Functionalizing Nanoparticles with Biological Molecules: Developing Chemistries that Facilitate Nanotechnology. *Chem. Rev.* **113**, 1904–2074 (2013).

49. Khandare, J. & Minko, T. Polymer–drug conjugates: Progress in polymeric prodrugs. *Progress in Polymer Science* **31**, 359–397 (2006).

50. Martínez-Jothar, L. et al. Insights into maleimide-thiol conjugation chemistry: Conditions for efficient surface functionalization of nanoparticles for receptor targeting. *Journal of Controlled Release* **282**, 101–109 (2018).

51. Chiodi, E., Marn, A. M., Geib, M. T. & Ünlü, M. S. The Role of Surface Chemistry in the Efficacy of Protein and DNA Microarrays for Label-Free Detection: An Overview. *Polymers* **13**, 1026 (2021).

52. Pei, X. et al. Putting precision and elegance in enzyme immobilisation with biorthogonal chemistry. *Chemical Society Reviews* **51**, 7281–7304 (2022).

53. Wasserberg, D., Cabanas-Danés, J., Subramaniam, V., Huskens, J. & Jonkheijm, P. Orthogonal supramolecular protein assembly on patterned bifunctional surfaces. *Chem. Commun.* **54**, 1615–1618 (2018).

54. Meder, F., Kaur, S., Treccani, L. & Rezwan, K. Controlling Mixed-Protein Adsorption Layers on Colloidal Alumina Particles by Tailoring Carboxyl and Hydroxyl Surface Group Densities. *Langmuir* **29**, 12502–12510 (2013).

55. Wongrakpanich, A., Khunkitchai, N., Achayawat, Y. & Suksiriworapong, J. Ketorolac-Loaded PLGA-/PLA-Based Microparticles Stabilized by Hyaluronic Acid: Effects of Formulation Composition and Emulsification Technique on Particle Characteristics and Drug Release Behaviors. *Polymers* **15**, 266 (2023).

56. Makadia, H. K. & Siegel, S. J. Poly Lactic-co-Glycolic Acid (PLGA) as Biodegradable Controlled Drug Delivery Carrier. *Polymers (Basel)* **3**, 1377–1397 (2011).

57. Vivek, K., Harivardhan Reddy, L. & Murthy, R. S. R. Comparative Study of Some Biodegradable Polymers on the Entrapment Efficiency and Release Behavior of Etoposide from Microspheres. *Pharmaceutical Development and Technology* **12**, 79–88 (2007).

58. Ghasemiyeh, P. & Mohammadi-Samani, S. Polymers Blending as Release Modulating Tool in Drug Delivery. *Frontiers in Materials* **8**, (2021).

59. Fu, J. et al. DNA-Scaffolded Proximity Assembly and Confinement of Multienzyme Reactions. *Top Curr Chem (Z)* **378**, 38 (2020).

60. Wiener, J., Kokotek, D., Rosowski, S., Lickert, H. & Meier, M. Preparation of single- and double-oligonucleotide antibody conjugates and their application for protein analytics. *Sci Rep* **10**, 1457 (2020).

61. van der Sleen, L. M. & Tych, K. M. Bioconjugation Strategies for Connecting Proteins to DNA-Linkers for Single-Molecule Force-Based Experiments. *Nanomaterials (Basel)* **11**, 2424 (2021).

62. von Witting, E., Hober, S. & Kanje, S. Affinity-Based Methods for Site-Specific Conjugation of Antibodies. *Bioconjugate Chem.* **32**, 1515–1524 (2021).

63. Manning, M. C., Chou, D. K., Murphy, B. M., Payne, R. W. & Katayama, D. S. Stability of Protein Pharmaceuticals: An Update. *Pharm Res* **27**, 544–575 (2010).

64. Frokjaer, S. & Otzen, D. E. Protein drug stability: a formulation challenge. *Nat Rev Drug Discov* **4**, 298–306 (2005).

65. Wang, W. Protein aggregation and its inhibition in biopharmaceutics. *International Journal of Pharmaceutics* **289**, 1–30 (2005).

66. Themeli, M., Rivière, I. & Sadelain, M. New Cell Sources for T Cell Engineering and Adoptive Immunotherapy. *Cell Stem Cell* **16**, 357–366 (2015).

67. Stock, S., Schmitt, M. & Sellner, L. Optimizing Manufacturing Protocols of Chimeric Antigen Receptor T Cells for Improved Anticancer Immunotherapy. *Int J Mol Sci* **20**, 6223 (2019).

68. Eskandari, S. K. et al. Regulatory T cells engineered with TCR signaling–responsive IL-2 nanogels suppress alloimmunity in sites of antigen encounter. *Science Translational Medicine* **12**, eaaw4744 (2020).

69. Ghaffari, S. et al. Optimizing interleukin-2 concentration, seeding density and bead-to-cell ratio of T-cell expansion for adoptive immunotherapy. *BMC Immunol* **22**, 1–9 (2021).

70. Techniques. https://imagej.nih.gov/nih-image/manual/tech.html.

71. Wang, Y. et al. Phase transitions in human IgG solutions. *J Chem Phys* **139**, 121904 (2013).

72. Wang, S. S., Yan, Y. (Susie) & Ho, K. US FDA-approved therapeutic antibodies with high concentration formulation: summaries and perspectives. *Antibody Therapeutics* **4**, 262–272 (2021).

73. Vincent, M. P., Navidzadeh, J. O., Bobbala, S. & Scott, E. A. Leveraging self-assembled nanobiomaterials for improved cancer immunotherapy. *Cancer Cell* **40**, 255–276 (2022).

74. Danaei, M. et al. Impact of Particle Size and Polydispersity Index on the Clinical Applications of Lipidic Nanocarrier Systems. *Pharmaceutics* **10**, 57 (2018).

75. Fass, D. & Thorpe, C. Chemistry and Enzymology of Disulfide Cross-linking in Proteins. *Chem Rev* **118**, 1169–1198 (2018).

76. Delcassian, D., Sattler, S. & Dunlop, I. E. T cell immunoengineering with advanced biomaterials. *Integrative Biology* **9**, 211–222 (2017).

77. Wang, C., Sun, W., Ye, Y., Bomba, H. N. & Gu, Z. Bioengineering of Artificial Antigen Presenting Cells and Lymphoid Organs. *Theranostics* **7**, 3504–3516 (2017).

78. Si, X., Xiao, L., Brown, C. E. & Wang, D. Preclinical Evaluation of CAR T Cell Function: In Vitro and In Vivo Models. *Int J Mol Sci* **23**, 3154 (2022).

Chapter 4

Diverse activation, expansion, and phenotypic maturation of human regulatory T cell subsets: implications for cellular manufacturing

A. ABSTRACT

Regulatory T cell (Treg) therapy has emerged as a promising approach for reestablishing immune tolerance. Despite the well-tolerated and safe nature of these therapies, their therapeutic efficacy remains uncertain. A significant challenge in Treg therapy lies in the manufacturing process, characterized by high variability and frequent failures in Treg expansion. This variability has been closely linked to the pre-expansion Treg phenotypic state, with current activation methods inadequate to expand activated, HLA-DR+ effector Treg subsets. Recognizing the need to precisely understand the activation requirements and genetic drivers of proliferation among these subsets, we employed a DNA-scaffolded biomaterial platform capable of finely tuning the input activation signals, specifically agonistic αCD3 and αCD28 antibodies. This platform has previously shown promise in T cell manufacturing by enabling the control over the activation signal density and relative stoichiometry. Using this technology, we investigated the differential expansion and phenotypic fates of clinically relevant Treg subsets, where initial findings indicated that increasing the αCD3 and αCD28 signals were insufficient for driving robust effector Treg expansion. Employing paired scRNAseq and scTCRseq, we used TCR-based tracing to monitor clonal expansion and mapped the transcriptomic profiles linked to Treg expansion. Our findings revealed that highly proliferative Tregs, particularly those within naïve and central memory phenotypes, exhibit unique transcriptional programs, including the upregulation of cAMP-degrading enzymes like PDE4D and downregulation of cAMP-producing adenylate cyclases, which diverge significantly from those of poorly proliferating cells. Moreover, this analysis highlighted the heterogeneity of distinct effector Treg groups, including a high-cytokine-producing T helper-like phenotype—a potential source of Foxp3-unstable Tregs in manufacturing. These findings not only advance our understanding of Treg biology and the technical challenges of Treg manufacturing but also opens new avenues for optimizing Treg therapy through targeted modulation of expansion and effector mechanisms.

B. INTRODUCTION

Regulatory T cells (Tregs) are central to the prevention of immune-mediated tissue damage, playing a critical role in facilitating tolerance in autoimmunity and organ transplantation[1–3]. While the disease-modifying potential of Treg adoptive transfer has been thoroughly demonstrated in preclinical settings across multiple disease contexts, translating these findings into clinically effective therapies has proven challenging. The safety of Treg therapy in clinical trials is well-established, yet achieving therapeutic efficacy remains elusive[2,4]. This gap underscores a pressing need to unravel the complex characteristics that define a therapeutically effective Treg—such as antigen specificity, differentiation state, homing capabilities, stability of the Foxp3 lineage, and proliferative capacity—and whether we can reproducibly manufacture these cells[5–11].

The ex vivo manufacturing of Tregs involves a coordinated process of isolation, purification, expansion, and quality control[1]. While Treg manufacturing is often successful in certain immunologically challenged patient populations, such as for Type 1 Diabetes Mellitus (T1DM), the variability in expansion outcomes and cell yields across donors—which is particularly pronounced in patients with heightened immunological demands like those undergoing organ transplantation—poses significant hurdles[2–4]. This variability is compounded by the effects of immunosuppressive treatments and the physiological alterations associated with organ transplantation on Treg quality and expansion potential. Indeed, the recent UCSF ARTEMIS clinical trial brought these challenges into focus, revealing previously uncommon difficulties in expanding liver-transplant recipient Tregs[3]. Failures in Treg expansion were linked to the expression of activation and effector markers, such as HLA-DR, PD-1 and KLRG1, and the absence of TCF-7, a key proliferative marker, suggesting an intrinsic limitation within the effector-Treg lineage that may impede expansion[12–14].

The concept of Treg phenotypic heterogeneity, particularly in terms of memory differentiation phenotypes (e.g., naïve, memory, effector), further complicates the landscape of Treg therapy. Although it is recognized that different T cell subsets exhibit distinct proliferative responses, activation sensitivities, and differentiation responses, a nuanced understanding of these dynamics in Tregs is lacking[15–21]. The traditional "one-activation-signal-fits-all" approach to Treg expansion may overlook the unique requirements of specific Treg subsets when they are enriched within certain donors, suggesting a potential avenue for enhancing the efficiency of Treg manufacturing protocols.

Methods for investigating Treg activation commonly employ either plate-adsorption, cell-based presentation, or surface-attachment via either covalent (e.g NHS) or non-covalent (e.g Biotin-Streptavidin) to present activation proteins, however these methods have been demonstrated to be difficult to precisely control[22–27] . To address the challenges with previous activation methods, our laboratory has pioneered a biomaterial-based strategy utilizing DNA-hybridization to precisely control the presentation of activation signals on the surface of DNA-scaffolded, polymeric microparticles[26,28]. This approach allows for precise control over the density and stoichiometric ratio of activation signals, which we demonstrated in the targeted activation and expansion of human T cells. Despite its potential in modulating T cell expansion and phenotypic modulation, this strategy has not been previously applied in the context Treg subset biology and manufacturing.

This study employs immune cell engaging particles (ICEps) with tunable αCD3 and αCD28 stimulation to explore the differential activation and expansion of Treg subsets. Our investigations reveal a predominant role for naïve Tregs in bulk Treg expansion, while highlighting the challenges in expanding effector Tregs using conventional αCD3 and αCD28 signals alone. Surprisingly, we observed an enrichment of Foxp3-/Helios- populations within the traditionally highly-suppressive effector subset, correlating with increased activation signal

strength. Through a novel application of combined scRNA/TCRseq analysis, we traced the

trajectories of clonally expanded Tregs, identifying key genes and pathways that govern Treg

proliferation and pinpointing a subset of effector Tregs marked by signatures suggestive of

inflammatory potential or instability. At the time of writing this chapter, we have yet to investigate

the expansion-modifying effects of modulating these proliferation targets. However, the

manipulation of effector Tregs and the potential removal of potentially destabilizing Tregs is

ongoing and has potential implications for the future of Treg manufacturing.

C. METHODS

C.1. Fabrication of DNA-scaffolded particles

DNA-scaffolded, poly-lactic-co-glycolic acid (PLGA) microparticles (average diameter of 2 µm) were fabricated following the procedures detailed in **Chapter 3**[28]. This included the synthesis of PLGA-PEG-DNA, particle fabrication via sonication-mediated emulsification, and verification of DNA-scaffold loading. Particles were created with DNA-surface ratios of 9:1, 3:1, 1:1, 1:3, and 1:9, selected based on the maximal loading requirement for specific DNA-cargos.

C.2. Preparation of DNA-conjugated αCD3 and αCD28

αCD3 (clone OKT-3, BioXCell) and αCD28 (clone 9.3, BioXCell) were conjugated to fluorescently-labeled DNA sequences (IDT), denoted as compR or compG, indicating their complementary sequences to the particle DNA scaffold. αCD3-compG-AlexaFluor647 and αCD28-compR-AlexaFluor488 were prepared from lyophilized stock and stored at 4°C.

C.3. Assembly of ICEps with αCD3 and αCD28

The hybridization strategy for particles with DNA-conjugated cargos has been previously published by our group and is documented in **Chapter 3**[28]. Briefly, the day prior to T cell activation, particles were cut from lyophilized stock, washed using water followed by 0.01% TE-Tween-20, and OD550 concentration was measured using Nanodrop. The necessary particle amount for hybridization was determined by calculating the particle excess needed for the cell count within each particle condition. This particle quantity was taken from the stock and diluted so that 50uL of the dilution could be added to each hybridization tube, representing a 2x concentration of the final desired hybridization volume. αCD3-compG-AlexaFluor647 and αCD28-compR-AlexaFluor488 hybridization calculations were determined using the total loading of particles in the hybridization tube and the desired surface coverage of each antibody. Particles used in **Fig 4.1e-g** and **Supplemental Fig. 4.2b,c** used a scaffold-saturation loading

approach, thus hybridization was performed using saturating amounts of αCD3 and αCD28. All other experiments relied on a titration-based loading approach. Particles were hybridized at 37°C for 30 minutes to generate ICEp and stored overnight at 4°C prior before T cell culture.

C.4. Preparation of ICEp for T cell culturing

ICEp preparation was performed sterilely within a biosafety cabinet. Particles were washed three times using sterile, 1x PBS and spun at 300g for 5 minutes at 4°C to fully remove non-hybridized antibodies; sufficient washes were performed so that the estimated residual antibody signal was far less than the minimal amount of antibody delivered by particles. ICEps were resuspended in hIL-2 containing media (see *D.6.*) and diluted such that a maximum of 10μL of particles could be added per well for the highest particle number condition.

C.5. T cell isolation from leukapheresis product

Leukapheresis product (StemCell Technologies) was acquired from healthy donors (<40y/o, non-smoker, BMI under 25) and enriched for T cells same-day. T cell experiments using Tconvs used CD4+ negative selection kits (EasySep, StemCell) to enrich for both Tconv and Treg. Experiments using CD8s required a CD3+ negative selection enrichment kit on a fraction of the initial leukapheresis product. Experiments containing just Tregs used a Treg enrichment kit without CD127 depletion (CD4+ negative selection, CD25+ positive selection). Cells were stained for 1hr at 4°C in PBS-FBS sorting buffer (1x PBs, 3% vol/vol FBS, and 1mM EDTA) before FACs purification (BD, FACAriaII). See **Supplemental Table S4.1** for donor information used in these experiments and **Supplemental Table S4.2** for sorting antibodies. Gating strategies used can be found in **Fig. 4.2a** and **Supplemental Fig. S4.1**.

C.6. T cell culturing with ICEp

T-cells were cultured in RPMI 1640 + GlutaMAX containing 10% heat-inactivated FBS, 10mM HEPES, 1mM sodium pyruvate, combined penicillin (100U/mL) and streptomycin

(0.1mg/mL), and recombinant hIL2 at either 300U/mL for Tregs or 100U/mL for CD4+ Tconvs and CD8+ T cells. Cells were seeded at 25,000 cells per 96 flat-bottom well (0.25E6/mL), activated using ICEp at the denoted particle excess or Dynabeads (1x excess Dynabeads to cells), and maintained at 37°C and 10% CO_2. Media was doubled on day 2 and cells were counted and split back to 0.25E6/mL every other day starting at day 4. Cell counting in **Fig 4.1** was performed using either flow-cytometry assisted, high-throughput liquid handlers (BD HTS, LSR-Fortessa) with dead cells marked using DAPI stain. Cell counting in subsequent experiments used an Incucyte S3 (Sartorius) for detecting live cells via the Calcein-Red-AM stain.

C.7 Calculating T cell expansion thresholds

Background survival and expansion in **Fig 4.1j** and **Supplemental Fig 4.2e** was varied between donors and stimulation rounds. The background signal for each expansion curve, distinguished by each individual donor, αCD28 condition (25, 50, or 75%), and stimulation round (first stimulation or restimulation) was determined using an expanding average window, starting at αCD3 = 0% and increasing until the percent-change—defined as [$|Average_n - Average_{n-1}|$ / $Average_{n-1}$], where n is the number of αCD3 steps after αCD3=0%— between average and the previous average exceeded 50%, indicating that expansion curve was now deviating away from background. The average background signal was defined as the average from αCD3 = 0% to *n* number of αCD3 steps before the 50% change is reached. After subtracting the background from each matching expansion curve, the expansion values were normalized to the global maximum expansion within each curve. To determine the percent of the maximal response that corresponds to the minimum αCD3 threshold for expansion, we calculated the percent of the global maximum that the background signal contributed to within each expansion curve— defined as [[Average Background Signal]*100]/[Global Maximum Expansion]; these percentages better account for residual background noise which was variable between donors and number of

stimulations. These values ranged from: Treg – 6.06-10.45% for first stimulation and 0.30-1.95% for restimulation; Tconvs – 0.20-3.67% for first stimulation and 0.65-26.92% for restimulation. Using these percentages, the αCD3 was defined as the first αCD3 level that exceeded the background-contributed percentage.

C.8. Flow cytometry and analysis

Expanded cells were washed, stained with a fixable viability dye diluted in 1x PBS for 10 minutes at room temperature before washing. Cells were stained for surface markers using fluorophore-conjugated antibodies diluted in FACs buffer (2g/L BSA and 1g/L sodium azide in 1x PBS) for 30 minutes at 4°C before washing. For intracellular markers, cells were fixed and permeabilized using a Foxp3 transcription factor staining kit (ThermoFisher) for 1 hour before staining for 30 minutes at 4°C before washing and resuspending in FACs buffer. Antibody panels can be found in **Table 4.2**. Fluorescence compensation controls were generated using UltraComp eBeads Plus (ThermoFisher). Cells were analyzed using either a spectral flow cytometer (Aurora, Cytek) or standard flow cytometer (LSR-Fortessa, BD) in the UCSF Parnassus Flowcore. Data was analyzed using FlowJo (BD) using the DownSample, UMAP, FlowSOM, and ClusterExplorer packages. Gating strategy for **Fig. 4.1f,g** and **Fig. S4.2c** can be found in **Supplemental Fig. S4.2a** and gating for **Fig 4.2** and **Supplemental Fig. 4.5** can be found in **Supplemental Fig. 4.4**.

C.9. Preparation of Tregs for scRNA/TCRseq

Tregs were isolated and FACS purified as outlined in *C.5*. A total of 2E6 cells were cryopreserved in CS-10 freezing medium (StemCell Technologies) for use as a pre-expansion sample (Pre). Tregs or CD4+ Tconvs were plated in 24-well plates at 0.375E6 cells/well (0.375E6/mL) and stimulated with either Dynabeads (Dyna sample; 1x excess Dynabead to cell) or CD28 superagonist (SA sample; 5μg/mL final concentration, clone anti-CD28.1). Following

the protocol described in *C.5*, on day 8, SA or Dyna samples were cryopreserved, reserving some for flow cytometry quality control to assess Treg purity. Pre, SA, and Dyna samples were thawed, and live cells enriched using a MACs dead cell removal kit (Miltenyi).

For scRNA/TCRseq, Chromium single cell 5' gene expression and V(D)J libraries were generated according to manufacturer's instructions (10x Genomics). Briefly, cells were loaded into four individual sample wells (two for Pre) on the GEM chip, followed by lysis, reverse transcription, and cDNA amplification via the Chromium Controller Instrument. Prior to sequencing, cDNA was split for V(D)J and gene expression enrichment and PCR amplified. The libraries were sequenced on the NovaSeq X (Illumina). Library preparation was performed by the UCSF Genomics CoLab and sequencing performed by the UCSF Center for Advanced Technology.

C.10. Pre-processing of scRNAseq data

After sequencing, FASTQ files were generated, and reads were aligned to GRch38 human genome reference using 10x Cell Ranger Cloud (version 7.1.0). In total, there were over 28285 cells detected in Pre (34798 average number of reads and 1824 genes per cell), 15888 SA cells (33556 average number of reads and 1664 genes per cell), and 12506 Dyna cells (39872 average number of reads and 1254 genes per cell). Cell Ranger outputs were processed in R using the Seurat package (v5.0.1)[29]. Doublet removal was performed on individual samples using DoubletFinder, with the expected doublet occurrence derived from the number of cells detected from chip loading[30]. Cells with <800 UMIs or <500 gene features were excluded. Additional filtering was performed on mitochondrial gene percentage, typically associated with dying cells, although highly metabolic cells are reported to express a higher fraction of mitochondrial reads[31]. Since these cells are highly viable and are in different activation states (qualified by their expansion fold at the time of analysis), we removed cells from Pre with >10% mitochondrial genes and Dyna/SA cells with >50%. Cells were also

removed if the mitochondria:ribosomal gene ratio was greater than 0.5. Pre and post-samples (SA/Dyna) were separately integrated using reciprocal PCA (RPCA) via Seurat for analysis.

C.11. Processing of scTCRseq data

V(D)J data was processed in the Cell Ranger 10x Cloud as described in *C.10.* Filtered annotated contigs were processed in R and analysis as performed using scRepertoire (v2.0.0)[32]. TCR clones were filtered where the V-J segments annotations from TCR-α and TCR-β were fully defined. Clonal proportions were calculated within each sample, and SA/Pre or SA/Dyna TCR enrichment ratios were calculated; cells where that were detected in Pre but not in SA or Dyna were labeled as "Undetected-SA" or "Undetected-Dyna", respectively, and cells that were not detected in Pre were labeled as "NA" to facilitate future analyses.

C.12. Analysis of scRNA/TCRseq data

A cell-barcode list, including complete TCR clones (concatenated VJ from TCR-α and TCR-β), sample names, and enrichment ratios, facilitated transcriptomic and V(D)J data integration for analysis. Data was normalized and variable gene features were identified, where genes corresponding to TCR variable fragments, ribosomal proteins, mitochondrial proteins were removed from variable gene identification as these have high variance between cells. Principle component analysis (PCA) was performed on variable genes, where the cell-cycle related genes were regressed out due to high variability and confounding of analysis as previously described[29,33]. The top 20 principal components were used to generate a nearest neighbor map, cluster identification, and UMAP dimensionality reduction visualization. Cluster annotations were performed using gene expression modules of known biological significance in Treg identity and function, which was further supported by Seurat and the Clustered DotPlot package within scCustomize (2.0.1). Additional annotation analysis was performed on a cluster-by-cluster basis using differentially expressed genes. Differential gene expression was

performed using Seurat and visualized using volcano plots via the EnhancedVolcano package. Gene set enrichment analysis (GSEA) was performed using Seurat/Enrichr, clusterProfiler (v3.10.1), and the Gene Ontology (GO) and Reactome databases[34–37].

C.13. Statistical analysis

Data analyses for expansion and flow cytometry were performed using GraphPad Prism (v10.1.2) and significance was determined by ns $P > 0.05$, $*P \leq 0.05$, $**P \leq 0.01$, $***P \leq 0.001$, and $****P \leq 0.0001$. scRNA/TCRseq analyses were performed in R (v4.3.2) and the associated packages described in the above methods.

D. RESULTS

D.1. Optimization of ICEp parameters for T cell activation

In **Chapter 3** we described the fabrication and features of ICEps, highlting the unique properties of the DNA-directed particle-loading approach including the simultaneous, decoupled control over the surface stoichiometric ratio and density of immunomodulatory biomolecules, such as αCD3 and αCD28 agonistic antibodies (**Fig. 4.1a**). Using this technology, we previously explored CD4+ and CD8+ T cell expansion using ICEps, noting that parameters such as αCD3/αCD28 surface coverage and particle-to-cell ratio significantly influence expansion[28]. Here, we sought to investigate the effect of these ICEp parameters in expanding CD4+ Tregs in culture. We first fabricated DNA-scaffolded, PLGA microparticles targeting an average diameter of ~2μm, as previously validated for T cell activation (**Fig. 4.1b,c**)[26,28]. We verified the surface stoichiometry of DNA-scaffolds in three different particle formulations designed to capture a wide range of biomolecule relative loadings via the detection of fluorescently-conjugated complementary DNAs (compDNA) (**Fig. 4.1d**). We constructed the final ICEp formulations by hybridizing compDNA-bearing αCD3 and αCD28 onto each particle type in a surface-saturating reaction which reflects the underlying particle scaffold ratio[28].

Our analysis of CD4+, CD127lo, CD25hi Treg expansion over 8 days post-activation with ICEps bearing different levels of αCD3 and αCD28 revealed a pronounced dependence on αCD28 dosage, with expansion peaking after 50% surface coverage (**Fig. 4.1e**). Despite high donor variance, the overall highest ICEp expansion at 90% αCD28 was not statistically different from expansion using commercial Dynabeads. Conversely, CD4+ T conventional (Tconv) cells exhibited less dependence on αCD28 for expansion, showing high expansion after 10% coverage, whose difference was statistically insignificant compared to 50 and 90% (**Supplemental Fig. 4.2b**). ICEp activation maintained Foxp3 expression across various particle formulations despite differing expansion rates. In addition to not initiating expansion, ICEps

bearing either neither αCD3 nor αCD28 led to reduced activation-dependent memory differentiation, indicated by the relatively high proportion of CD45RO- CCR7+ naïve Tregs across donors (**Fig 4.1g**). In contrast, while 90% αCD28 induced the highest average expansion, the majority of cells committed to the CD45RO+ CCR7+ central memory (CM) fate which tended to increase with higher ratios of αCD28 to αCD3. Similar to Tregs, increasing αCD28 tended to increase the proportion of CM within Tconvs (**Supplemental Fig. S4.2c**). Tconvs, however, also differentiate into a mixture of CD45RO+ CCR7- effectors and CM even in the presence of αCD3 alone—where they expand on average of 33-fold—and only maintain naïve Tconv at 100% αCD28 which induced <5 fold expansion. Thus, both cell types tended to differentiate under expansion-inducing stimulation strengths.

To further decouple the specific contributions αCD3 and αCD28, we constructed a two-dimensional matrix of αCD3/αCD28 formulations with an increased range of ICEp doses using a titration-directed surface loading approach (**Fig. 4.1h**). Treg expansion was primarily driven by αCD28 coverage and increasing number of ICEps, with expansion tending to increase at lower αCD3 levels. Further, expansion could not initiate below a αCD28 threshold of 5% despite increasing the ICEp number. The observed expansion benefit gained from increased ICEp doses was primarily driven by increased αCD28 delivery (**Fig. 4.1i**), whereas αCD3 dose failed to model this effect (**Supplemental Fig. 4.2d**). An optimal ICEp amount of 9x was chosen due to the best-fit approaching saturation and to balance with material usage (**Fig. 4.1i**). We then investigated whether αCD3 had a similar expansion threshold behavior by activating Tregs with ICEps generated by titrating αCD3 against fixed amounts of αCD28. Due to varied background expansion and survival, we defined an expansion threshold as the first αCD3 to exceed the background contribution to the maximum expansion within each donor (see Methods). This yielded identical αCD3 thresholds of 0.4% for both first stimulation and restimulation across all donors and αCD28 levels—with the exception of Donor E at 90% αCD28 requiring 2% αCD3 at

first stimulation. Cells initially stimulated with Dynabeads were used for restimulation with ICEps due to the minimal cell numbers available after the first round in ICEp conditions (**Supplemental Fig. S4.2g**). The αCD3 threshold for Tconvs was less clear, yielding thresholds between 0.4% and 2% for both first stimulation and restimulation, with higher αCD3 thresholds calculated with increasing αCD28, likely due to the increased background proliferation confounding the threshold calculation rather than a biological effect (**Supplemental Fig. S4.2e**). Indeed, the Tconv background proliferation tended to increase with higher αCD28. While there was high donor expansion variance in the first stimulation, both Tregs and Tconvs significantly reduced the percent difference between donors during restimulation across all αCD28 levels (**Fig. 4.1k** and **Supplemental Fig. S4.2f,h**).

D.2. Expansion of Treg subsets using ICEp

It has been previously documented that freshly isolated Tregs are highly heterogenous, being composed of multiple different phenotypic states such as naïve, effector, memory, etc, and that these different subsets have varied proliferation magnitudes and sensitivity to stimulation cues[15,18,38–41]. The ARTEMIS trial similarly noted this state heterogeneity and its impact on expansion, highlighting that effector markers like HLA-DR, PD-1, and KLRG-1 negatively correlate with Treg expansion[3]. Since we observed T cell enrichment for a CM phenotype after a single expansion round, the reduction of donor variation upon restimulation prompted us to consider state-specific activation sensitivity and expansion dynamics. Further, we hypothesized that the similar donor response to ICEp upon restimulation may be due to the expansion potential of the first-round enriched phenotype. This led us to examine the activation and expansion responses of distinct Treg subsets, using markers guided by clinical manufacturing relevant subtypes to isolate bulk (non-subsetted), naïve (CD45RA+, HLA-DR-), resting memory (memory, CD45RA- HLA-DR-), and effector (CD45RA-, HLA-DR+) Tregs with a CD4+, CD127lo, and CD25hi phenotype (**Fig. 4.2a**). Due to Treg memory and its associated

definitions being an actively evolving area, we use effector above to describe a pool of both effector memory—which retain proliferative capacity—and effector—specialized for immunosuppressive effector function but may be relatively short-lived[13,38,42–44].

Using ICEps optimized for αCD3 and αCD28 threshold and saturating limits, we examined the expansion response of Treg subsets to varying input stimulations (**Fig 4.2b**). Both bulk and naïve Tregs exhibited comparable expansion across ICEp formulations, with 1% αCD3 and 2.67% αCD28 failing to expand over 1-fold, similar to the previously identified thresholds. Additionally, the response to αCD3 or αCD28 tended towards saturation at the highest levels. The overall expansion response tended to decrease with more differentiated subsets, with effector cells failing to expand except at the highest αCD3 or αCD28 formulations. Interestingly, the αCD3 and αCD28 threshold for expanding >1 for all donors increased by one titration step for memory (5% αCD3 and 8.33% αCD28) and two titration steps for effector (25% αCD3 and 25%-75% αCD28) compared to either bulk or naïve cells, highlighting the increased activation strength demands for increasingly differentiated subsets. These subset trends were also mirrored in the Dynabead-expanded comparison group (**Supplemental Fig. S4.3a**).

We next wanted to investigate whether the different Treg subsets enriched for different post-expansion phenotypes and whether this was modulated by the different ICEp formulations. We performed spectral flow cytometry profiling on expanded Treg subsets and pooled the live, CD4+, CD8-, Foxp3+, Helios+ gated cells across all samples for analysis. Following UMAP dimensionality reduction and visualization of marker heatmap projections, we observed that post-expansion Tregs compose of highly heterogenous states (**Fig. 4.2c**). To aid visualization between samples, we projected the subset-of-origin onto the UMAP and noted that the bulk Tregs were highly distributed across the phenotypic space with a high degree of overlap with the naïve samples (**Fig. 4.2d**). The regions of overlap between samples appeared to be correlated with regions that are mapped to expanding cells, defined by samples where the culture fold

expansion exceed 1-fold (**Supplemental Fig. 4.3b**). Effector cells, however, appeared to have the most distinct separation, including a region mapping to high HLA-DR, CD25, FoxP3 and low CD38. Due to these differences, we performed clustering of the spectral data to guide our downstream flow analysis and noted distinct phenotypic clusters, including one cluster (cluster 6) defined by low Foxp3, Helios, TIGIT, CCR7, TCF7, and CD25 and high in multiple effector Treg molecules such as CTLA-4, CD39, ICOS, HLA-DR (**Supplemental Fig. 4.3c**). This cluster was observed in ICEp and Dynabead samples that expanded, and had the highest enrichment from within the effector subset samples (**Supplemental Fig. 4.3b,d**). We then evaluated the purity of Foxp3+/Helios+ and emergence of FoxP3-/Helios- cells, noting the latter population was nearly absent from the naïve Treg population and was the prevalent within the effector subset (**Fig. 4.2e,f**). Interestingly, this double-negative population tended to increase with higher αCD3/αCD28 strength ICEps. In bulk and naïve Tregs, the Foxp3+/Helios+ population decreased with lower αCD3/αCD28 levels, whereas memory and effector subsets showed an increase under these conditions. Given that naïve cells exhibited the most significant expansion, the phenotypic maturation of bulk Tregs closely resembled that of the naïve group. This suggests that ICEp stimulation strength variably influences Treg subset expansion, with post-expansion cells tending to cluster according to their subset origin or expansion status.

We confirmed the memory differentiation results from **Fig 4.1e-g**, where bulk Tregs enrich for a CM phenotype, retain TCF7 expression, and return to a resting state—indicated by low HLA-DR expression (**Supplemental Fig. S4.5**). Treg memory differentiation appeared to follow a linear naïve-to-CM-to-effector differentiation path that was dependent on αCD3/αCD28 levels which induced proliferation[45]. At sub-proliferative levels, naïve Tregs retain a CD45RO-CCR7+ phenotype; memory Tregs differentiate towards an effector phenotype but, interestingly, can only maintain their CM pool at αCD3/αCD28 which induce proliferation; effectors retained their effector state although, similar to memory Tregs, a small pool of CM is maintained for

proliferative conditions. In the memory subset, the majority of cells expressed CCR7 at the time

of FACs purification, thus this emergence of effectors is likely due to differentiation rather than

outgrowth of CCR7- effectors (data not shown). Other than memory differentiation markers, we

noted that naïve Tregs tended to drop TCF7+ expression in high αCD3/αCD28 conditions and

maintain low HLA-DR expression, whereas effector Tregs maintain their TCF7+ expression at

high αCD3/αCD28 with a majority of cells retaining high HLA-DR+ expression at the end of

expansion. While HLA-DR+ tended to increase with additional αCD3 or αCD28—most evident in

the memory subset—its use as a stimulation marker is not clear here since low-expanding

memory Tregs enrich for CD45RO- CCR7- but have minimal HLA-DR expression, whereas low-

expanding effector cells retain high HLA-DR expression. Finally, using CD38 and CD39 as

markers for mature effector function, we noted that CM cells enriched from the naïve subset fail

to upregulate CD39 whereas activated memory and effector subsets upregulate both effector

molecules, with effector Tregs having the highest percent expression[17,46]. These findings are

largely in-line with the current dogma of Treg functional diversity, with naïve Tregs being the

most proliferative but least suppressive whereas effector cells are the most suppressive but are

less able to proliferate [47]. Since the bulk population failed to detect some phenotypic differences

across ICEp conditions, the investigation of Tregs with subset-level resolution enabled the study

of phenotypic maturation which informs our understanding about Treg differentiation,

maintenance of stemness related markers, and acquisition of effector function across

stimulation strengths.

D.3. Mapping heterogeneity of Tregs subsets using scRNAseq

Addressing the limited proliferative capacity of memory and effector Tregs under

ICEp stimulation, we aimed to identify Treg genomic features critical for expansion. The inherent

heterogeneity within Treg phenotypes during ICEp experiments prompted us to utilize

scRNAseq to explore this diversity and identify features correlating with expansion capacity.

While in vitro we were able to identify Treg subsets that had variable expansion magnitudes, there was a possibility that there is further proliferative heterogeneity within each subset. Recognizing that scRNAseq cannot be used to simultaneously track both the pre-and-post-expansion gene expression from an individual cell due to the destructive nature of the assay, we hypothesized that TCR clonality could serve as a marker for tracking the expansion and phenotypes of clonal populations. This hypothesis is guided under the assumption that cells of a given clonal group are more likely to be within the same phenotypic state—for example, expanding T cells will enrich for a more activated-phenotype and will be more numerous compared to unactivated, naïve cells. This approach would allow the TCR enrichment to act as a proxy for expansion and allows the comparison of transcriptomic profiles in an unexpanded population based off whether their TCR clonotype enriched or contracted after expansion. To this end, we divided FACs-purified bulk Tregs into three groups: 1) cells cryopreserved before activation 2) cells expanded by CD28 superagonist (CD28SA)—an activation reagent previously documented by our group to induce highly proliferative Tregs, and 3) cells expanded by Dynabeads. Expanded cells were tracked over 8-days and were assessed for Foxp3+/Helios+ purity prior to cryopreservation (**Supplemental Fig. S4.6**). Cells from all three experimental groups were later thawed, live-cell enriched, and processed for paired scRNA/TCRseq using the 10x Chromium platform (see Methods).

We first investigated the phenotypic landscape of the non-expanded Treg sample and attempted to identify the Treg subsets we previously sorted during ICEp experiments. After performing quality control—including removal of low-quality events, dead-cell and doublet removal, and sample integration to control for batch effects—we performed dimensionality reduction and clustering on the non-expanded Tregs (**Fig. 4.3a**, see Methods). We identified nine clusters corresponding to previously sorted subsets including naïve (NV), central memory (CM), and effector groups, with the latter composed of numerous subsets that correspond to the

extent of activation, differentiation, and acquisition of effector molecules, ranging from early

effector memory (EM) to late/terminal effectors (E-Late) (**Fig. 4.3c**). For cluster annotation, we

first looked at markers associated with Treg phenotype and proliferative capacity—such as

FOXP3, *IKZF2* encoding Helios, *CCR7*, and *TCF7* associated with naïve and CM or *HLA-DRB1*

and *ILR2,* encoding CD25, for activation—noting that there was polarization of activation and

naïve/CM markers that clustered them separately from the effector clusters (**Fig. 4.3b**). This

high-level separation prompted us to perform differential gene expression analysis between all

clusters (**Fig 4.3d**). Naïve and central memory cells were highly specific for markers regulating

stemness and repression of differentiation—including *TCF7*, *CCR7*, and *BACH2*—and minimal

expression of numerous activation and differentiation modules, including MHC-II associated

molecules (e.g *HLA-D* subtypes), *DUSP4*, *S100A10/A4*, *IL32*, *HPGD,* etc[48–53]. To further

distinguish their identities, we used a manually selected set of Treg-phenotyping genes,

including those encoding for Treg and T helper-like (Th-like) transcription factors, chemokine

receptors, surface effector molecules, cytokines, and intracellular signaling[8,9,13,38,39,42,44,54,55].

Relative to NV-1 and NV-2, CM upregulated *TIGIT*, *TNFRSF4* encoding OX40, *TNFRSF18*

encoding GITR, *IKZF2*, and *CD69*, indicating a relatively higher activation state and more recent

TCR-dependent activation (**Fig 4.3e** and **Supplemental Fig. S4.7a**)[56,57]. NV-1 and NV-2 were

highly similar, although NV-1 expressed higher *CD69*, *ICOS*, *PECAM1* and stemness-and-

survival factors such as *TCF7*, *MYC* and *BCL2*, indicating potentially more recent activation and

emigration from the thymus[58–61]. To distinguish effector groups, we first looked at the top

differentially expressed genes and noted that while they share many of these activation and

differentiation modules, a few select clusters expressed highly specific gene sets. Of these

groups, Effector Th-like (E-Th) was a low *Foxp3* expressing cluster which specifically

upregulated a group of genes reported in Th17 biology, including *RORC* encoding the Th17

transcription factor RORγ, *GPR25*, and *LMO4*[62,63]. E-Th also expressed genes for a variety of

cytokines which overlapped with multiple different Th-subsets, including *IL2, IL4, IL10, IL17A/F,*

and *IFNG*, prompting further subclustering to distinguish the heterogeneity in this cluster (**Supplemental Fig. S4.7a,c,d**). Subclustering E-Th revealed unique Th-like groups that were initially missed with the average cluster signature, including: subcluster 2 as Th2, expressing *GATA3, IL4, IL5,* and *IL13*; subcluster 3 as Th1, expressing *TBX21* and *IFNG*; and subcluster 4 as Th17 cells, expressing *RORC* and *IL17A/F*. Another cluster with a highly-specific gene set was Effector Interferon Response (E-IFN), which expressed numerous IFN-related genes, such as *IFIT1, IFIT3,* and *STAT1*, and was confirmed when running gene set enrichment analysis (GSEA) of all differentially expressed genes in this cluster, using the Reactome Database, showing high enrichment for Interferon Alpha/Beta and Gamma signaling pathways (**Fig. S4.3d** and **Supplemental Fig. S4.7a,b**). To distinguish the remaining effector groups, EM was associated with high expression of *TNFRSF4*, *TNFRSF18*, *TNFRSF1B* encoding TNFR2, *TIGIT*, and low *NFATC2*, which have collectively been associated with progenitor Tregs and maintenance of Treg memory pools[54,57,64]. The activated effector clusters, E-Act-1 and E-Act-2, were initially separated by relatively higher *CD69* expression in E-Act-1—indicating more recent TCR activation—and other markers of showing reduced differentiation and improved survival including slightly higher *TCF7*, *SELL*, *BCL2*, and lower *BAX*[59]. Compared to any other cluster, E-Act-2 had the highest expression of numerous activation and effector molecules, including high *FOXP3*, *IKZF2*, *HLA-DRB1/DRA*, *IL2RA*, *CTLA*-4, and *ENTPD1* encoding CD39, albeit at the expensive of low *TCF7*, *TIGIT*, *BCL2*, and high *CD226*—encoding DNAM-1—and *BAX*, features associated a shorter-lived, highly suppressive effector. The final effector group, termed Late Effector (E-Late), expresses Foxp3, HLA-DRB1/DRA, and DUSP4, similar to other effectors, but lacks many activation, effector, and survival molecules including *CD69, RORA, IL2RA, PDCD1* encoding PD-1*, ENTPD1, CTLA-4, ICOS*, and had the lowest *BCL2* expression of any cluster along with high *BAX*. While a Foxp3+/CD25lo Treg population has been associated with inflammatory conditions and even peripherally generated Tregs (pTreg), the absence of activation and effector molecules alongside the high ratio of *BAX:BCL2* may mark

this group as the end-state of the short-lived effectors with a pro-apoptotic potential[65,66].

Together, differential gene expression analysis, GSEA, manual gene selection, and cluster-sub-

clustering enabled the classification of different Treg subsets which reflect the populations and

maturation identified during ICEp activation of Treg subsets.

D.4. Identifying features of highly expanding Tregs using combined scRNA/TCRseq

Employing scTCRseq, we retroactively labeled clones based on their TCR clonotype

enrichment in either CD28SA or Dynabead conditions (see Methods). Here we focus primarily

on the CD28SA samples due to the higher number of TCRs detected from V(D)J sequencing

and the higher in vitro expansion compared to Dynabead, although this data is provided within

the **Supplemental Figures**. Analysis of post-expansion clonal enrichment revealed that highly

expanding clones become dominant and originate from rare, pre-expansion clones (**Fig. 4.4a**).

While the majority of abundant, pre-expansion cells were not detected in the CD28SA or

Dynabead samples, the sample-size was sufficient to capture a wide distribution of clones with

a defined TCR enrichment ratio (**Fig. 4.4b** and **Supplemental Figs. S4.8a,b,e-g**). By labeling

cells with their associated TCR enrichment ratio, we plotted enrichment distributions within Treg

transcriptomic clusters, summarizing cluster proportions by expansion fold bins (**Fig. 4.4c,d** and

Supplemental Fig. S4.8c,d, see Methods). Treg clones which contracted (<1 fold expansion)

were highly enriched for E-Act-1, E-Act-2, and E-Late whereas the more proliferative cells (>2

fold expansion) enrich NV-1, NV-2, CM, EM, and E-Th. Dynabeads also similarly enrich for

these clusters, although NV-1 and NV-2 are primarily found within the >4 high expansion

category (**Fig. S4.8c,d**). We proceeded to investigate the gene modules associated with each

expansion categories, finding that the highly expansive cells were low in *FOXP3* and high in

IKZF2, were associated with naïve/CM markers (i.e. *TIGIT*, *CCR7*, and *TCF7*), and tended to be

less activated (low *IL2RA*, *HLA-DRA/HLA-DRB1*, and *CD69*), which was expected due to the

relative enrichment from NV-1 and NV-2 (**Fig. 4.4e** and **Supplemental Fig. S4.9a**). Differential

gene expression analysis between expanding and contracting cells highlighted genes associated with proliferation and T-cell differentiation, with GSEA revealing distinct pathway enrichments between high expanders and contractors, notably an upregulation of cAMP degradation and regulation of WNT-signaling pathways as well as downregulation of cadherin-binding, actin remodeling, and cytokine signaling pathways (**Fig. 4.4f,g** and **Supplemental Fig. S4.9b,c**). Expectedly, numerous genes expected to correlate with proliferative capacity, such as *TCF7* and *CCR7*, were upregulated in expanders, as well as genes associated with repression of T-cell differentiation, *BACH2*, and mediators of RNA translation such as *EEF1G* and *EEF1B2*[67]. Genes predicted to be upregulated in contracting cells were associated with activation (*HLA-DRB1*, *S100A100*, *S100A4*), and effector differentiation and function (*DUSP4*, *PRDM1* encoding Blimp-1, *LGALS1* encoding Galectin-1). *AFF3,* a target of TCF7 and upregulated in expanding cells, has been implicated as an oncogenic driver in other cell types, promoting proliferation and reduction of apoptosis[68,69]. However, it has also been shown to be specific to naïve CD4+ T cells with the highest expression in naïve Tregs, with subsequent downregulation after activation and differentiation. Thus, further investigation into these markers is needed to identify genes that can be modulated for improving expansion versus those that are solely correlated with expansion potential and are driven by other master regulators. This analysis underscores the intricate relationship between TCR clonality, transcriptomic profiling, and Treg expansion, revealing specific gene expression patterns and signaling pathways may play pivotal roles in determining the proliferative capacities of Treg subsets.

E. DISCUSSION AND CONCLUSION

ICEp technology facilitated the controlled presentation of αCD3 to αCD28, enabling precise tuning to optimize the expansion of Tregs while maintaining Foxp3/Helios purity (**Fig. 4.1**). Maximal Treg expansion was dependent on relatively high αCD28 compared to αCD3, which additionally drove high Foxp3 expression and led to the highest enrichment of CD45RO+ CCR7+ CM cells. This high signaling demand is unsurprising, as multiple mechanisms have been reported to blunt Treg activation, including blunting of downstream TCR signals (e.g. PTEN, PKA-cAMP)[70–72]. Tconvs, however, were observed to have significant expansion at low αCD3, even capable of minor proliferation in absence of αCD28, albeit to a lesser extent than what is observed for CD8+ T cells activated without costimulation (data not shown)[73]. This differential capacity to expand with the lack of either signal drove us to explore the stimulation threshold for each activator. Our investigation revealed distinct αCD3 and αCD28 expansion thresholds for Tregs, which had been relatively unexplored in this cell type using engineered materials. Further, we observed a saturating response for both αCD3 and αCD28, most evident for bulk and naïve Tregs, which could not be overcome through increasing either antibody (**Fig. 4.2b**). Despite increased αCD3 and αCD28 being insufficient to drive memory and effector Treg proliferation, the identified expansion thresholds and level for saturation delineate the boundaries for further investigating Treg activation using this approach. We acknowledge that while memory differentiation was linked to expansion, sub-mitogenic cues may still mediate survival and other effector functions—a distinction which should be further investigated for modulating Treg activity, either in vitro or in vivo[9,74–77].

Treg subsets displayed differential expansion responses, with the majority of the bulk Treg response deriving from the highly proliferative naïve subset, as determined by similar expansion-folds and enrichment for similar post-expansion phenotypes. Further, the naïve subset gave rise to Foxp3+/Helios+ pure cells across ICEp formulations, whereas the poorly

expanding effector subset generated the highest proportion of Foxp3-/Helios- cells with the most stimulating ICEps. Clinical protocols that enrich for CD45RA+ Tregs before expansion may sidestep issues identified in subsets less amenable to expansion[86–88]. However, the challenges faced in the ARTEMIS trial highlight the necessity of a more sophisticated approach, especially given the likely predominance of CD45RO+ cells in patient samples which may be enriched for the allo-reactive Tregs required for the ARTEMIS trial. This insight compels further exploration into strategies for enhancing expansion in CD45RO+ memory and effector Tregs, potentially broadening the applicability of Treg therapies.

It is worth noting that Dynabeads frequently outperformed ICEp in expansion—with an additional 1-2 days of expansion before resting relative to ICEp (**Supplemental Fig. 4.3a**). T cell activation is well-orchestrated process that leads to various cytoskeletal rearrangements and organelle trafficking to polarize towards this synapse[78,79]. Here, Dynabeads are provided 1x bead:cell excess, thus a cell is more likely to form a singular synapse with one bead, whereas in the ICEp case we give 9x excess, potentially leading to multiple regions of activation. While increasing ICEp number initially improves expansion, it is possible that this effect is diminished with additional particles due to the lack of a primary immunological synapse. Unlike for Tregs, the relatively smaller ICEp has been shown here to achieve similar Tconv expansions compared to Dynabeads, potentially due to the observed reduction in activation demands required to achieve maximal expansion. There are multiple ICEp parameters which can be further investigated for improving Treg expansion, such as increasing the particle diameter and number, use alternative costimulatory ligands, and presentation or release of immunomodulatory agents such as IL-2[60,80–85].

Through paired scRNA/TCRseq, we delved into the heterogeneity of Treg subsets, identifying distinct populations with differential features corresponding to stemness, survival, proliferation, and effector function. We identified numerous Treg subsets which resembled the

phenotypes that we sorted for subset activation with ICEp. However, numerous assumptions on Treg differentiation—such as the acquisition of effector molecules and the dynamic gain and loss of activation markers—were applied to these groups based off of our in vitro expansion data, which may not reflect the same Treg in vivo fates. To further gain confidence in these annotation labels and their state transformations, RNA-velocity can be performed[89]. Further, we can apply these methods or CITE-seq to specifically track CD45RA/RO isoforms to better align identified clusters with our FACs purified subsets[90,91]. Regardless of the differentiation path, we identified effector Treg clusters with unique cytokine and transcriptional profiles, raising questions about their stability and role in immune regulation. Of these, the high-cytokine producing Th-like group, E-Th, expressed relatively high Th17 and Th1 programs. While Th-like Tregs have been purported to play a physiological role in immune tolerance due to their capacity to migrate into specific Th-promoting inflammatory sites (e.g. CXCR3/CCR5 for Th1, CCR6 for Th17), this cluster was found to be a low expressor of both *Foxp3* and *IKZF2* which is concerning for Treg identity destabilization (**Fig. 4.3e** and **Supplemental Fig. S4.7a**)[8,92–94]. Interestingly, these cells were high expressors of *LIMS1*, which has been reported to be expressed in a subpopulation of Foxp3+ Tregs which, upon stimulation, were highly proliferative but were a main source of Foxp3-/Helios- cells[13]. While *LIMS1* encodes an intracellular marker—preventing its used for FACs removal—its expression was found specifically in Tregs expressing low *SELL*, *CCR7*, and *TIGIT*, which is also minimally expressed in the E-Th cluster. Additionally, *CD40LG* was highly expressed in *LIMS1* expressors, although naïve, thymically derived Tregs may also express this, albeit with specifically high *CCR7* and *SELL* expression[13,92,95]. Thus, future work could use such differentially expressed markers to selectively deplete the *LIMS1* expressing E-Th cells without depleting naïve Tregs. Additional work is needed to confirm the protein-expression correlations with any markers identified within this study. Another possibility for this E-Th population is that they could be Tconv impurities from FACs. However, these cells express numerous markers associated with Treg effector function,

130

including *PDCD1*, *HAVCR1* encoding TIM-3, *CD38*, and *TGFB1*. While these may also be expressed on activated or exhausted Tconv cells, we would expect that in the bulk culture these reportedly slow-growing cells would be outnumbered and further suppressed by the rapidly dividing Tregs[96,97]. Since their fraction remains consistent across ICEp conditions, it is more likely that the Foxp3-/Helios- population is emerging from a Treg source rather than a rapidly dividing Tconv source. Further investigation into these subpopulations via FACs purification is needed to confirm their identity and fate.

The application of TCR enrichment for cell expansion labeling successfully identified Tregs with high proliferative potential, predominantly enriching for naïve and CM groups as anticipated from our in vitro ICEp experiments. Unexpectedly, we observed proliferation from EM groups, which may imply that the minimal in vitro expansion observed in effector subset may be due to the EM dilution within multiple poor expanding effector subgroups, such as the activated effector groups. Across all high expanding Tregs, differential gene expression identified a distinct transcriptional profile, notably the upregulation of cAMP-degrading enzyme genes such as *PDE4D* (**Fig. 4.4f,g**). Given cAMP's critical role in mediating Treg suppressive functions—where Tregs inherently exhibit elevated levels due to increased adenylate cyclase activity and decreased PDE activity—this finding warranted further investigation for modulating expansion[72,98,99]. Upon revisiting the intracellular signaling gene module, we observed that, in contrast to the highly expanding Tregs, the contracting cells exhibit elevated expression for T cell relevant adenylate cyclases (*ADC3/7/9*) and Gs-GPCRs such as *PTGER2* and *ADORA2A*—encoding Prostaglandin E Receptor 2 and Adenosine A2A Receptor, whose activation leads to cAMP production (**Supplemental Fig. 4.9a**)[99,100]. Interestingly, the ligands for these receptors, PGE2 and Adenosine, are synthesized by effector Tregs through the upregulation of COX-2 and the CD38/CD39/CD73 axis, respectively. Additionally, the highly suppressive metabolite of PGE2, 15-keto PGE2, is produced via HPGD, whose expression was

also specific for effectors and highly contracting cells. Regarding the observed effect of minimal memory/effector proliferation except at high αCD3/αCD28, it is hypothesized that cAMP may attenuate TCR signaling through LCK phosphorylation by Protein Kinase A which is anchored to the cell membrane by Ezrin—whose expression was markedly upregulated in contracting cells[72]. This mechanism, if validated, could explain the observed resistance to αCD3 and αCD28 ICEps except at the highest stimulation strengths. As a therapeutic target, transient inhibition of adenylate cyclases in Tregs has been shown to improve proliferation in bulk Treg, albeit temporarily compromising their suppressive function which recovers after expansion[101]. Among the PDE4 forms, PDE4D has been shown to be required for CD4+ Tconv proliferation, while PDE4A/B/C are more closely linked to effector functions[102]. Our data reflect a similar dichotomy for Tregs, with *PDE4A/B/C* predominantly expressed in contracting cells, whereas *PDE4D* is upregulated in expanding cells. Exploring inducible but transient *PDE4D* expression could offer a novel method to toggle between proliferation and effector functions in Tregs. If validated, this should prompt an investigation into effector Treg self-suppressive mechanisms and which ones Tregs naturally are able to escape. While identifying potential targets for enhancing effector Treg expansion, it's imperative to proceed with caution due to the trade-off between proliferation and immunosuppression. The identification of the cytokine producing E-Th group within the expanding TCR pool underscores this balance, highlighting the need for further research to understand if the effector Treg population intrinsically limits the growth of unstable Tregs and whether enhancing proliferation risks compromising suppressive capabilities and Treg purity. Future studies will delve into cAMP modulation across the effector Treg pool and specific subpopulations, aiming to mitigate the influence of potentially destabilizing groups.

A notable limitation of our TCR enrichment strategy as a proxy for expansion is that the most highly expanding cells originate from rare pre-expansion clones, leading to sampling difficulties. Based on the expansion curves for Dynabead and CD28SA samples, the mean

132

expansion of cells detected via TCR analysis should have approached 26.4 and 69.6, respectively, although from the majority of cells fall below these values. This discrepancy suggests that a significant portion of cells contributing to overall expansion could not be labeled due to their rarity and sampling limitations. Although some of these cells are likely represented in our transcriptomic dataset, distinguishing them from less proliferative, more abundant cells poses a challenge for future analysis.

In conclusion, this study not only advances our understanding of Treg biology and manufacturing challenges but also opens new avenues for optimizing Treg therapy through strategic manipulation of expansion and effector mechanisms. Future work is geared towards investigating isolation methods for potential destabilizing Tregs, validating the protein expression of target genes associated with highly expanding Tregs, modulating identified pathways/targets in Treg subsets to improve expansion, and—if the targets successfully promote proliferation—closing-the-loop with ICEps to verify whether the target modulation acts through modified TCR/costimulation sensitivity and whether ICEps can be fine-tuned to promote proliferation without incurring destabilization. This study has opened numerous exciting paths in Treg biology and cell therapy, and advancing these insights into research and clinical manufacturing pipelines may provide a means to reestablish the potential for Treg therapy for patients in need.
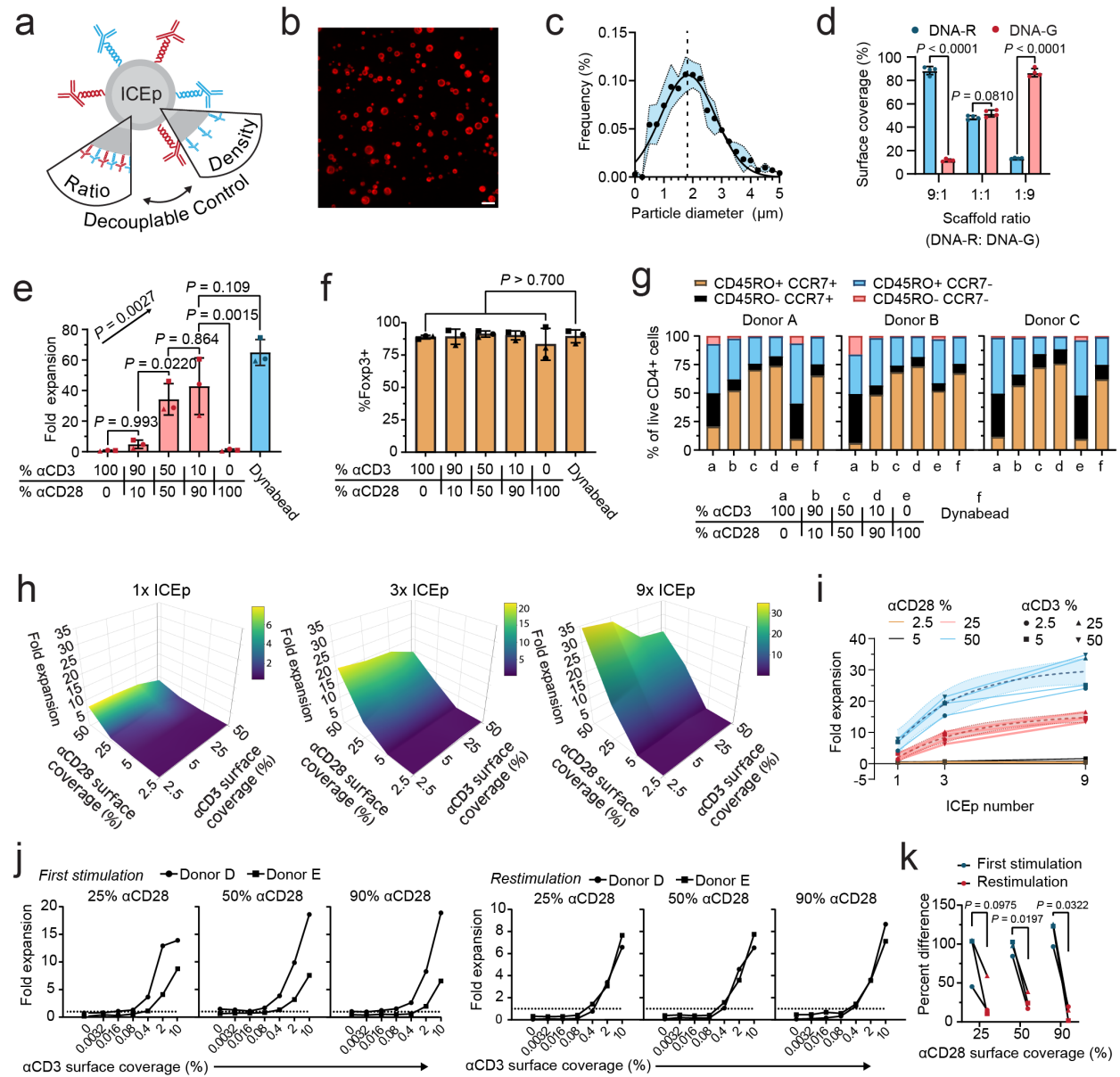
F. FIGURES

Figure 4.1. Optimization of ICEp activation parameters to maximize T cell expansion.

(a), Diagram of ICEp highlighting the ability to independently control the ratio and density of surface-hybridized biomolecules between ICEp formulations. (b), Representative confocal microscopy image (40x magnification) of 2 μm diameter particles hybridized with 5'-Cy3-labeled compDNA-R. Scale bar, 10 μm. (c), Representative size distribution of 2 μm particles from b, mean diameter 1.84 μm (represented as vertical dashed line) and s.d. 0.935 as determined by gaussian distribution fit of n = 3 independent fabrication samples (adjusted R^2 = 0.921, room mean square error (RMSE) = 0.0101).

(Figure caption continued on the next page.)

(Figure caption continued from the previous page.)

Shaded envelope represents ±1 s.d. for each frequency bin across samples. (d), Verification of scaffold DNA ratios via detection of hybridized 5-FITC compDNA-R and 5'-Quasar705 compDNA-G, normalized to total loading capacity of both compDNAs across n = 4 technical replicates. P values were determined using multiple two-tailed unpaired t-tests with Holm-Šídák correction. (e), Fold expansion of Tregs at day 8 post-stimulation using ICEp (4x excess ICEp to cells) across varying surface-hybridized αCD3 and αCD28. Inter-ICEp P values were determined by one-way ANOVA ($F_{5,12}$ = 24.29, P < 0.0001) followed by Tukey's post hoc test and a linear trend was determined using one-way ANOVA ($F_{3,8}$ = 11.65, P = 0.0027). Data point markers: circle = Donor A, square = Donor B, triangle = Donor C. (f), Percentage of Foxp3 expressing cells among live CD4+ gated Tregs (see **Supplemental Fig. S4.2a** for gating strategy) from e. P values (marked by the lower bound of all P values) comparing ICEp conditions to commercial Dynabead control was determined using one-way ANOVA ($F_{1.403,2.807}$ = 0.846, P = 0.4739) followed by Dunnet's post hoc test. (g), Memory differentiation phenotype of live CD4+ gated Tregs from e. (h), Surface plots of Treg fold expansion after 8 days post-activation with ICEps across varied ICEp amounts (excess ICEP to Tregs) and surface titrations of αCD3 and αCD28. (i), Treg expansion response from h as a function of ICEp number and αCD28. Growth curves for 25 and 50% αCD28 were fit using exponential plateau: ((adjusted R^2, RMSE$)$: 25% αCD28 (0.940, 1.250); 50% αCD28 (0.870, 3.348)) where the dashed lines correspond to the fit and the shaded envelope represents the 95% confidence interval. 2.5 and 5% αCD28 were not plotted due to fit instability and overlap with X-axis. (j), Left: expansion fold of Treg at day 10 post-first stimulation using ICEp (9x excess ICEp to cells) with a fixed αCD28 surface coverage (25, 50, or 90%) and varying αCD3 levels. Right: Subsequent fold expansion of Tregs 8 days after restimulation of Dynabead-expanded cells using ICEps (9x excess ICEp to cells; restimulation on day 10 post-first stimulation). The dotted-line represents 1-fold expansion, and unique data points markers represent individual donors. (k), Fold expansion percent difference (to the mean) between donors in j at αCD3 levels that initiated expansion, comparing between first stimulation and restimulation. Data point markers indicate the αCD3 surface coverage used for calculation: circle = 0.4%, square = 2%, triangle = 10%. P values were determined using multiple two-tailed paired t-tests with Holm-Šídák correction. Data in b represent n = 4 technical replicates, e, f, g represent n = 3 donors, h, i represent n = 1 donor, j, k represents n = 2 donors. Error bars in b represents ± s.e.m., e, f represents ± s.d.
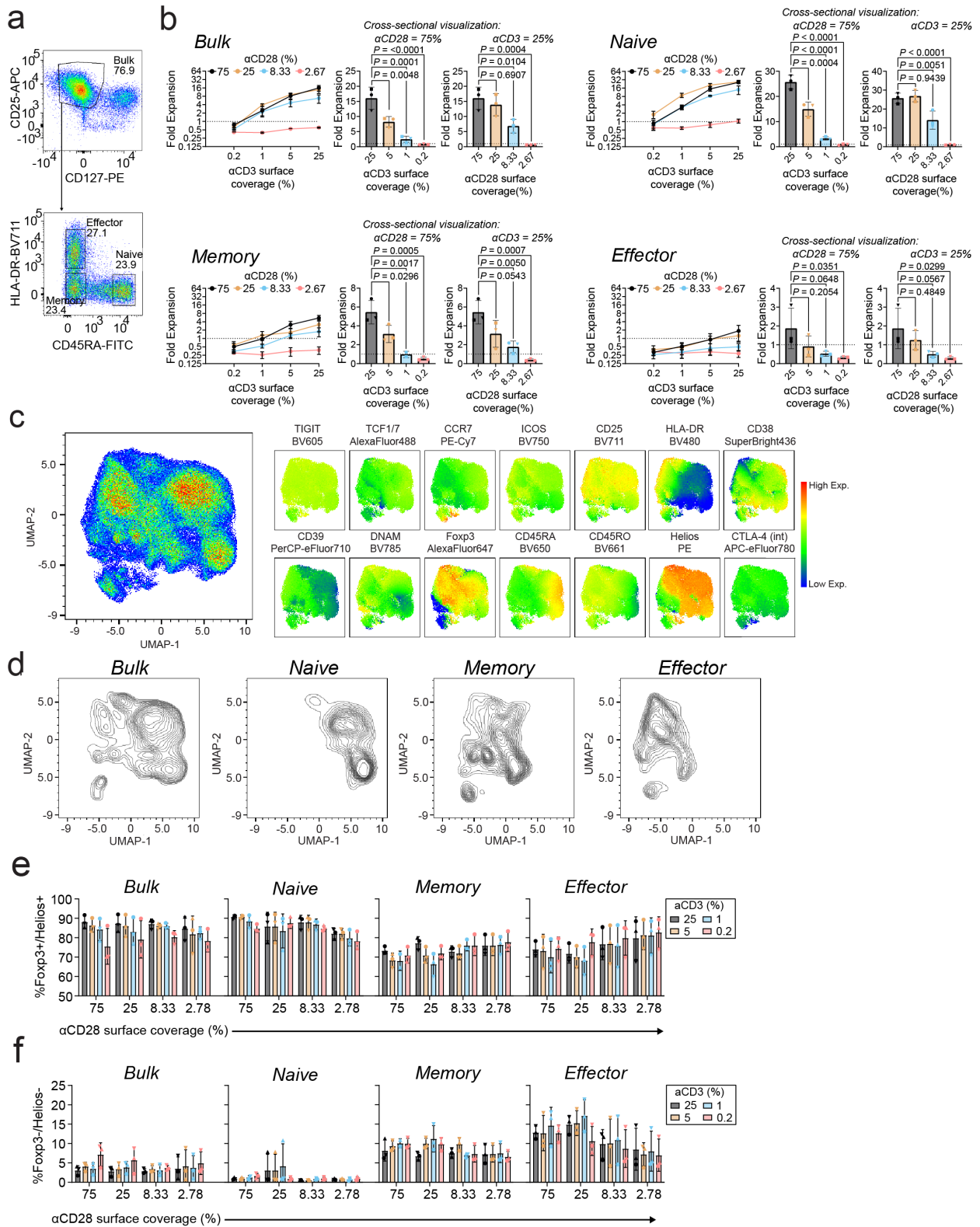
Figure 4.2. Treg subsets display differential expansion and distinct post-expansion fates.

(Figure caption continued on the next page.)

(Figure caption continued from the previous page.)

(a), Representative FACs sorting gates for bulk (CD4+, CD25hi, CD127-) Treg and further subsets of naive (CD45RA+, HLA-DR-), memory (CD45RA-, HLA-DR-), and effector (CD45RA-, HLA-DR+). (b), Left: fold expansion of Treg subsets on day 8 post-ICEp activation (6x excess of ICEp to cells) under varying αCD3 and αCD28 ICEp surface coverage (left). Middle: Expansion dose-response to αCD3 at maximum αCD28 coverage (75%). Right: Expansion dose-response to αCD28 at maximum αCD3 coverage (25%). *P* values were determined by one-way ANOVA followed by Tukey's post hoc test. Dotted-line represents 1-fold expansion. Individual donor data are represented by unique markers (Donors F-H for circle, square, and triangle, respectively). (c), Left: Spectral flow analysis of pooled data across all data in c. Right: Heatmap projections of markers onto UMAP using down-sampling (n=2000 cells per condition) gated by live, CD4+, CD8- cells. (d), Visualization of samples from each subset culture in c. €, Percentage of Foxp3 and Helios expressing cells among live CD4+ gated Tregs (see **Supplemental Fig. S4.4a** for gating strategy) from e across subsets and ICEp conditions. (f), Percentage of Foxp3 and Helios non-expressing cells among live CD4+ gated Tregs from e across subsets and ICEp conditions. Data in b, e, and f represent mean ± s.d. of *n* = 3 independent donors.
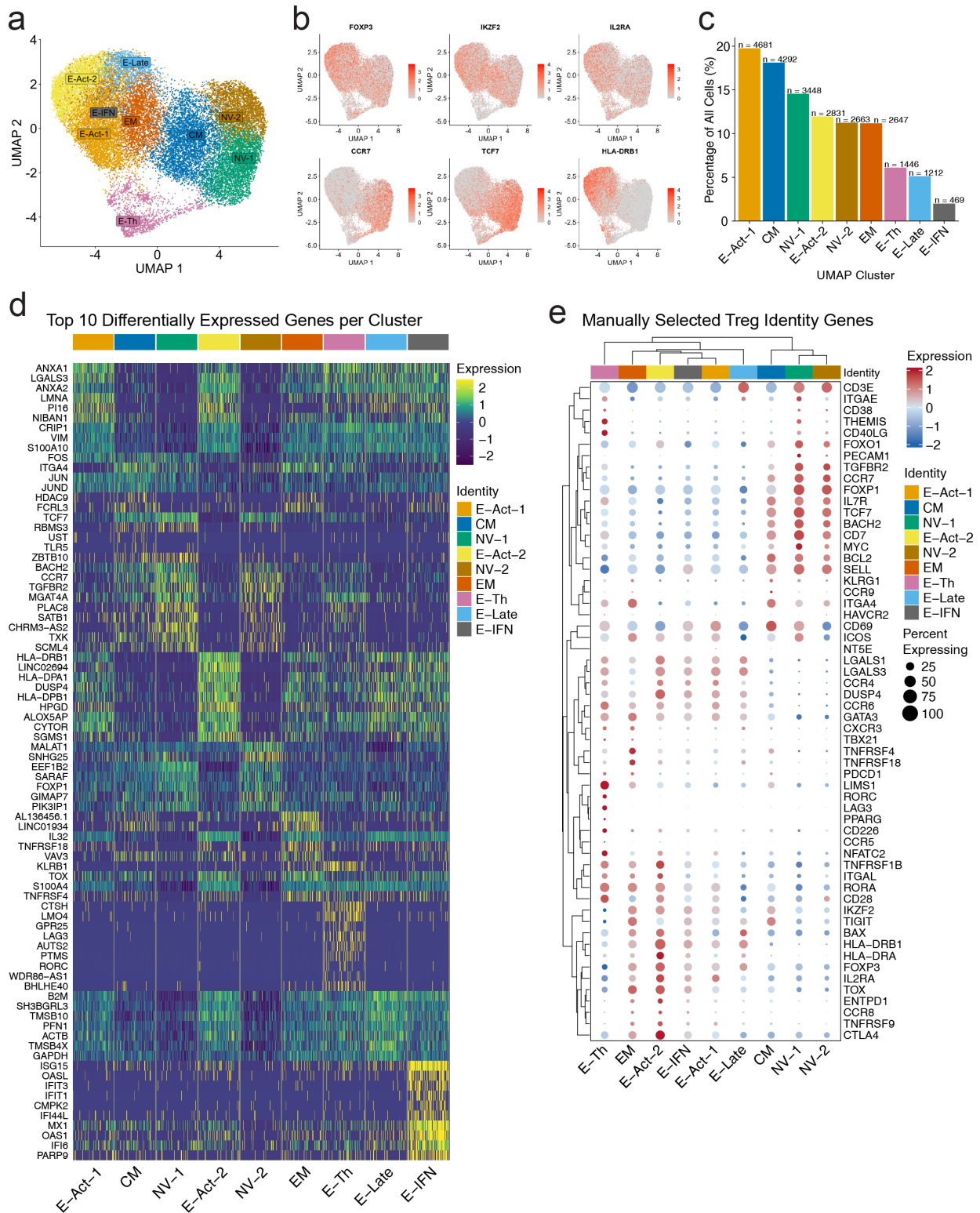
Figure 4.3. scRNAseq of reveals heterogenous Treg states.

(Figure caption continued on the next page.)

(Figure caption continued from the previous page.)

(a), UMAP visualization of Treg single-cell transcriptome, with clusters identified and labeled using custom-defined identities (NV = Naïve, CM = Central Memory, EM = Effector Memory, E-Act = Effector Activated, E-Late = Effector Late, E-IFN = Effector Interferon Responsive, E-Th = Effector Th-Like. (b), UMAP projections highlighting the spatial distribution of marker expression, delineating distinct Treg states. *n* indicates the total number of cells within each cluster. (c), Proportion of all cells contained within each cluster. (d), Heatmap of the top 10 differentially expressed genes between all identified Treg clusters. (e), Dot plot representation of selected Treg-phenotyping genes for further classification of cluster identities, with further clustering within both genes and identity cluster. Dot expression represents average normalized expression, and the dot size is proportional to the percentage of cells within an identity cluster that express the given marker.
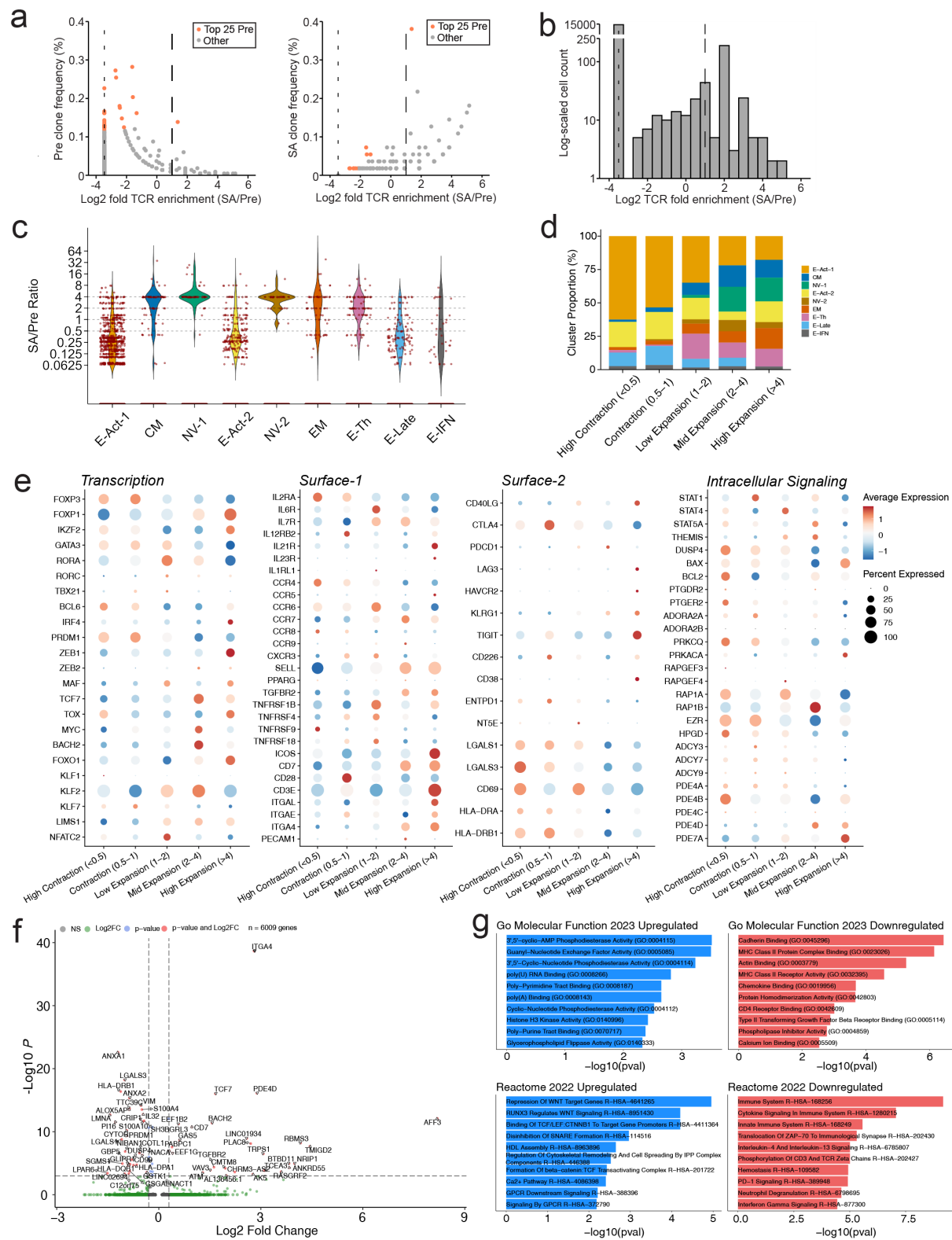
Figure 4.4. Paired scRNAseq and scTCRseq enables tracing of expanding Tregs.

(Figure caption continued on the next page.)

(Figure caption continued from the previous page.)

(a), Frequency distribution of TCR clones before (Pre, Left) and after expansion with CD28SA (SA, Right), plotted against log2 fold enrichment ratio (TCR clone frequency SA versus Pre). Markers represent unique clonal groups identified by paired α-and-β VJ segments, with top 25 most frequent pre-expansion clones highlighted. Dotted line at x=-3.5 indicates clones absent in SA TCR pool; dashed line at x=1 marks the two-fold expansion threshold. (b), Count distribution of all TCR clones identified in a, linear scale values: mean = 3.793 (Log2=1.923) and s.d. = 3.938 (Log2 = 1.977). (c), Violin plots of SA/Pre enrichment ratios for Treg identity clusters, with individual cells represented by markers. Cells at x=0 were not found in the SA TCR pool. Dashed lines at x=0.5, 1, 2, and 4 indicate expansion category thresholds. (d), Enrichment of Treg identity clusters within SA/Pre TCR enrichment categories shown in c. (e), Dot plot representations of phenotypic modules used investigate expansion categories. (f), Volcano plots of differentially expressed genes between SA-expanded cells with >2 fold enrichment and those contracted to <1 fold, with log2 fold change (vertical dashed line) threshold at ±0.3 and adjusted *P* value cutoff of 0.001 (-Log10 = 3, horizontal dashed line). (g), Pathway analysis of differentially expressed genes in f using the Go Molecular Function 2023 (Top) and Reactome 2022 (Bottom), comparing pathways upregulated in expanders (>2 fold, left) versus pathways upregulated in contractors (<1 fold, right).
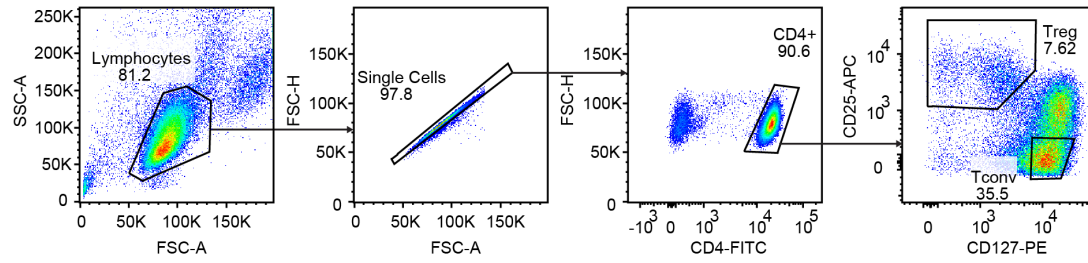
Supplemental Figure S4.1. FACs gating strategy for isolating CD4+ Tconvs and CD4+ Tregs using CD4+ negative selection kits.

FACs gating for isolating Tregs and Tconvs used in **Fig. 4.1** using a CD4+ negative enrichment kit.
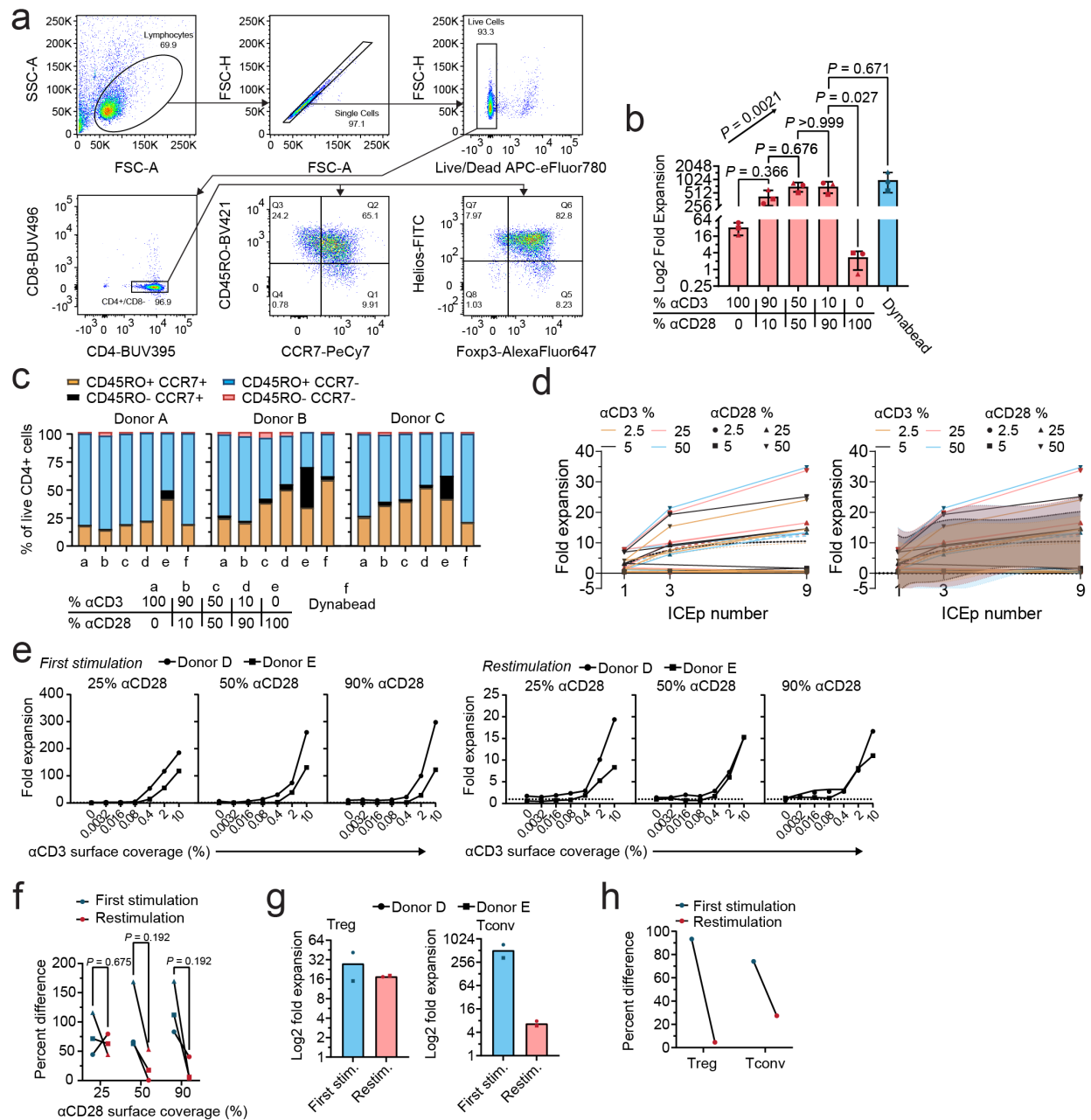
Supplemental Figure S4.2. Optimization of ICEp for general T cell activation and phenotyping.

(a), Representative flow cytometry gating for phenotyping T cells used in **Fig 4.1**. (b), Log2 fold expansion of Tconvs at day 8 post-stimulation using ICEp (4x excess ICEp to cells) across varying surface-hybridized αCD3 and αCD28. Inter-ICEp *P* values were determined by one-way ANOVA ($F_{5,12}$ = 8.850, *P* = 0.0010) followed by Tukey's post hoc test and a linear trend was determined using one-way ANOVA ($F_{3,8}$ = 12.61, *P* = 0.0021). Data point markers represent Donors A-C for circle, square, and triangle, respectively. (c), Memory differentiation phenotype of live CD4+ Tconvs from b. (d), Left: Treg expansion response from **Fig 4.1h** as a function of ICEp number and αCD3.

(Figure caption continued on the next page.)

(Figure caption continued from the previous page.)

Growth curves for 2.5, 5, 25, and 50 αCD28 were fit using exponential plateau (dashed lines): ((adjusted R^2, RMSE): 2.5% αCD28(0.1981, 7.107); 5% αCD28(0.1532, 7.818); 25% αCD28 (0.1668,9.753); 50% αCD28 (0.1447, 10.10)). Right: similar plot to left including the fit and the shaded envelope represents the 95% confidence interval. (e), Left: expansion fold of Tconv at day 10 post-first stimulation using ICEp (9x excess ICEp to cells) with a fixed αCD28 surface coverage (25, 50, or 90%) and varying αCD3 levels. Right: Subsequent fold expansion of Tconv 8 days after restimulation of Dynabead-expanded cells using ICEps (9x excess ICEp to cells; restimulation on day 10 post-first stimulation). The dotted-line represents 1-fold expansion, and unique data points markers represent individual donors. (f), Fold expansion percent difference (to the mean) between donors in e at αCD3 levels that initiated expansion, comparing between first stimulation and restimulation. Data point markers indicate the αCD3 surface coverage used for calculation: circle = 0.4%, square = 2%, triangle = 10%. P values were determined using multiple two-tailed paired t-tests with Holm-Šídák correction. (g), Left: Dynabead expansion response for Tregs in **Fig 4.1j** after first stimulation and restimulation using Dynabeads. Right: Dynabead expansion response for Tconvs from e. (h), Dynabead fold expansion percent difference (to the mean) between donors for Treg and Tconv. Data in b, c represent $n = 3$ donors, d represent $n = 1$ donor, e-h represent $n = 2$ donor. Error bars in b represent ± s.d.
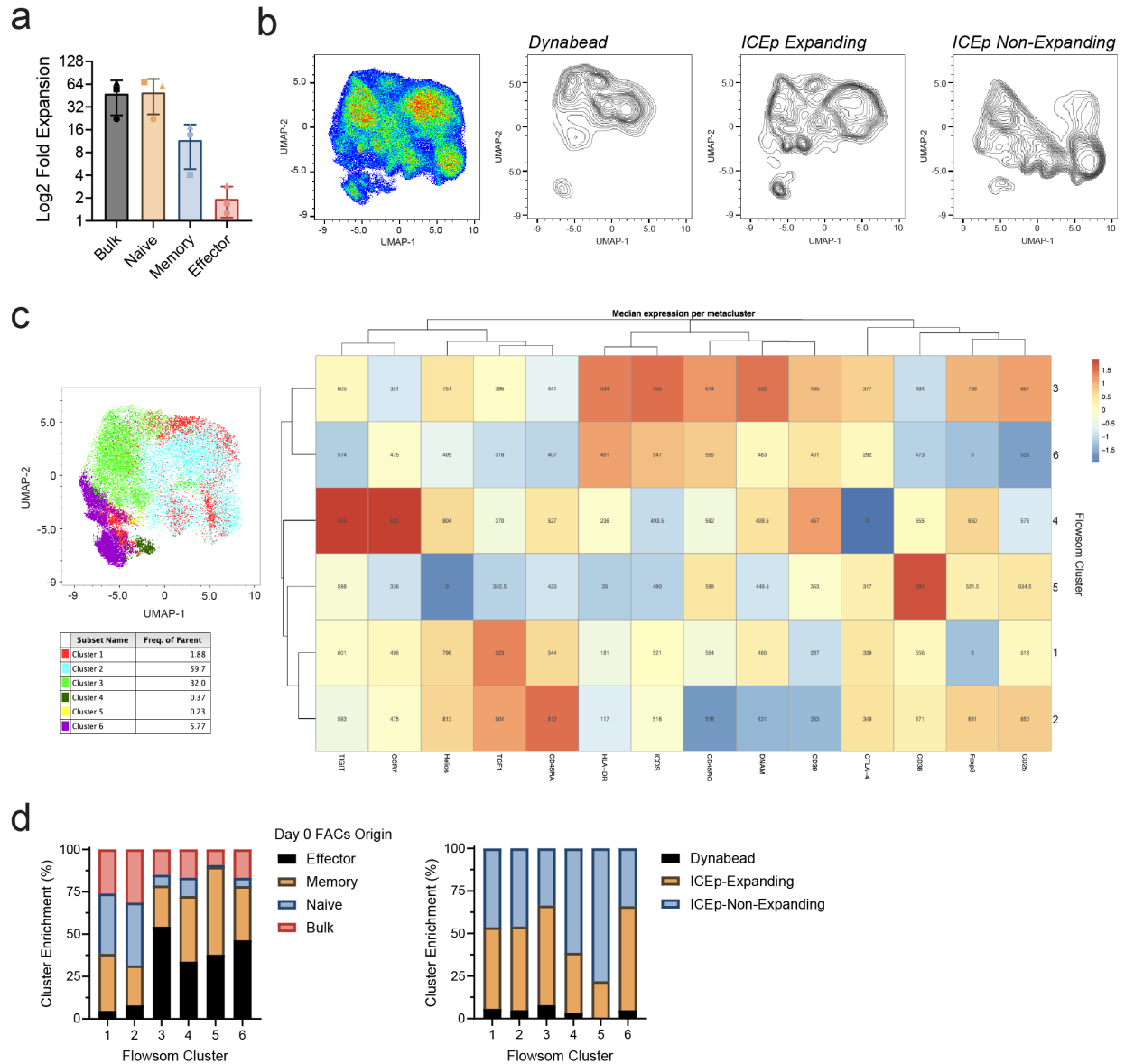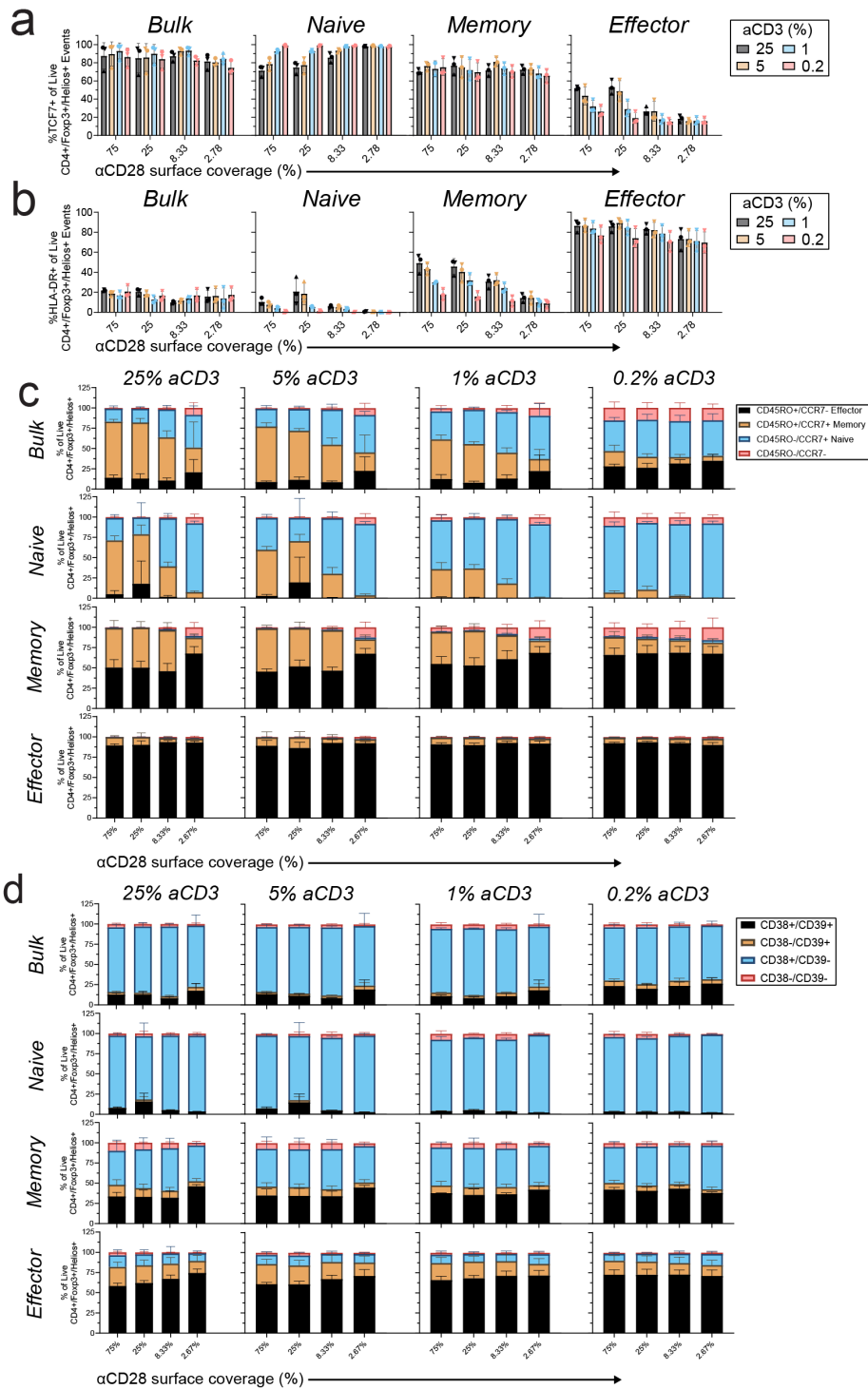
Supplemental Figure S4.3. Phenotypic analysis of expanded Treg subsets indicates differential enrichment based on origin and expansion status.

(a), Fold expansion of Dynabead-activated Treg subsets from **Fig. 4.2** measured at Day 8 (1x excess Dynabead to cell). Data point markers represent Donors F-H for circle, square, and triangle, respectively. (b), Left: UMAP representation of spectral flow cytometry data from **Fig 4.2c**. Right: visualization of samples from either Dynabead or ICEp grouped by expansion status (expanding: >1 fold at day 8 and non-expanding: <1 fold at day 8). (c), Left: Projection of cell clusters onto the spectral flow UMAP. Right: heatmap of marker expression within cell clusters with further hierarchical clustering by marker (normalized expression within each channel). (d), Left: cluster enrichment by Treg subset samples. Right: cluster enrichment by either Dynabead or ICEP samples grouped by expansion status defined in b.
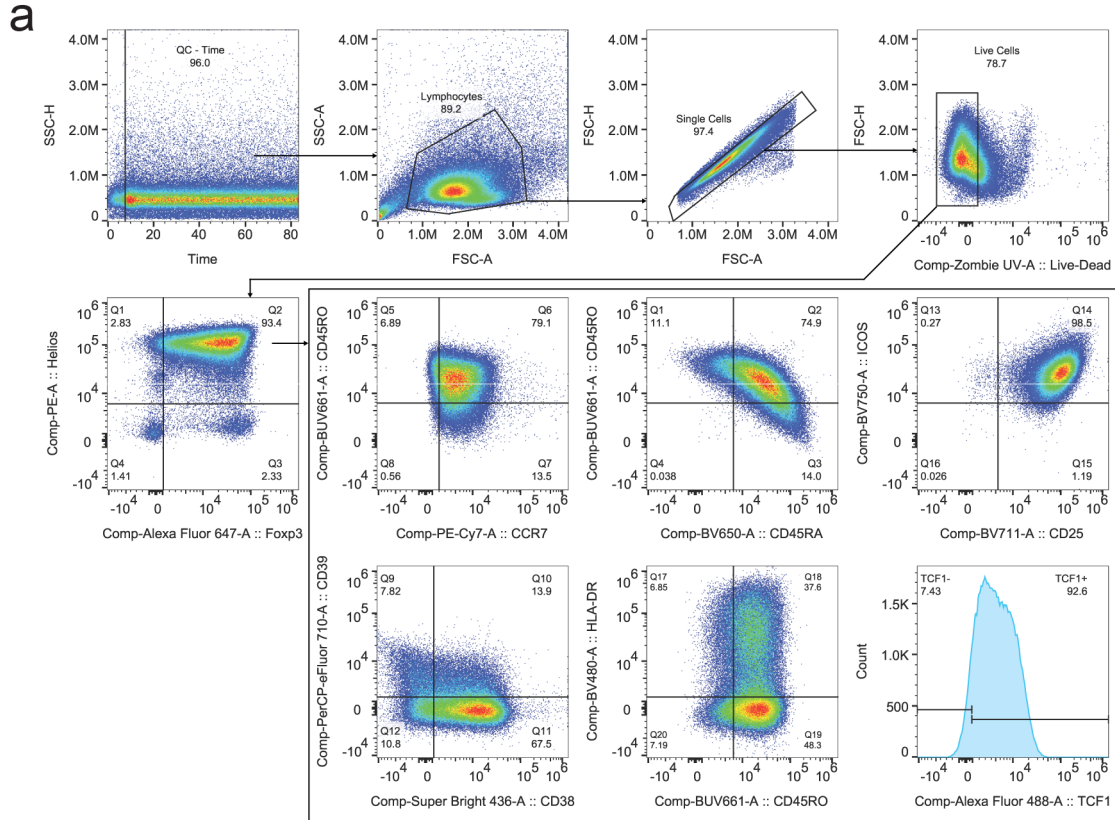
Supplemental Figure S4.4. Spectral flow cytometry gating strategy for post-expansion Treg subset phenotyping.

Flow cytometry gating used for analysis in **Fig 4.2** using Dynabead-expanded cells. Initial gating was performed using a time-gate for quality controlling early MFI-fluctuations before cytometer stabilization. Subsequent gates were established based on fluorescence-minus-one (FMO) controls to define cell populations.
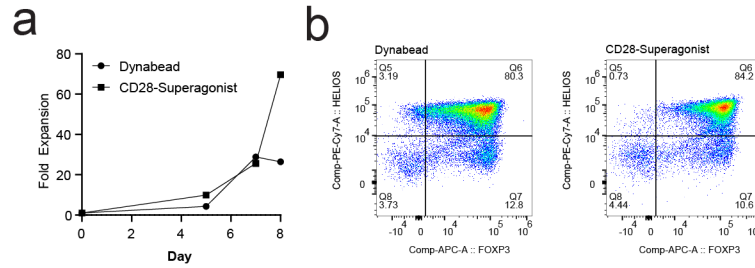
Supplemental Figure S4.5. Post-expansion phenotyping of Treg subsets.

Data here accompanies **Fig. 4.2** for FACs purified Treg subsets activated for 8 days with either ICEp or Dynabead. All data derive from live, CD4+, Foxp3+, Helios+ Treg gates using the strategy defined in **Supplemental Fig. S4.4**.

(Figure caption continued on the next page.)

(Figure caption continued from the previous page.)

(a), Quantification of TCF7+ cells (b), Quantification of HLA-DR+ cells. (c), Quantification of memory differentiation phenotypes, including naïve (CD45RO-, CCR7+), memory (CD45RO+, CCR7+), effector (CD45RO+, CCR7-), and a phenotype of unknown significance (CD45RO- CCR7-). (d), Quantification of CD38/CD39 phenotypes. Data in a-d, represent mean ± s.d. of n = 3 independent donors.

Supplemental Figure S4.6. Purity assessment for expanded Tregs used in paired scRNA/TCRseq.

(a), Expansion fold over-time for FACs purified bulk Tregs expanded using either Dynabeads or CD28 superagonist. (b), Flow cytometry plots to quantify Treg purity via Foxp3+/Helios+ at day 8 post-activation using either Dynabead (left) or CD28 superagonist (right).
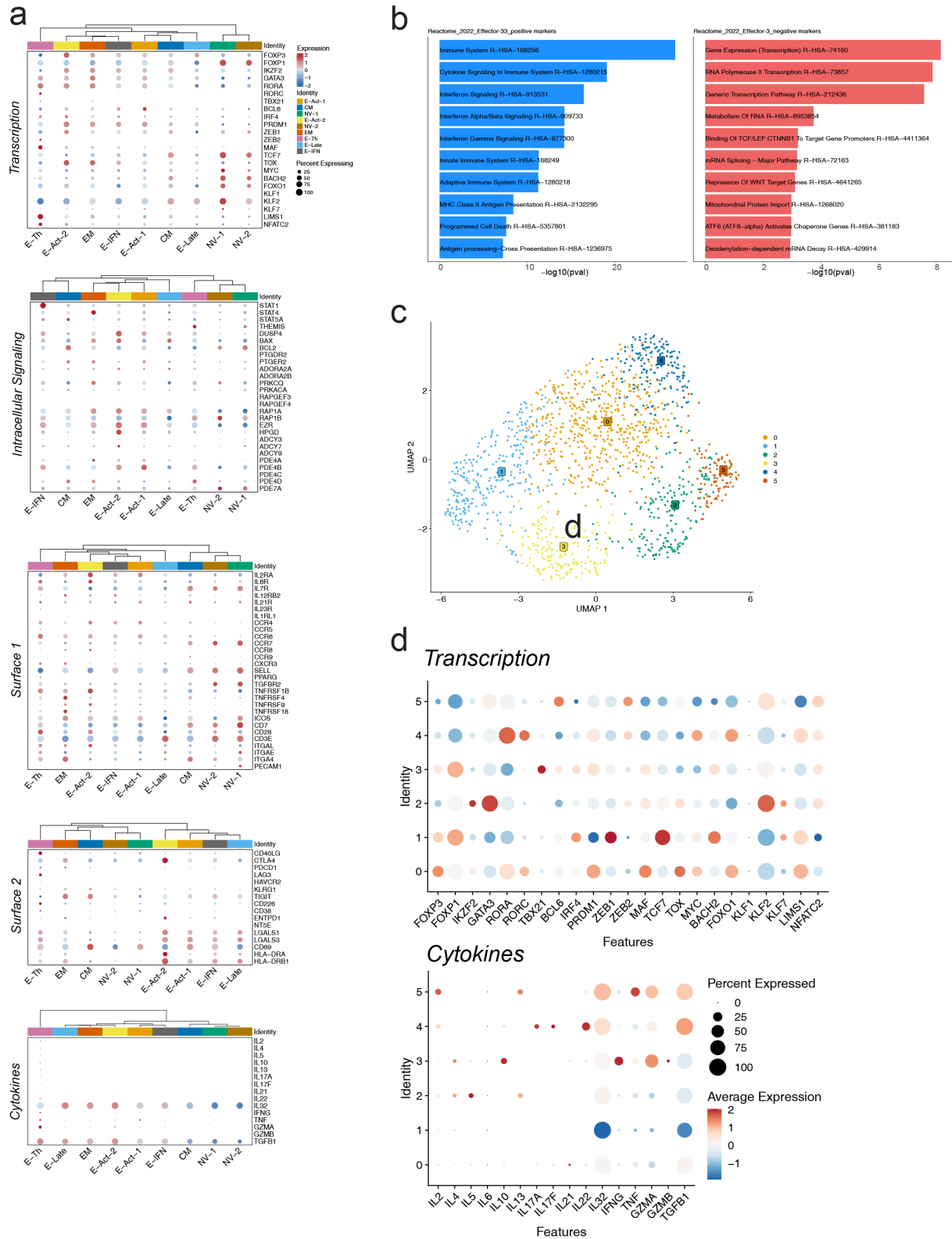
Supplemental Figure S4.7. Transcriptomic analysis identifies unique Treg cluster identities. (Figure caption continued on the next page.)
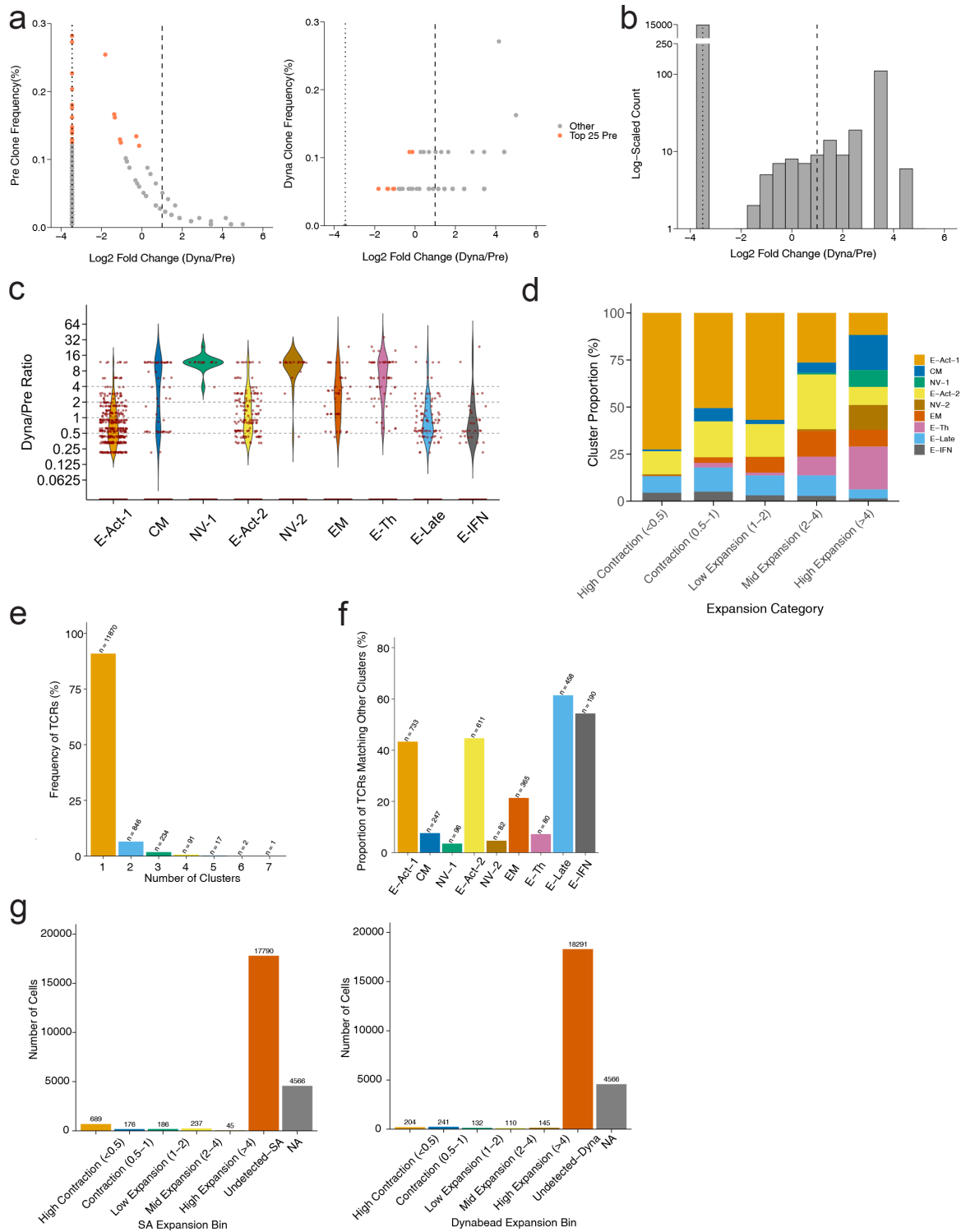
(Figure caption continued from the previous page.)

(a), Dot plot representation of selected gene modules across different Treg identity clusters with further clustering on identity based on gene expression. (b), Pathway analysis of differentially expressed genes within the E-IFN (Effector Interferon Responsive) cluster, using the Reactome 2022 database. Left: upregulated pathways within E-IFN compared to all other identities. Right: Downregulated pathways within E-IFN compared to all other identities. (c), UMAP representation of sub-clustering E-Th (Effector Th-Like). (d), Dot plot representations of transcriptomic and cytokine related gene modules for clusters in c.
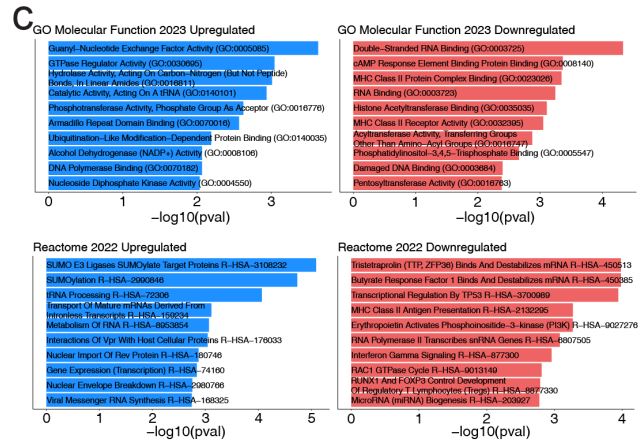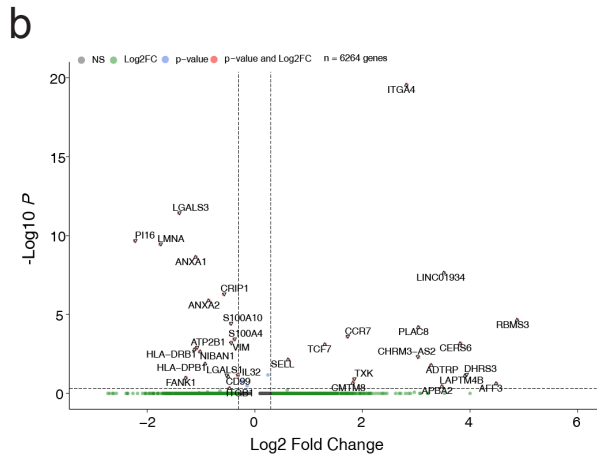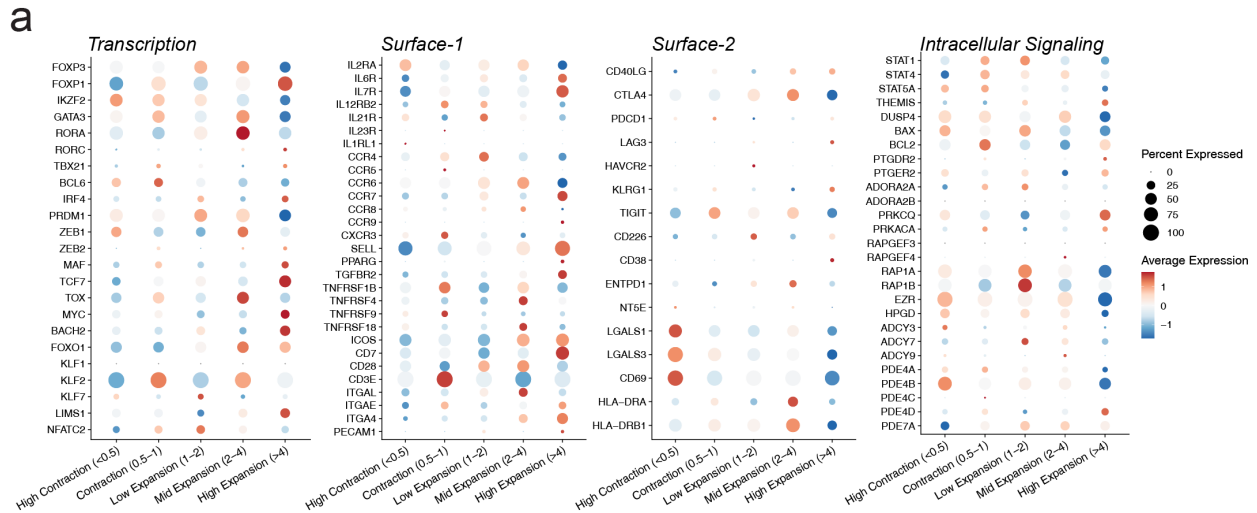
Supplemental Figure S4.8. Tracing Dynabead-Expanded Tregs with scRNAseq and scTCRseq.

(Figure caption continued on the next page.)

(Figure caption continued from the previous page.)

(a), Frequency distribution of TCR clones before (Pre, left) and after expansion with Dynabead (Dyna, right), plotted against log2 fold enrichment ratio (TCR clone frequency Dyna versus Pre). Markers represent unique clonal groups identified by paired α-and-β VJ segments, with top 25 most frequent pre-expansion clones highlighted. Dotted line at x=-3.5 indicates clones absent in Dyna TCR pool; dashed line at x=1 marks the two-fold expansion threshold. (b), Count distribution of all TCR clones identified in a, linear scale values: mean = 8.652 (Log2=3.113) and s.d. = 5.559 (Log2 = 2.475). (c), Violin distributions of Dyna/Pre enrichment ratios grouped by Treg identity clusters. Each marker represents an individual cell; cell markers at x=0 (y-axis) represents cells that were not found in the Dyna TCR pool. Dashed lines at x=0.5, 1, 2, and 4 mark expansion category thresholds. (d), Enrichment of Treg identity clusters within Dyna/Pre TCR enrichment expansion categories shown in c. (e), Frequency of unique clones that spread between one or multiple UMAP clusters from **Fig 4.3a** where *n* indicates the total number of cells. (f), Percentage of all TCRs within each Treg identity found within at least one other cluster. Data derives from the list of all TCRs that are shared between 2 or more clusters from e, where *n* indicates the total number of cells. The total *n* across all of f surpasses the count of unique TCRs listed in e (for cells found within 2-7 clusters) due to significant TCR overlap. Alternatively, the summation of [*n**(number of clusters)] across each column in e equals the total *n* in f. (g), Frequency of expansion labels across all cells corresponding to CD28-SA (SA, Left) or Dynabead (Dyna, Right) TCRs, with bars showing the percentage and n-number of total cells. "Undetected" corresponds to cells with TCRs found in the Pre pool but not within the expanded TCR pool. "NA" corresponds to cells that are found within the expanded TCR pool but have no match within the Pre TCR pool.

Supplemental Figure S4.9. Transcriptomic analysis of scTCRseq-traced, Dynabead-expanded Tregs.

(a), Dot plot representations of phenotypic modules used investigate Dynabead expansion categories. (b), Volcano plots showing differentially expressed genes between Dyna-expanded cells whose TCRs enriched >4 fold and contracted to <1 fold. Log2 fold change in gene expression (vertical dashed line) threshold set to ±0.3 and adjusted *P* value cutoff of 0.05 (-Log10 = 1.3, horizontal dashed line). (c), Pathway analysis of differentially expressed genes in b using the Go Molecular Function 2023 (Top) and Reactome 2022 (Bottom), comparing pathways upregulated in expanders (>2 fold, left) versus pathways upregulated in contractors (<1 fold, right).

G. TABLES

Table S4.1. T cell donor characteristics and documented use

Donor	Code*	Age	Sex	BMI	Smoking Status	Figure	Enrichment Method**	Subset %***		
								CD45RA+ HLA-DR-	CD45RA- HLA-DR-	CD45RA- HLA-DR+
A	40003	33	M	40.4	No	4.1e-g S4.2b-c	CD4 Neg	----	----	----
B	40819	37	M	25.9	No	4.1e-g S4.2b-c	CD4 Neg	----	----	----
C	40654	37	M	43.3	No	4.1e-i S4.2b-d	CD4 Neg	----	----	----
D	9509	24	M	20.4	No	4.1j-k 4.3,4.4, S4.2e-h, S4.6, S4.7, S4.8, S4.9	CD4 Neg	----	----	----
E	9827	27	M	24.4	Yes	4.1j-k S4.2e-h	CD4 Neg	----	----	----
F	9811	25	F	21.8	No	4.2, S4.3, S4.4, S4.5	CD4 Neg, CD25 Pos	39.7	22.6	34.9
G	7035	24	F	25.2	No	4.2, S4.3, S4.5	CD4 Neg, CD25 Pos	43.5	25.2	30.7
H	0124	32	F	26.1	No	4.2, S4.3, S4.5	CD4 Neg, CD25 Pos	54.6	18.4	24.9
I	8024	45	F	38.9	No	S4.1	CD4 Neg	----	----	----

*Internal reference code used for donor tracking

**Neg=negative selection, Pos=Positive selection

***Data not collected pre-activation for Donors A-E

Table S4.2. Antibody list used for FACs and flow cytometry phenotyping

Target	Fluorophore	Clone	Suppler	Catalog Number	Dilution
Sorting Panel 1 (**Fig S4.1**)					
CD4	FITC	SK3	Biolegend	344604	1:200
CD25	APC	2A3	BD	340939	1:100
CD127	PE	M21	BD	557938	1:100
Sorting Panel 2 (**Fig 4.2a**)					
CD4	BUV395	SK3	Biolegend	563550	1:200
CD25	APC	2A3	BD	340939	1:100
CD127	PE	M21	BD	557938	1:100
HLA-DR	BV711	G46-6	BD	563696	1:100
CD45-RA	FITC	HI100	Biolegend	983002	1:100
CCR7	PE-Cy7	G04H7	Biolegend	353226	1:100
CD62L	BV421	DREG-56	Biolegend	304828	1:200
Phenotyping Panel 1 – Traditional (**Fig 4.1, Fig S4.2**)					
Foxp3	AlexaFluor647	206D	Biolegend	320114	1:100
Helios	FITC	22F6	Biolegend	137214	1:100
CD4	BUV395	SK3	BD	563550	1:200
CD8a	BUV496	RPA-T8	BD	612942	1:100
CD25	AlexaFluor700	BC96	Biolegend	302622	1:100
CTLA-4	PercP-Cy5.5	BNI3	Biolegend	369608	1:100
ICOS	BV711	DX29	BD	563833	1:100
Live-Dead	APC-eFluor780	----	ThermoFisher	65-0865-18	1:2000
HLA-DR	PE	G46-6	BD	555812	1:100
CCR7	PE-Cy7	G043H7	Biolegend	353226	1:100
CD45RO	BV421	UCHL1	BD	562641	1:100
Phenotyping Panel 2 – Spectral (**Fig 4.2, Fig S4.3-S4.5**)					
CD4	BUV395	SK3	BD	563550	1:200
CD8	BUV496	RPA-T8	BD	612942	1:200
Foxp3	AlexaFluor647	206D	Biolegend	320114	1:50
Helios	PE	22F6	Invitrogen	12-9883-42	1:100
CD45RA	BV650	HI100	BD	563963	1:200
CD45RO	BUV661	UCHL1	BD	749887	1:200
CD226 (DNAM)	BV785	11A8	Biolegend	338322	1:100
TIGIT	BV605	A15153G	BIolegend	372712	1:100
ICOS	BV750	DX29	BD	746858	1:100
CD38	Superbright 436	HIT2	ThermoFisher	62-0389-42	1:100
CD39	PerCP-eFluor710	eBioA1(A1)	ThermoFisher	46-0399-42	1:100
HLA-DR	BV480	G46-6	BD	566113	1:100
TCF1	AlexaFluor488	C63D9	CellSignaling	6444S	1:100
CTLA-4	APC-eFluor780	14D3	ThermoFisher	47-1529-42	1:100
CD25	BV711	2A3	BD	563159	1:200
CCR7	PE-Cy7	G043H7	Biolegend	353226	1:200
Live-Dead	Zombie UV	----	Biolegend	423107	1:2000

H. REFERENCES

1. Balcerek, J. *et al.* Polyclonal Regulatory T Cell Manufacturing Under cGMP: A Decade of Experience. *Frontiers in Immunology* **12**, (2021).

2. Dong, S. *et al.* The effect of low-dose IL-2 and Treg adoptive cell therapy in patients with type 1 diabetes. *JCI Insight* **6**, e147474 (2021).

3. Tang, Q. *et al.* Selective decrease of donor-reactive T $_{regs}$ after liver transplantation limits T $_{reg}$ therapy for promoting allograft tolerance in humans. *Sci. Transl. Med.* **14**, eabo2628 (2022).

4. Bluestone, J. A. *et al.* Type 1 diabetes immunotherapy using polyclonal regulatory T cells. *Science Translational Medicine* **7**, 315ra189-315ra189 (2015).

5. Ferreira, L. M. R., Muller, Y. D., Bluestone, J. A. & Tang, Q. Next-generation regulatory T cell therapy. *Nat Rev Drug Discov* **18**, 749–769 (2019).

6. Amini, L. *et al.* Super-Treg: Toward a New Era of Adoptive Treg Therapy Enabled by Genetic Modifications. *Frontiers in Immunology* **11**, (2021).

7. MacDonald, K. N., Salim, K. & Levings, M. K. Manufacturing next-generation regulatory T-cell therapies. *Current Opinion in Biotechnology* **78**, 102822 (2022).

8. Duhen, T., Duhen, R., Lanzavecchia, A., Sallusto, F. & Campbell, D. J. Functionally distinct subsets of human FOXP3+ Treg cells that phenotypically mirror effector Th cells. *Blood* **119**, 4430–4440 (2012).

9. Shevyrev, D. & Tereshchenko, V. Treg Heterogeneity, Function, and Homeostasis. *Frontiers in Immunology* **10**, 3100 (2020).

10. Ermann, J. *et al.* Only the CD62L+ subpopulation of CD4+CD25+ regulatory T cells protects from lethal acute GVHD. *Blood* **105**, 2220–2226 (2005).

11. Opstelten, R. & Amsen, D. Separating the wheat from the chaff: Making sense of Treg heterogeneity for better adoptive cellular therapy. *Immunology Letters* **239**, 96–112 (2021).

12. Escobar, G., Mangani, D. & Anderson, A. C. T cell factor 1 (Tcf1): a master regulator of the T cell response in disease. *Sci Immunol* **5**, eabb9726 (2020).

13. Luo, Y. *et al.* Single-cell transcriptomic analysis reveals disparate effector differentiation pathways in human Treg compartment. *Nat Commun* **12**, 3913 (2021).

14. Mijnheer, G. *et al.* Conserved human effector Treg cell transcriptomic and epigenetic signature in arthritic joint inflammation. *Nat Commun* **12**, 2710 (2021).

15. Hoffmann, P. *et al.* Only the CD45RA+ subpopulation of CD4+CD25high T cells gives rise to homogeneous regulatory T-cell lines upon in vitro expansion. *Blood* **108**, 4260–4267 (2006).

16. Putnam, A. L. *et al.* Expansion of Human Regulatory T-Cells From Patients With Type 1 Diabetes. *Diabetes* **58**, 652–662 (2009).

17. Jarvis, L. B. *et al.* Therapeutically expanded human regulatory T-cells are super-suppressive due to HIF1A induced expression of CD73. *Commun Biol* **4**, 1–14 (2021).

18. Donnelly, C. *et al.* Optimizing human Treg immunotherapy by Treg subset selection and E-selectin ligand expression. *Sci Rep* **8**, 420 (2018).

19. Glinos, D. A. *et al.* Genomic profiling of T-cell activation suggests increased sensitivity of memory T cells to CD28 costimulation. *Genes Immun* **21**, 390–408 (2020).

20. Golovina, T. N. *et al.* CD28 Costimulation is Essential for Human T Regulatory Expansion and Function. *J Immunol* **181**, 2855–2868 (2008).

21. Hombach, A. A., Kofler, D., Hombach, A., Rappl, G. & Abken, H. Effective Proliferation of Human Regulatory T Cells Requires a Strong Costimulatory CD28 Signal That Cannot Be Substituted by IL-2. *J Immunol* **179**, 7924–7931 (2007).

22. Li, S. *et al.* Biomimetic immunomodulation by crosstalk with nanoparticulate regulatory T cells. *Matter* **4**, 3621–3645 (2021).

23. Zhang, D. K. Y., Cheung, A. S. & Mooney, D. J. Activation and expansion of human T cells using artificial antigen-presenting cell scaffolds. *Nat Protoc* **15**, 773–798 (2020).

24. Wauters, A. C. *et al.* Artificial Antigen-Presenting Cell Topology Dictates T Cell Activation. *ACS Nano* **16**, 15072–15085 (2022).

25. Trickett, A. & Kwan, Y. L. T cell stimulation and expansion using anti-CD3/CD28 beads. *Journal of Immunological Methods* **275**, 251–255 (2003).

26. Huang, X. *et al.* DNA scaffolds enable efficient and tunable functionalization of biomaterials for immune cell modulation. *Nat. Nanotechnol.* **16**, 214–223 (2021).

27. Delcassian, D., Sattler, S. & Dunlop, I. E. T cell immunoengineering with advanced biomaterials. *Integrative Biology* **9**, 211–222 (2017).

28. Hadley, P. *et al.* Precise surface functionalization of PLGA particles for human T cell modulation. *Nat Protoc* **18**, 3289–3321 (2023).

29. Hao, Y. *et al.* Dictionary learning for integrative, multimodal and scalable single-cell analysis. *Nat Biotechnol* **42**, 293–304 (2024).

30. McGinnis, C. S., Murrow, L. M. & Gartner, Z. J. DoubletFinder: Doublet Detection in Single-Cell RNA Sequencing Data Using Artificial Nearest Neighbors. *Cell Syst* **8**, 329-337.e4 (2019).

31. Subramanian, A., Alperovich, M., Yang, Y. & Li, B. Biology-inspired data-driven quality control for scientific discovery in single-cell transcriptomics. *Genome Biology* **23**, 267 (2022).

32. Borcherding, N., Bormann, N. L. & Kraus, G. scRepertoire: An R-based toolkit for single-cell immune receptor analysis. *F1000Res* **9**, 47 (2020).

33. Heumos, L. *et al.* Best practices for single-cell analysis across modalities. *Nat Rev Genet* **24**, 550–572 (2023).

34. Chen, E. Y. *et al.* Enrichr: interactive and collaborative HTML5 gene list enrichment analysis tool. *BMC Bioinformatics* **14**, 128 (2013).

35. Yu, G., Wang, L.-G., Han, Y. & He, Q.-Y. clusterProfiler: an R Package for Comparing Biological Themes Among Gene Clusters. *OMICS* **16**, 284–287 (2012).

36. Gene Ontology Consortium *et al.* The Gene Ontology knowledgebase in 2023. *Genetics* **224**, iyad031 (2023).

37. Milacic, M. *et al.* The Reactome Pathway Knowledgebase 2024. *Nucleic Acids Research* **52**, D672–D678 (2024).

38. Khantakova, J. N., Bulygin, A. S. & Sennikov, S. V. The Regulatory-T-Cell Memory Phenotype: What We Know. *Cells* **11**, (2022).

39. Dong, S. *et al.* Multiparameter single-cell profiling of human CD4+FOXP3+ regulatory T-cell populations in homeostatic conditions and during graft-versus-host disease. *Blood* **122**, (2013).

40. Kaech, S. M., Wherry, E. J. & Ahmed, R. Effector and memory T-cell differentiation: implications for vaccine development. *Nat Rev Immunol* **2**, 251–262 (2002).

41. Jameson, S. C. & Masopust, D. Understanding Subset Diversity in T Cell Memory. *Immunity* **48**, 214–226 (2018).

42. Rosenblum, M. D., Way, S. S. & Abbas, A. K. Regulatory T cell memory. *Nat Rev Immunol* **16**, 90–101 (2016).

43. Dias, S. *et al.* Effector Regulatory T Cell Differentiation and Immune Homeostasis Depend on the Transcription Factor Myb. *Immunity* **46**, 78–91 (2017).

44. Miragaia, R. J. *et al.* Single-Cell Transcriptomics of Regulatory T Cells Reveals Trajectories of Tissue Adaptation. *Immunity* **50**, 493-504.e7 (2019).

45. Gasper, D. J., Tejera, M. M. & Suresh, M. CD4 T-Cell Memory Generation and Maintenance. *Crit Rev Immunol* **34**, 121–146 (2014).

46. Rissiek, A. *et al.* The expression of CD39 on regulatory T cells is genetically driven and further upregulated at sites of inflammation. *Journal of Autoimmunity* **58**, 12–20 (2015).

47. Dees, S., Ganesan, R., Singh, S. & Grewal, I. S. Regulatory T cell targeting in cancer: Emerging strategies in immunotherapy. *European Journal of Immunology* **51**, 280–291 (2021).

48. Menning, A. *et al.* Distinctive role of CCR7 in migration and functional activity of naive- and effector/memory-like Treg subsets. *Eur J Immunol* **37**, 1575–1583 (2007).

49. Pfoertner, S. *et al.* Signatures of human regulatory T cells: an encounter with old friends and new players. *Genome Biology* **7**, R54 (2006).

50. Xydia, M. *et al.* Common clonal origin of conventional T cells and induced regulatory T cells in breast cancer patients. *Nat Commun* **12**, 1119 (2021).

51. Baecher-Allan, C., Wolf, E. & Hafler, D. A. MHC class II expression identifies functionally distinct human regulatory T cells. *J Immunol* **176**, 4622–4631 (2006).

52. Han, L. *et al.* Interleukin 32 Promotes Foxp3+ Treg Cell Development and CD8+ T Cell Function in Human Esophageal Squamous Cell Carcinoma Microenvironment. *Front Cell Dev Biol* **9**, 704853 (2021).

53. Hsiao, W.-Y., Lin, Y.-C., Liao, F.-H., Chan, Y.-C. & Huang, C.-Y. Dual-Specificity Phosphatase 4 Regulates STAT5 Protein Stability and Helper T Cell Polarization*. *PLOS ONE* **10**, e0145880 (2015).

54. Fuhrman, C. A. *et al.* Divergent Phenotypes of Human Regulatory T Cells Expressing the Receptors TIGIT and CD226. *The Journal of Immunology* **195**, 145–155 (2015).

55. Koizumi, S. & Ishikawa, H. Transcriptional Regulation of Differentiation and Functions of Effector T Regulatory Cells. *Cells* **8**, 939 (2019).

56. Cibrián, D. & Sánchez-Madrid, F. CD69: from activation marker to metabolic gatekeeper. *Eur J Immunol* **47**, 946–953 (2017).

57. Ronchetti, S. *et al.* Glucocorticoid-Induced Tumour Necrosis Factor Receptor-Related Protein: A Key Marker of Functional Regulatory T Cells. *Journal of Immunology Research* **2015**, (2015).

58. Newman, D. K. *et al.* PECAM-1 (CD31) expression in naïve and memory, but not acutely activated, CD8+ T cells. *J Leukoc Biol* **104**, 883–893 (2018).

59. Carrington, E. M. *et al.* Anti-apoptotic proteins BCL-2, MCL-1 and A1 summate collectively to maintain survival of immune cell populations both in vitro and in vivo. *Cell Death Differ* **24**, 878–888 (2017).

60. Ito, T. *et al.* Two functional subsets of FOXP3+ regulatory T cells in human thymus and periphery. *Immunity* **28**, 870–880 (2008).

61. Nozais, M. *et al.* MYC deficiency impairs the development of effector/memory T lymphocytes. *iScience* **24**, 102761 (2021).

62. Simone, D. *et al.* Single cell analysis of spondyloarthritis regulatory T cells identifies distinct synovial gene expression patterns and clonal fates. *Commun Biol* **4**, 1395 (2021).

63. Tu, Z. *et al.* Pro-inflammatory cytokine IL-6 regulates LMO4 expression in psoriatic keratinocytes via AKT/STAT3 pathway. *Immun Inflamm Dis* **11**, e1104 (2023).

64. Bendfeldt, H. *et al.* Stable IL-2 decision making by endogenous c-Fos amounts in peripheral memory T-helper cells. *J Biol Chem* **287**, 18386–18397 (2012).

65. Schuster, M., Plaza-Sirvent, C., Visekruna, A., Huehn, J. & Schmitz, I. Generation of Foxp3+CD25− Regulatory T-Cell Precursors Requires c-Rel and IκBNS. *Frontiers in Immunology* **10**, (2019).

66. Horwitz, D. A. Identity of mysterious CD4+CD25-Foxp3+cells in systemic lupus erythematosus. *Arthritis Research & Therapy* **12**, 101 (2010).

67. Marchingo, J. M. & Cantrell, D. A. Protein synthesis, degradation, and energy metabolism in T cell immunity. *Cell Mol Immunol* **19**, 303–315 (2022).

68. Tsukumo, S. *et al.* AFF3, a susceptibility factor for autoimmune diseases, is a molecular facilitator of immunoglobulin class switch recombination. *Science Advances* **8**, eabq0008 (2022).

69. Zeng, Y., Zhang, X., Li, F., Wang, Y. & Wei, M. AFF3 is a novel prognostic biomarker and a potential target for immunotherapy in gastric cancer. *J Clin Lab Anal* **36**, e24437 (2022).

70. Huynh, A. *et al.* The phosphatase PTEN-mediated control of PI-3 kinase in Tregs cells maintains homeostasis and lineage stability. *Nat Immunol* **16**, 188–196 (2015).

71. Hawse, W. F. & Cattley, R. T. T cells transduce T-cell receptor signal strength by generating different phosphatidylinositols. *Journal of Biological Chemistry* **294**, 4793–4805 (2019).

72. Wehbi, V. L. & Taskén, K. Molecular Mechanisms for cAMP-Mediated Immunoregulation in T cells – Role of Anchored Protein Kinase A Signaling Units. *Frontiers in Immunology* **7**, (2016).

73. Wang, B., Maile, R., Greenwood, R., Collins, E. J. & Frelinger, J. A. Naive CD8+ T Cells Do Not Require Costimulation for Proliferation and Differentiation into Cytotoxic Effector Cells1. *The Journal of Immunology* **164**, 1216–1222 (2000).

74. Au-Yeung, B. B. *et al.* A sharp T-cell antigen receptor signaling threshold for T-cell proliferation. *Proceedings of the National Academy of Sciences* **111**, E3679–E3688 (2014).

75. Sakaguchi, S., Yamaguchi, T., Nomura, T. & Ono, M. Regulatory T Cells and Immune Tolerance. *Cell* **133**, 775–787 (2008).

76. Bhattacharyya, N. D. & Feng, C. G. Regulation of T Helper Cell Fate by TCR Signal Strength. *Frontiers in Immunology* **11**, 624 (2020).

77. Levine, A. G., Arvey, A., Jin, W. & Rudensky, A. Y. Continuous requirement for the TCR in regulatory T cell function. *Nat Immunol* **15**, 1070–1078 (2014).

78. Dustin, M. L. & Cooper, J. A. The immunological synapse and the actin cytoskeleton: molecular hardware for T cell signaling. *Nat Immunol* **1**, 23–29 (2000).

79. Dupré, L., Boztug, K. & Pfajfer, L. Actin Dynamics at the T Cell Synapse as Revealed by Immune-Related Actinopathies. *Frontiers in Cell and Developmental Biology* **9**, (2021).

80. Steenblock, E. R., Fadel, T., Labowsky, M., Pober, J. S. & Fahmy, T. M. An Artificial Antigen-presenting Cell with Paracrine Delivery of IL-2 Impacts the Magnitude and Direction of the T Cell Response*. *Journal of Biological Chemistry* **286**, 34883–34892 (2011).

81. Wakamatsu, E., Mathis, D. & Benoist, C. Convergent and divergent effects of costimulatory molecules in conventional and regulatory CD4+ T cells. *Proc Natl Acad Sci U S A* **110**, 1023–1028 (2013).

82. Kumar, P., Bhattacharya, P. & Prabhakar, B. S. A Comprehensive Review on the Role of Co-signaling Receptors and Treg Homeostasis in Autoimmunity and Tumor Immunity. *J Autoimmun* **95**, 77–99 (2018).

83. Majedi, F. S. *et al.* Augmentation of T-Cell Activation by Oscillatory Forces and Engineered Antigen-Presenting Cells. *Nano Lett.* **19**, 6945–6954 (2019).

84. Cheung, A. S., Zhang, D. K. Y., Koshy, S. T. & Mooney, D. J. Scaffolds that mimic antigen-presenting cells enable ex vivo expansion of primary T cells. *Nat Biotechnol* **36**, 160–169 (2018).

85. Rhodes, K. R. *et al.* Bioengineered particles expand myelin-specific regulatory T cells and reverse autoreactivity in a mouse model of multiple sclerosis. *Science Advances* **9**, eadd8693 (2023).

86. Fritsche, E., Volk, H.-D., Reinke, P. & Abou-El-Enein, M. Toward an Optimized Process for Clinical Manufacturing of CAR-Treg Cell Therapy. *Trends in Biotechnology* **38**, 1099–1112 (2020).

87. MacDonald, K. N., Piret, J. M. & Levings, M. K. Methods to manufacture regulatory T cells for cell therapy. *Clin Exp Immunol* **197**, 52–63 (2019).

88. MacDonald, K. G. *et al.* Alloantigen-specific regulatory T cells generated with a chimeric antigen receptor. *J Clin Invest* **126**, 1413–1424.

89. Fernández-García, J. *et al.* CD8+ T cell metabolic rewiring defined by scRNA-seq identifies a critical role of ASNS expression dynamics in T cell differentiation. *Cell Rep* **41**, 111639 (2022).

90. Ntranos, V., Yi, L., Melsted, P. & Pachter, L. A discriminative learning approach to differential expression analysis for single-cell RNA-seq. *Nat Methods* **16**, 163–166 (2019).

91. Leblay, N. *et al.* Cite-Seq Profiling of T Cells in Multiple Myeloma Patients Undergoing BCMA Targeting CAR-T or Bites Immunotherapy. *Blood* **136**, 11–12 (2020).

92. Munn, D. H., Sharma, M. D. & Johnson, T. S. Treg destabilization and reprogramming: implications for cancer immunotherapy. *Cancer Res* **78**, 5191–5199 (2018).

93. Bailey-Bucktrout, S. L. *et al.* Self-antigen driven activation induces instability of regulatory T cells during an inflammatory autoimmune response. *Immunity* **39**, 949–962 (2013).

94. Zhou, X., Bailey-Bucktrout, S., Jeker, L. T. & Bluestone, J. A. Plasticity of CD4+ FoxP3+ T cells. *Current Opinion in Immunology* **21**, 281–285 (2009).

95. Williams, J. A., Tai, X. & Hodes, R. J. CD28-CD80/86 and CD40-CD40L Interactions Promote Thymic Tolerance by Regulating Medullary Epithelial Cell and Thymocyte Development. *Crit Rev Immunol* **35**, 59–76 (2015).

96. Tietscher, S. *et al.* A comprehensive single-cell map of T cell exhaustion-associated immune environments in human breast cancer. *Nat Commun* **14**, 98 (2023).

97. Wherry, E. J. & Kurachi, M. Molecular and cellular insights into T cell exhaustion. *Nat Rev Immunol* **15**, 486–499 (2015).

98. Klein, M. & Bopp, T. Cyclic AMP Represents a Crucial Component of Treg Cell-Mediated Immune Regulation. *Front Immunol* **7**, 315 (2016).

99. Su, W. *et al.* The cAMP–Adenosine Feedback Loop Maintains the Suppressive Function of Regulatory T Cells. *The Journal of Immunology* **203**, 1436–1446 (2019).

100. Schmidleithner, L. *et al.* Enzymatic Activity of HPGD in Treg Cells Suppresses Tconv Cells to Maintain Adipose Tissue Homeostasis and Prevent Metabolic Dysfunction. *Immunity* **50**, 1232-1248.e14 (2019).

101. Klein, M. *et al.* Repression of Cyclic Adenosine Monophosphate Upregulation Disarms and Expands Human Regulatory T Cells. *The Journal of Immunology* **188**, 1091–1097 (2012).

102. Peter, D., Jin, S. L. C., Conti, M., Hatzelmann, A. & Zitt, C. Differential Expression and

    Function of Phosphodiesterase 4 (PDE4) Subtypes in Human Primary CD4+ T Cells:

    Predominant Role of PDE4D1. *The Journal of Immunology* **178**, 4820–4831 (2007).

Publishing Agreement

It is the policy of the University to encourage open access and broad distribution of all theses, dissertations, and manuscripts. The Graduate Division will facilitate the distribution of UCSF theses, dissertations, and manuscripts to the UCSF Library for open access and distribution. UCSF will make such theses, dissertations, and manuscripts accessible to the public and will take reasonable steps to preserve these works in perpetuity.

I hereby grant the non-exclusive, perpetual right to The Regents of the University of California to reproduce, publicly display, distribute, preserve, and publish copies of my thesis, dissertation, or manuscript in any form or media, now existing or later derived, including access online for teaching, research, and public service purposes.

DocuSigned by:

Pierce Hadley

—6EC15F683773489…   Author Signature

3/15/2024

Date